SUPPLEMENTARY INFORMATION

Functionalized Nitro-Piperonal Thiosemicarbazones based Ruthenium(II)-Arene Complexes for DNA Interaction, Anticancer and Flow Cytometry Studies

Vishnunarayanan Namboothiri Vadakkedathu Palakkeezhillam[a], Jebiti Haribabu[b], Karthik KS[a], Vaishnu Suresh Kumar[a,d], Vipin Manakkadan[a], Puthiyavalappil Rasin[c], Mohith Garg[d], Arunachalam Arulraj[e], Daniel Moraga[f], Anandaram Sreekanth[a*]

[a]*Department of Chemistry, National Institute of Technology, Tiruchirappalli, Tamil Nadu, India-620015*

[b]*Facultad de Medicina, Universidad de Atacama, Los Carreras 1579, Copiapo 1532502, Chile*

[c]*Centre for nonlinear systems, Chennai Institute of Technology (CIT), Chennai 600069, India.*

[d]*Department of Chemical Engineering, Birla Institute of Technology & Science, Pilani-333031, Rajasthan. India*

[e]*Departamento de Electricidad, Facultad de Ingeniería, Universidad Tecnológica Metropolitana (UTEM), Av. José Pedro Alessandri 1242, Ñuñoa 7800002, Santiago, Chile*

[f]*Laboratorio de Fisiología, Departamento de Ciencias Biomédicas, Facultad de Medicina, Universidad de Tarapacá, Arica 1000000, Chile*

*Corresponding Author: E-mail: sreekanth@nitt.edu

TABLE OF CONTENTS

List of Tables		**Page No.**

S1. Materials and methods

All chemicals utilized in this study were procured from reputable suppliers, including Sigma Aldrich, Merck, and Alfa Aesar. These chemicals were of the highest purity grade, eliminating the need for additional purification. Melting points were determined using a Lab India instrument without any modifications. For IR spectra, a Perkin Elmer Frontier FT-IR spectrophotometer was utilized. Elemental analyses were performed using a CHNS analyzer 2400 series II. High-resolution mass spectrometry (HRMS) data were obtained using an Agilent 6546 LC-Q/TOF instrument. Electronic transitions of the synthesized compounds were observed with a Specord S 600 Analytik Jena UV-Visible spectrometer. Fluorescence spectroscopy, investigating DNA/BSA binding of the compounds, was conducted on a Jasco V-630 spectrophotometer. NMR spectra were recorded on a Bruker 500 MHz spectrometer, using TMS as the internal standard and DMSO-d_6/CDCl3 as the solvent. Additionally, the single crystal structures of complexes (**6NPT, RuPNMT,** and **RuBNCT**) were elucidated through an XRD study performed on a three-circle Bruker APEX II X-ray CCD diffractometer.

S2. Synthesis

S2.1. 6-Nitropiperonal pyrrolidine TSC (6NPT)

Yield 88%. Yellow-solid. M.p.:165 °C. Anal. Cald. for $C_{13}H_{14}N_4O_4S$: C, 48.44; H, 4.38; N, 17.38; S, 9.95; Found: C, 48.47; H, 4.37; N, 17.34; S, 9.96. UV-Vis (DMSO): λ_{max}, nm 309

($\pi \rightarrow \pi^*$), 388($n \rightarrow \pi^*$). FT-IR (ATR): v, cm^{-1}, 3139 (N^2H) , 1509 (C=N), 1241 (C=S). ^{1}H NMR (500 MHz, DMSO) δ 11.26 (s, 1H, NH), 8.62 (s, 1H, HC=N), 7.63 (s, 1H, piperonal-H), 7.43 (s, 1H, piperonal-H), 6.27 (s, 2H, piperonal-H), 3.72 (t, J = 6.7 Hz, 4H, pyrrolidine-H), 1.90 (s, 4H, pyrrolidine-H).^{13}C NMR (126 MHz, DMSO) δ 176.8 (C=S), 152.2 (C=N), 148.9, 143.1, 138.9, 126.7, 105.4 (aromatic), 104.18 (OCO), 40-38 (pyrrolidine). HR-MS (m/z): Calculated 323.0814, Found 323.0809 $[M+H^+]^+$

S2.2. 6-Nitropiperonal morpholine TSC (6NMT)

Yield: 92%. Yellow-solid. M.p.:172 °C. Anal. Cald. for $C_{13}H_{14}N_4O_5S$: C, 46.15; H, 4.17; N, 16.56; S, 9.48; Found: C, 46.14; H, 4.18; N, 16.55; S, 9.47. UV-Vis (DMSO): λ^{max}, nm 310 ($\pi \rightarrow \pi^*$), 383 ($n \rightarrow \pi^*$). FT-IR (ATR): v, cm^{-1}, 3343 (N^2H), 1510 (C=N), 1210 (C=S). ^{1}H NMR (500 MHz, DMSO) δ 11.47 (s, 1H, NH), 8.60 (s, 1H, HC=N), 7.65 (s, 1H, piperonal-H), 7.41 (s, 1H, piperonal-H), 6.28 (s, 2H, piperonal-H), 3.94 – 3.90 (t, 4H, Morpholine-H), 3.69 – 3.65 (t, 4H, Morpholine-H). ^{13}C NMR (126 MHz, DMSO) δ 181.1 (C=S), 152.2 (C=N), 149.1, 143.2, 139.9, 126.4, 105.4 (aromatic), 104.24 (OCO), 66.4,50.72 (morpholine). HRMS (m/z): Calculated 339.0763, Found 339.075 $[M+H^+]^+$

S2.3. 6-Nitropiperonal-N-cyclohexyl TSC (6NCT)

Yield: 90 %. Yellow-solid. M.p.:167 °C. Anal. Cald. for $C_{15}H_{18}N_3O_4S$: C, 51.42; H, 5.18; N, 15.99; S, 9.15; Found: C, 51.45; H, 5.20; N, 15.95; S, 9.17. UV-Vis (DMSO): λ_{max}, nm 321 ($\pi \rightarrow \pi^*$), 390 ($n \rightarrow \pi^*$). FT-IR (ATR): v, 3344 (N^4H) cm^{-1}, 3152 (N^2H) , 1523 (C=N), 1253 (C=S). ^{1}H NMR (500 MHz, DMSO) δ , 11.62 (s, 1H, NH), 8.48 (s, 1H, NH), 7.97 (s, 1H, piperonal-H), 7.63 (s, 1H, piperonal-H), 6.28 (s, 2H, piperonal-H) , 4.26 – 4.17 (m, 1H, NH-cyclohexyl), 1.88 (dd, J = 12.2, 2.4 Hz, 2H, cyclohexyl-H), 1.75 (d, J = 13.2 Hz, 2H, cyclohexyl-H), 1.63 (d, J = 12.6 Hz, 1H, cyclohexyl-H), 1.59–1.42 (m, 2H, cyclohexyl-H), 1.42–1.27 (m, 2H, cyclohexyl-H), 1.28 – 1.04 (m, 2H, Cyclohexyl-H).^{13}C NMR (126 MHz, DMSO) δ 176.3 (C=S), 152.2 (C=N), 149.0 , 143.6, 137.9, 126.0, 106.58, 105.33(aromatic) , 104.13(OCO) , 53.47 , 32.16 , 25.55(cyclohexyl). HR-MS (m/z): Calculated 351.0178, Found 350.9877 $[M+H^+]^+$.

S2.4. 6-Nitropiperonal N-methyl TSC (6NMeT)

Yield: 88%. Yellow- White solid. M.p.:173 °C. Anal. Cald. for $C_{10}H_{10}N_4O_4S$: C, 42.55;

H, 3.57; N, 19.85; S, 11.36; Found: C, 42.58; H, 3.56; N, 19.84; S, 11.38. UV-Vis (DMSO): λ_{max}, nm 323 ($\pi \rightarrow \pi^*$), 386 ($n \rightarrow \pi^*$). FT-IR (ATR): ν, cm^{-1}, 3338 (N^2H), 3126 (N^4H), 1510 (C=N), 1228 (C=S). ^1H NMR (500 MHz, chloroform) δ 11.71(s, 1H, NH), 7.72 (s, 1H, HC=N), 7.61 (s, 1H, NH-methyl), 7.50 (s, 1H, piperonal-H), 6.78 (s, 1H, piperonal-H), 5.91 – 5.88 (s, 2H, piperonal-H), 2.93–2.92 (d , J=5.9Hz, 3H, methyl-H). HR-MS (m/z): Calculated 284.0579, Found 284.2021 $[M+2H^+]^+$,

S2.5. Ru(II)-(η^6-p-cymene) NPT (RuPNPT)

Yield: 81%. Orange-red solid. M.p.:198 °C. Anal. Cald. for $C_{23}H_{27}ClN_4O_4RuS$: C, 46.66; H, 4.60; N, 9.46; S, 5.42; Found: C, 46.69; H, 4.68; N, 9.45; S, 5.41. UV-Vis (DMSO): λ_{max}, nm 262 ($\pi \rightarrow \pi^*$), 327 ($n \rightarrow \pi^*$), 439 ($d^6 \rightarrow \pi^*$). FT-IR (ATR): ν, cm^{-1}, 1497 (C=N), 875 (C-S). ^1H NMR (500 MHz, $CDCl_3$) δ 9.11 (s, 1H, HC=N), 8.46 (s, 1H, piperonal-H), 7.76 (s, 1H, piperonal-H), 6.29 (s, 1H, piperonal-H), 6.23 (s, 1H, piperonal-H), 5.43 (d, J = 5.8 Hz, 1H, aromatic-H of p-cymene), 4.97 (d, J = 5.6 Hz, 1H, aromatic-H of p-cymene), 4.84 (d, J = 5.9 Hz, 1H, aromatic-H of p-cymene), 4.34 (d, J = 5.6 Hz, 1H, aromatic-H of p-cymene), 3.88 (s, 4H, pyrrolidine-H), 3.72 (t, J = 4.7 Hz, 4H, pyrrolidine-H), 2.07 (s, 3H, CH_3 of p-cymene), 1.14 (s, 3H, $(CH_3)_2$ of p-cymene), 1.04 (s, 3H, $(CH_3)_2$ of p-cymene). ^{13}C NMR (126 MHz, $CDCl_3$) δ 171.70 (C=S), 152.6(C=N), 149.9, 142.0, 127.1, 112.8, 106.4, 105.03 (aromatic), 104.17 (OCO), 96.1, 90.2, 87.6, 83.9, 81.0, 79.6 (p-cymene), 26.4, 24.9 (pyrrolidine), 30.6, 23.6, 20.7, 18.6 (p-cymene). HR-MS (m/z), Calculated 557.0796, Found 557.0807 $[M–Cl^–]^+$

S2.6. Ru(II)-(η^6-p-cymene) NMT (RuPNMT)

Yield: 85%. Red solid. M.p.:195 °C. Anal. Cald. for $C_{23}H_{27}ClN_4O_5RuS$: C, 45.43; H, 4.48; N, 9.21; S, 5.27; Found: C, 45.45; H, 4.51; N, 9.18; S, 5.26. UV-Vis (DMSO): λ_{max}, nm 265 ($\pi \rightarrow \pi^*$), 329 ($n \rightarrow \pi^*$), 438 ($d^6 \rightarrow \pi^*$). FT-IR (ATR): ν, cm^{-1}, 1485 (C=N), 881 (C-S). ^1H NMR (500 MHz, $CDCl_3$) δ 9.11 (s, 1H, HC=N), 8.46 (s, 1H, piperonal-H), 7.76 (s, 1H, piperonal-H), 6.29 (d, 1H, piperonal-H), 6.23 (d, 1H, piperonal-H), 5.43 (d, J = 5.8 Hz, 1H, aromatic-H of p-cymene), 4.97 (d, J = 5.6 Hz, 1H, aromatic-H of p-cymene), 4.84 (d, J = 5.9 Hz, 1H, aromatic-H of p-cymene), 4.34 (d, J = 5.6 Hz, 1H, aromatic-H of p-cymene), 3.88 (d, 3H, morpholine-H), 3.72 (d, J = 4.7 Hz, 4H, morpholine-H), 2.17 (m, J = 3.1 Hz, 1H, $(CH_3)_2CH$ of p-cymene), 2.07 (s, 3H, CH_3 of p-cymene), 1.14 (t, 3H, $CH_3)_2$ of p-cymene), 1.04 (t, 3H, $(CH_3)_2$ of p-cymene). ^{13}C NMR (126 MHz, $CDCl_3$) δ 176.9 (C=S), 176.9 (C=N), 152.2, 148.7, 142.2,

128.4, 113.8, 105.6 (aromatic), 104.7(OCO), 103.6, 96, 92, 87.9, 81.0, 79.3,(p-cymene), 66.7, 49.3 (morpholine), 30.3, 23.9, 20.5, 18.7(p-cymene). HR-MS (m/z), Calculated 573.0745 , Found 573.0752 $[M–Cl^–]^+$

S2.7. Ru(II)-(η^6-p-cymene) NCT (RuPNCT)

Yield: 83%. Brown solid. M.p.:195 °C. Anal. Cald. for $C_{25}H_{31}ClN_4O_4RuS$: C, 48.42; H, 5.04; N, 9.03; S, 5.17; Found: C, 48.42; H, 5.03; N, 9.07; S, 5.14. UV-Vis (DMSO): λ_{max}, nm 265 ($\pi\rightarrow\pi^*$), 329 ($n\rightarrow\pi^*$), 433 ($d^6\rightarrow\pi^*$). FT-IR (ATR): ν, cm^{-1}, 3136 (N^4H) 1478 (C=N), 875 (C-S). ^1H NMR (500 MHz, $CDCl_3$) δ 8.86 (s, 1H, HC=N), 8.20 (s, 1H, piperonal-H), 7.80 (s, 1H, piperonal-H), 6.34 (d, 1H, piperonal-H), 6.29 (d, 1H, piperonal-H), 5.46 (d, J = 6.0 Hz, 1H, aromatic-H of p-cymene), 5.05 (d, J = 5.4 Hz, 1H, aromatic-H of p-cymene), 4.92 (d, J = 6.0 Hz, 1H, aromatic-H of p-cymene), 4.41 (d, J = 5.4 Hz, 1H, aromatic-H of p-cymene), 3.92 (d, 1H, NH-cyclohexyl), 2.70 (m, J = 13.3, 6.7 Hz, 1H, $(CH_3)_2CH$ of p-cymene), 2.09 (s, 3H, CH_3 of p-cymene), 2.04 (dt, J = 12.2 Hz, 2H, cyclohexyl-H), 1.80 (dt, J = 13.8 Hz, 2H, cyclohexyl-H), 1.70 (tt, 2H, cyclohexyl-H), 1.60 (tt, *J* = 12.3 Hz, 1H, cyclohexyl-H), 1.45 (tt, 2H, cyclohexyl-H), 1.32 – 1.24 (tt, 2H, cyclohexyl-H), 1.18 (d, *J* = 7.0 Hz, 3H, $(CH_3)_2$ of p-cymene), 1.12 (d, *J* = 6.9 Hz, 3H, $(CH_3)_2$ of p-cymene).^{13}C NMR (126 MHz, $CDCl_3$) δ 175.4 (C=S), 156.6 (C=N), 152.7, 150.3, 142.3, 125.7, 113, 106.3(aromatic carbon), 105.3(OCO), 104.3, 103.6, 89.4, 87.2, 81.3, 79.8 (p-cymene), 55, 32.1, 24.4, 23.5 (cyclohexane), 30.8, 25.2, 20.8, 18.7 (p-cymene). HR-MS (m/z), Calculated 585.1109, Found 585.1117 $[M–Cl^–]^+$

S2.8. Ru(II)-(η^6-p-cymene) NMeT (RuPNMeT)

Yield: 82% Orange solid. M.p.:165 °C. Anal. Cald. for $C_{20}H_{23}ClN_4O_4RuS$: C, 43.52; H, 4.20; N, 10.15; S, 5.81; Found: C, 43.55; H, 4.23; N, 10.12; S, 5.80. UV-Vis (DMSO): λ_{max}, nm 269 ($\pi\rightarrow\pi^*$), 327 ($n\rightarrow\pi^*$), 424 ($d^6\rightarrow\pi^*$). FT-IR (ATR): *ν*, cm^{-1},3222 (N^4H), 1492 (C=N), 862 (C-S). ^1H NMR (500 MHz, $CDCl_3$) δ 8.86 (s, 1H, HC=N), 8.35 (d, 1H, piperonal-H), 8.26 (d, 1H, piperonal-H), 7.83 (d, 2H, piperonal-H), 5.47–5.43 (m, 1H, aromatic-H of p-cymene), 5.36–5.27 (m, 1H, aromatic-H of p-cymene), 5.07–5.00 (m, 1H, aromatic-H of p-cymene), 4.94 (m, 1H, $(CH_3)_2CH$ of p-cymene), 3.17 (d, 3H, $(CH_3)_2$ of p-cymene), 2.97–2.83 (s, 3H, $(CH_3)_2$ of p-cymene), 2.36 (m, 1H, NH-CH_3), 2.31 (d, 3H, CH_3), 2.13 (d, 3H, CH_3 of p-cymene). ^{13}C NMR (126 MHz, $CDCl_3$) δ 175.3 (C=S), 158.3 (C=N), 152.7, 151.0, 147.5, 127.8, 116.3, 113.5 (aromatic carbon) , 105.6 (OCO), 103.1, 102.8, 89.4, 87.5, 82.3, 80.1(p-cymene), 54.9 (CH_3),

30.7, 25.1, 21.2 (p-cymene). HR-MS (m/z) $[M–Cl^–]^+$, Calculated 517.0483, Found 517.0488

S2.9. Ru(II)-(η^6-benzene) NPT (RuBNPT)

Yield: 79%. Reddish brown solid. M.p.:165 °C. Anal. Cald. for $C_{19}H_{19}ClN_4O_4RuS$: C, 42.58; H, 3.57; N, 10.45; S, 5.98; Found: C, 42.60; H, 3.54; N, 10.47; S, 5.96. UV-Vis (DMSO): λ_{max}, nm 265 ($\pi\rightarrow\pi^*$), 331 ($n\rightarrow\pi^*$), 438 ($d^6\rightarrow\pi^*$). FT-IR (ATR): ν, cm^{-1}, 1471 (C=N), 849 (C-S). ^{1}H NMR (500 MHz, DMSO) δ 8.95 (s, Hz, 1H, HC=N), 8.35 (s, 1H, piperonal-H), 7.90 (s, 1H, piperonal-H), 7.71 (d, 1H, piperonal-H), 7.15 (d, 1H, piperonal-H), 5.41 (s, 6H, benzene-H), 3.54 (t, 4H, pyrrolidine-H), 1.91 (t, 4H, pyrrolidine-H). ^{13}C NMR (126 MHz, DMSO) δ 177.6 (C=S), 152.6 (C=N), 148.0, 142.2, 147.5, 129.0, 113.2, 107.2 (aromatic carbon) , 105.2(OCO), 103.2, 89.4 , 87.3, 83.8, 81.2, 79.6 (benzene), 30.6, 28.7, 23.5, 20.8 (pyrrolidine). HR-MS (m/z), Calculated 536.9937, Found 536.1674 $[M+H^+]^+$

S2.10. Ru(II)-(η^6-benzene) NMT (RuBNMT)

Yield: 82%. Reddish brown solid. M.p.:165 °C. Anal. Cald. for $C_{19}H_{19}ClN_4O_5RuS$: C, 41.34; H, 3.47; N, 10.15; S, 5.81; Found: C, 41.33; H, 3.48; N, 10.16; S, 5.82. UV-Vis (DMSO): λ_{max}, nm 267 ($\pi\rightarrow\pi^*$), 334 ($n\rightarrow\pi^*$), 436 ($d^6\rightarrow\pi^*$). FT-IR (ATR): ν, cm^{-1}, 1485 (C=N), 884 (C-S). ^{1}H NMR (500 MHz, DMSO) δ 9.02 (s, 1H, HC=N), 7.82 (s, 1H, piperonal-H), 7.58 (s, 1H, piperonal-H), 7.37 (s, 6H, benzene-H), 6.32 (s, 2H, piperonal-H), 3.79 (t,3H, morpholine-H), 3.66 (t, 4H, morpholine-H). ^{13}C NMR (126 MHz, DMSO) δ 175.3 (C=S), 158.3 (C=N), 152.7, 151.0, 147.5, 127.8, 116.3, 113.5 (aromatic carbon), 105.6(OCO), 103.1, 102.8, 89.4, 87.5, 82.3, 80.1(benzene), 65.4, 54.9 (morpholine). HR-MS (m/z) Calculated 517.0119, Found 517.0204 $[M–Cl^–]^+$,

S2.11. Ru(II)-(η^6-benzene) NCT (RuBNCT)

Yield: 88%. Brown-solid. M.p.:165 °C. Anal. Cald. for $C_{21}H_{23}ClN_4O_4RuS$: C, 44.72; H, 4.11; N, 9.93; S, 5.69; Found: C, 44.74; H, 4.13; N, 9.91; S, 5.67. UV-Vis (DMSO): λ_{max}, nm 266 ($\pi\rightarrow\pi^*$), 327 ($n\rightarrow\pi^*$), 428 ($d^6\rightarrow\pi^*$). FT-IR (ATR): ν, cm^{-1}, 3131(N^{4}H) ,1465 (C=N), 862 (C-S). ^{1}H NMR (500 MHz, DMSO) δ 8.81 (d, J = 9.1 Hz, 1H, HC=N), 8.17 (s, 1H, piperonal-H), 8.08 (s, 1H, piperonal-H), 8.06 (s, 1H, piperonal-H), 7.75 (s, 1H, piperonal-H), 7.67 (d, J = 27.7 Hz, 1H, NH-cyclohexyl), 6.33 (s, 6H, benzene-H), 1.77 (s, 2H, cyclohexyl-H), 1.70 (s, 1H, cyclohexyl-H), 1.43 (d, J = 5.6 Hz, 1H, cyclohexyl-H), 1.30 (s, 2H, cyclohexyl-H), 1.24

(s, 2H, cyclohexyl-H), 1.11 (m, 2H, cyclohexyl-H). ^{13}C NMR (126 MHz, DMSO) δ 175.3 (C=S), 158.3 (C=N), 151.8, 147.5, 127.8, 116.3, 113.5, 112.6 (aromatic carbon), 105.8 (OCO), 103.1, 102.8, 89.4 , 87.5, 82.3, 80.1(benzene), 54.3, 30.7, 25.1, 24.4, 21.2, 18.1 (cyclohexyl). HR-MS (m/z): Calculated 529.0483, Found 529.0502 $[M–Cl^–]^+$,

S2.12. Ru(II)-(η^6-benzene) NMeT (RuBNMeT)

Yield: 88%. Brown-solid. M.p.:165 °C. Anal. Cald. for $C_{16}H_{15}ClN_4O_4RuS$: C, 38.75; H, 3.05; N, 11.30; S, 6.47; Found: C, 38.79; H, 3.03; N, 11.29; S, 6.44. UV-Vis (DMSO): λ_{max}, nm 262 ($\pi\rightarrow\pi^*$), 330 ($n\rightarrow\pi^*$), 420 ($d^6\rightarrow\pi^*$). FT-IR (ATR): v, cm^{-1}, 3152(N^{4}H), 1496 (C=N), 875 (C-S). ^{1}H NMR (500 MHz, DMSO) δ 11.74 (s, 1H, HC=N), 8.74 (m, 1H, NH-CH_3), 8.48 (s, 1H, piperonal-H), 8.03 (s, 1H, piperonal-H), 7.63 (s, 1H, piperonal-H), 7.37 (s, 2H, piperonal-H), 5.98 (s, 6H, benzene-H), 3.02 (s, 3H, CH_3), 2.77 (s, 1H). ^{13}C NMR (126 MHz, DMSO) δ 182.9 (C=S), 156.7 (C=N), 152.5, 150.1, 148.1, 142.2, 137.8, 129.0, 113.2 (aromatic carbon), 104.2(OCO), 103.2, 89.4, 87.3, 83.8, 79.6, 78.8 (benzene), 42.1 (CH_3). HR-MS (m/z): Calculated 475.3482, Found 475.3265 $[M–Cl^–]^+$,

S3. Single crystal XRD technique

X-ray diffraction data for the **6NPT** and **RuPNMT** were acquired utilizing a Bruker Quest X-ray diffractometer in fixed-Chi geometry. The X-ray radiation was produced by a Mo-Iμs X-ray tube with a wavelength (Kα) of 0.71073Å. The goniometer was controlled, and integrated intensity information for each reflection was gathered using APEX3 software.[1] To account for absorption effects, the acquired data underwent analysis with the absorption correction program SADABS.[2] The absence of any additional symmetry was confirmed using the PLATON program (ADDSYM).[3] Following this, the structures were plotted, and final data refinement was carried out using the Olex2 software.[4]

S4. Stability studies

To assess the stability of the complexes, we diluted them in phosphate buffer solution (PBS) with a pH of 7.4 at both low (4 mM NaCl) and high (110 mM NaCl) concentrations. We monitored the bands continuously for an hour and obtained UV-Visible spectra at regular intervals to evaluate their stability under the specified conditions. The primary aim of this stability study was to understand how the complexes responded to different ionic environments

and whether they maintained stability over time. The insights gained from this study are valuable for considering the potential applications and reactivity of these complexes.

S5. Molecular Docking Study

In this study, we utilized molecular docking techniques to investigate the interactions between our synthesized complexes and the EGFR protein (PDB ID: 7KNW). Docking simulations were performed using AutoDock4 with the MGL Tools 1.5.7 interface, employing a Lamarckian genetic algorithm search and stochastic scoring function to predict favorable binding configurations.[5] Prior to docking, we utilized the PRankWeb web server, incorporating the p2rank machine learning package, to identify active binding sites on the EGFR protein.[6] This crucial step enabled us to pinpoint specific regions where ligands are likely to bind and interact effectively. By conducting docking experiments between the compounds and EGFR, we gained valuable structural insights into the potential inhibition mechanisms of the synthesized complexes. These simulations generated multiple structural hypotheses regarding the interactions between the complexes and EGFR, elucidating potential inhibition mechanisms. Furthermore, we calculated the free binding energies throughout the docking process to identify the optimal binding site for each compound within the protein. This analysis revealed the binding site with the lowest binding free energy, indicating the most promising location for ligand binding. To further elucidate the interactions between the compounds and EGFR, we utilized Chimera to visualize and assess the docking results.[7] Our research provided a comprehensive understanding of the binding modes and key interactions between the synthesized complexes and EGFR. In summary, the molecular docking experiments yielded valuable insights into the potential interactions between the synthesized complexes and EGFR, laying a foundation for future research and the rational design of novel compounds aimed at enhancing binding affinities and improving inhibitory effects on the target protein.

S6. DNA Binding Study

In order to thoroughly assess the bioactivity of the developed compounds in a laboratory setting, we utilized calf-thymus DNA (CT-DNA) and bovine serum albumin (BSA).[8] The CT-DNA was dissolved in a Tris HCl/NaCl buffer with a pH of 7.2 for the binding assays. A buffer solution was prepared by modifying the pH of a solution containing 5 mM tris(hydroxymethyl)aminomethane and 50 mM NaCl. The optical density ratio at 260/280 nm was used to verify that the CT-DNA did not contain any protein contamination. In order to investigate the binding of CT-DNA, the synthesized compounds were dissolved in a solution

containing 5% DMSO, Tris HCl, and NaCl. This resulted in solutions with a concentration of 25 M. Modifications in the UV-Visible spectra were detected when the concentration of CT-DNA increased in the chemical solution contained in a cuvette, ranging from 0 to 50 µM.

The Wolfe-Shimmer equation (**Equation S1**) was employed to assess the binding capacity of the complexes. The equation is presented as follows:

$$\mathbf{[DNA]/(\varepsilon_a-\varepsilon_f) = [DNA]/(\varepsilon_b-\varepsilon_f) + 1/K_b\,(\varepsilon_b-\varepsilon_f)} \quad (\textbf{Equation S1})$$

In this equation:

[DNA] denotes the concentration of DNA.

ε_a represents the apparent extinction coefficient, calculated as A(observed)/[complex].

ε_f is the extinction coefficient for the free complex.

ε_b stands for the extinction coefficient for the complex in its fully bound form.

The intrinsic binding constant (K_b) values were established by plotting the ratio of [DNA] to ($\varepsilon a-\varepsilon f$) against [DNA]. By examining the ratio of the slope to the y-intercept in this plot, we were able to determine the K_b values, which indicate the degree of binding between the complexes and DNA. This research provides vital insights into the nature of the interaction and emphasizes the potential of the complexes as DNA intercalators.

The synthesized compounds were tested for their intercalating capacities by recording the fluorescence spectra of CT-DNA/EB (at pH 7.2) to learn more about how they displaced ethidium bromide (EB). As the concentration of the compounds grew, the fluorescence intensity of CT-DNA/EB at 596 nm (with excitation at 510 nm) decreased because EB was displaced from its binding sites as a result of competitive binding to CT-DNA. These findings suggest that synthetic compounds have the ability to interact with CT-DNA, which could make them effective DNA intercalators.

The compounds' ability to displace ethidium bromide (EB) relative to their binding affinity to DNA can be correlated using the Stern-Volmer/quenching constant, as determined by the following equation:

$$\mathbf{F^0/F = 1 + K_q[Q]} \quad (\textbf{Equation S2})$$

In this equation:

F^0 represents the intensity of the ligand when it is switched off.

F denotes the intensity of the ligand when it is switched on.

[Q] stands for the concentration of the compound (complex).

K_q represents the Stern-Volmer constant.

Through the application of the Stern-Volmer/quenching constant, we can acquire valuable insights into the interaction dynamics between the synthesized compounds and DNA. This parameter serves as a tool for comprehending the fluorescence quenching phenomenon, enabling the assessment of the strength of the compounds' binding to DNA. This information is crucial for understanding the DNA intercalation capabilities of the compounds.

Additionally, the cyclic voltametric technique stands as an effective approach for exploring the interaction between the metal complexes and DNA. This method offers a significant complement to the spectral experiments previously employed, contributing additional valuable insights into the nature of their interaction.

Viscosity experiments were carried out using a semi-micro viscometer maintained at 27 C in a thermostatic water bath. DNA samples (0.5 µM) were prepared by sonication in order to minimize the complexities arising from the DNA flexibility. The flow time was measured three times for each sample and an average flow time was then calculated. The values of relative specific viscosity (η/η_0), where g is the relative viscosity of DNA in the presence of the complex and η_0 is the relative viscosity of DNA alone, were plotted against 1/R, (1/R = [compound]/[DNA]). Relative viscosity (η_0) values were calculated from the observed flow time of the DNA solution (t) corrected for the flow time of the buffer alone (t_0), using the expression $\eta_0 =(t-t_0)/t_0$.

S7. BSA Binding Study

In this study, Bovine Serum Albumin (BSA) served as a representative protein model to assess the interaction of the Ru(II) complexes.[9] Due to its constituent amino acids, notably tryptophan, tyrosine, and phenylalanine, BSA exhibits intrinsic fluorescence characteristics. A fixed concentration of BSA (1 µM) was prepared in a PBS buffer with a pH of 7.2 to investigate its binding behavior. The fluorescence intensities were subsequently observed as incremental amounts of the Ru(II) complexes (ranging from 0 to 30 µM) were added to the BSA solution. Fluorescence quenching spectra of BSA were recorded at 346 nm (λex = 280 nm) at room temperature, and synchronous fluorescence quenching spectra were obtained at two distinct

offsets (Δλ= 60 and 15 nm). The quenching constants (K_q) were calculated from the slopes of the resulting straight lines using the Stern-Volmer equation (**Equation S2**).

$$\mathbf{F^0/F = 1 + K_q[Q]} \text{ (Equation S2)}$$

In this equation, F^0 denotes the emission intensity in the absence of quenchers, while F denotes the emission intensity in the presence of Ru(II) complexes. The Scatchard equation (**Equation S3**) was used to further investigate the binding strength of the complexes with BSA.

$$\mathbf{\log [(F^0\text{-}F)/F] = \log K_b + n \log [Q]} \text{ (Equation S3)}$$

In this equation, K_b signifies the equilibrium binding constant, and n is the number of binding sites. K_b was derived from the antilogarithm of the intercept, and n was calculated from the slope of the plot log [(F^0-F)/F] against log [Q]. These investigations provide critical insights into the interaction of the Ru(II) complexes with BSA, assisting in the effective elucidation of their protein binding capacities. Inorder to find out the quenching mechanism, we carried out the absorption spectra for BSA (1 µM) and BSA with other complexes (5 µM).

S8. MTT ((3-(4,5-dimethylthiazol-2-yl)-2,5-diphenyltetrazolium bromide) Assay

The cytotoxicity of the Ru(II)-arene complexes was evaluated in vitro on human breast cancer and triple-negative breast cancer cell lines (MCF-7, MDA-MB-231), using the 3-(4,5-dimethylthiazol-2yl)-2,5-diphenyl tetrazolium bromide (MTT) assay.[10] These cell lines were grown at 37°C in a humidified environment containing 5% CO2 and 95% air in standard Dulbecco's modified Eagle's medium (DMEM) supplemented with 10% fetal bovine serum (FBS). Cells were planted in 96-well microplates at a density of 1×10^4 cells per well with the appropriate medium for each cell line. The plates were then incubated at 37 °C for 24 hours. The produced compounds were then dissolved in DMSO and put to the wells, where they were incubated for another 24 hours. After incubation, MTT dye solution (10 µL, 5 mg/mL) was added to each well. The plates were then incubated at 37°C for 4 hours. Following that, DMSO was applied to the wells before measuring absorbance at 570 nm. The IC_{50} values for each compound, which represent the concentration at which cell viability is reduced by 50%, were calculated using a plot of percentage cell viability against compound concentration. The percentage cell viability of each chemical was estimated using the following formula (**Equation S4**):

Cell viability (%) = (Absorbance of treated cells / Absorbance of control cells) × 100 (**Equation S4**)

This assay facilitated the determination of IC_{50} values, offering significant insights into the cytotoxic impact of the compounds on the examined cell lines and their potential as anticancer medicines.

S9. Fluorescence staining

AO-EB (Acridine Orange-Ethidium Bromide) Staining Experiment:

MDA-MB-231 cells were treated with **RuPNPT**, **RuPNMT**, and cisplatin as a control. The cells were planted at a density of 5,000 cells per well in 24-well plates and treated at 37°C for 24 hours to assess apoptosis. The cells were then treated to various amounts of cisplatin (0.9 µM), **RuPNPT** (0.4 µM), and **RuPNMT** (0.4 µM). After another 24 hours of incubation, a staining solution with AO (acridine orange) and EB (ethidium bromide) was added to each well (500 µL staining solution with 10 µL of AO and EB at 100 µg/mL each). Following initial observation with a fluorescence microscope (Olympus BX-60, Japan), at least three randomly selected microscopic fields were evaluated to determine the proportion of apoptotic cells.

Apoptosis ratio (%) = (Number of cells stained with orange fluorescence/ Number of cells stained with green fluorescence) X 100

S10. Flow Cytometry Analysis

To investigate the cell death mechanism, specifically apoptosis produced by the active complexes (**RuPNPT** and **RuPNMT**), the Annexin V-fluorescein-5-isothiocyanate (FITC)/propidium iodide (PI) detection kit from BioLegend in San Diego was used. MDA-MB-231 cells were collected and suspended in an annexin-binding buffer after being exposed to the active complexes. 10^5 cells were treated for 15 minutes at room temperature and in darkness with 5 µL of annexin V-FITC and 15 µL of PI solution. After incubation, 400 µL of binding buffer was added to the cells, and the samples were analyzed using a Becton Dickinson FACS Calibur flow cytometer. This study aided in the identification of the cell death mechanism activated by the examined complexes.

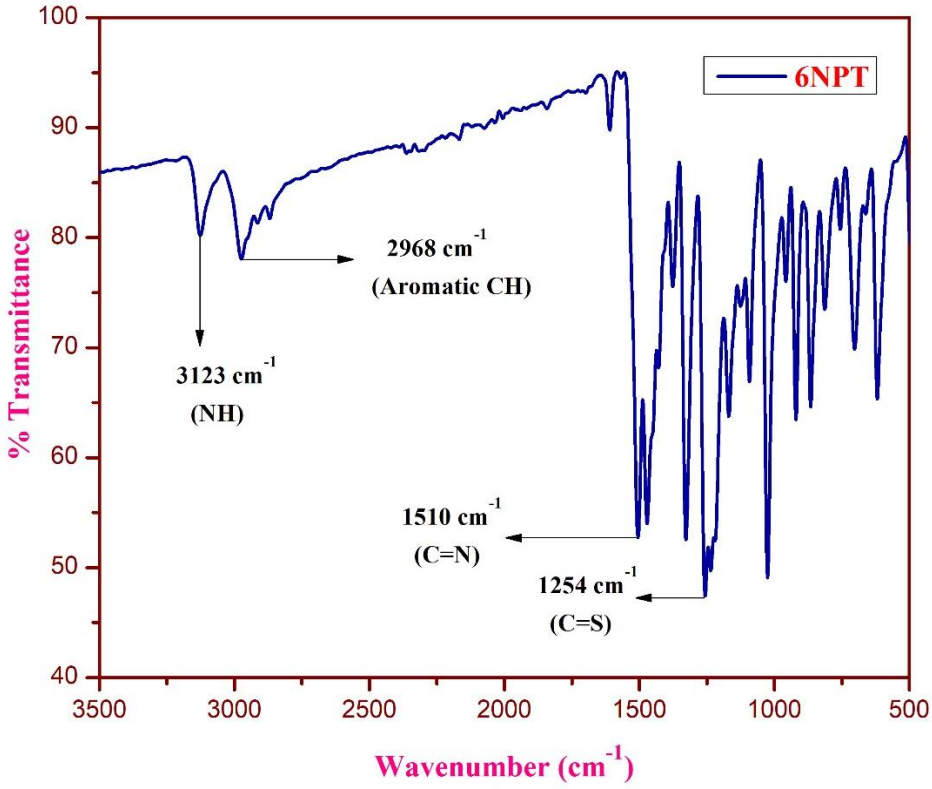

Figure S1. FT-IR Spectrum of **6NPT**

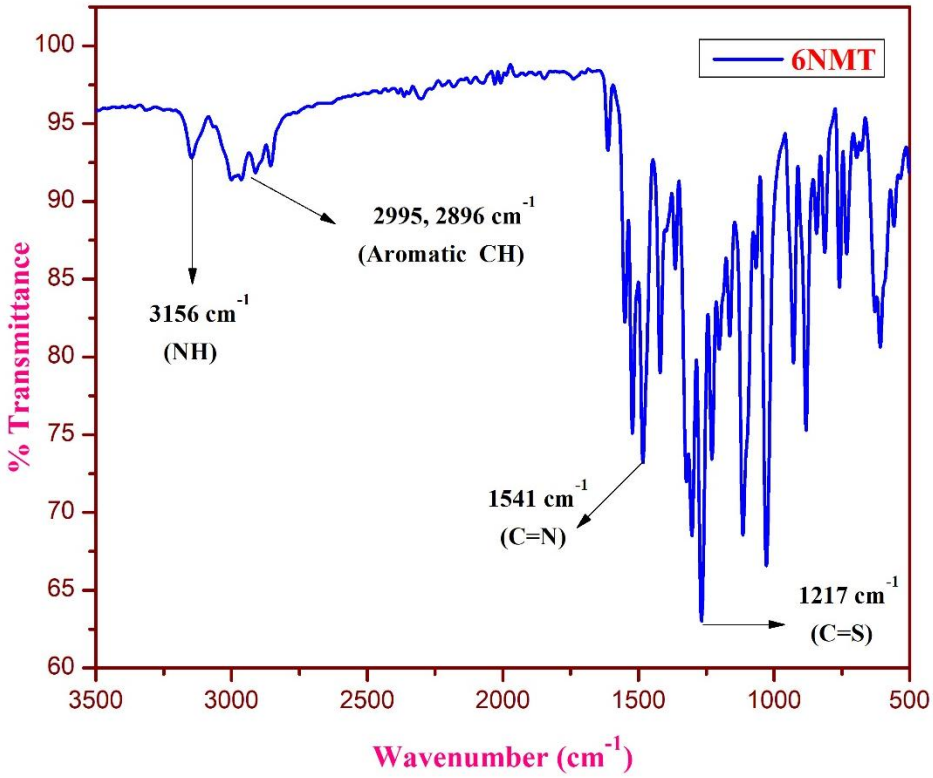

Figure S2. FT-IR Spectrum of **6NMT**

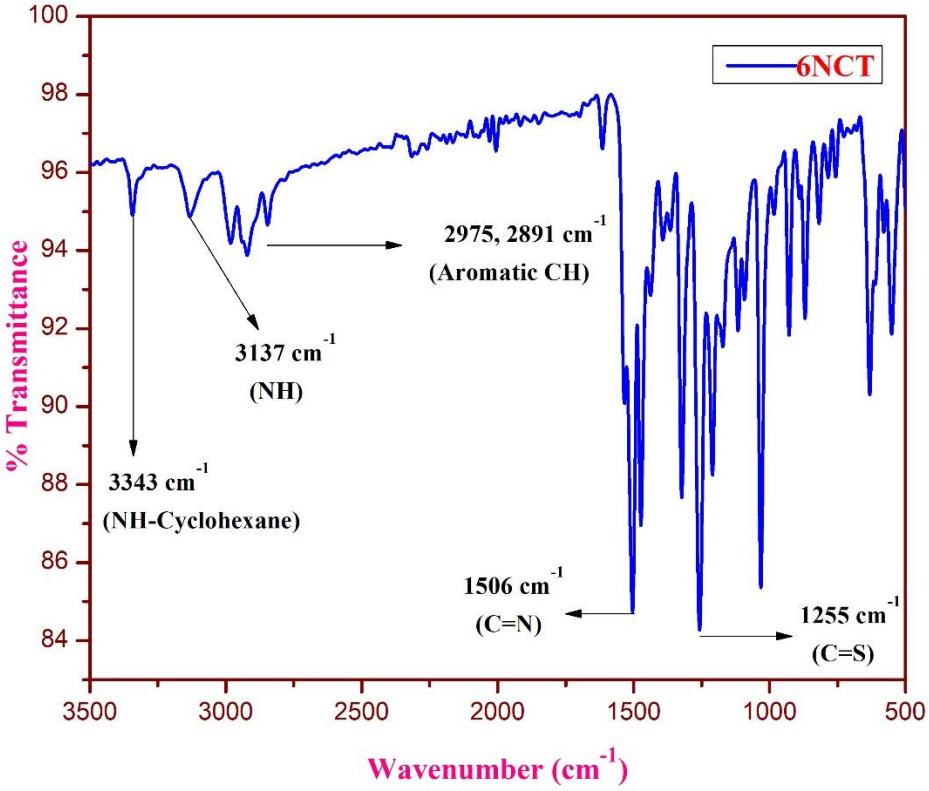

Figure S3. FT-IR Spectrum of **6NCT**

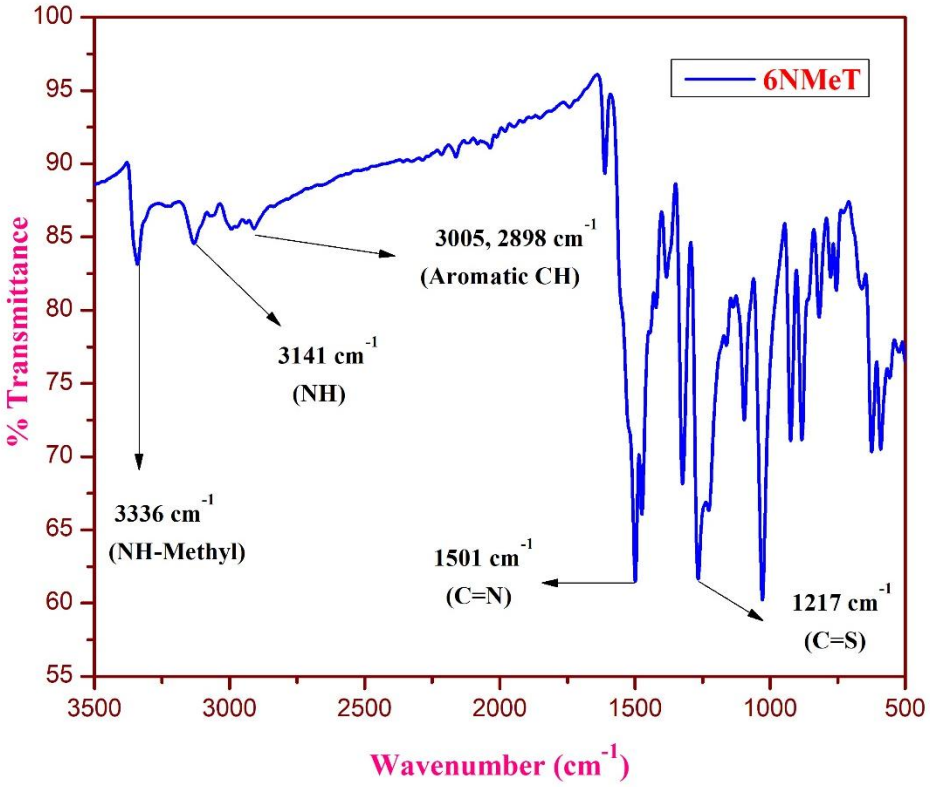

Figure S4. FT-IR Spectrum of **6NMeT**

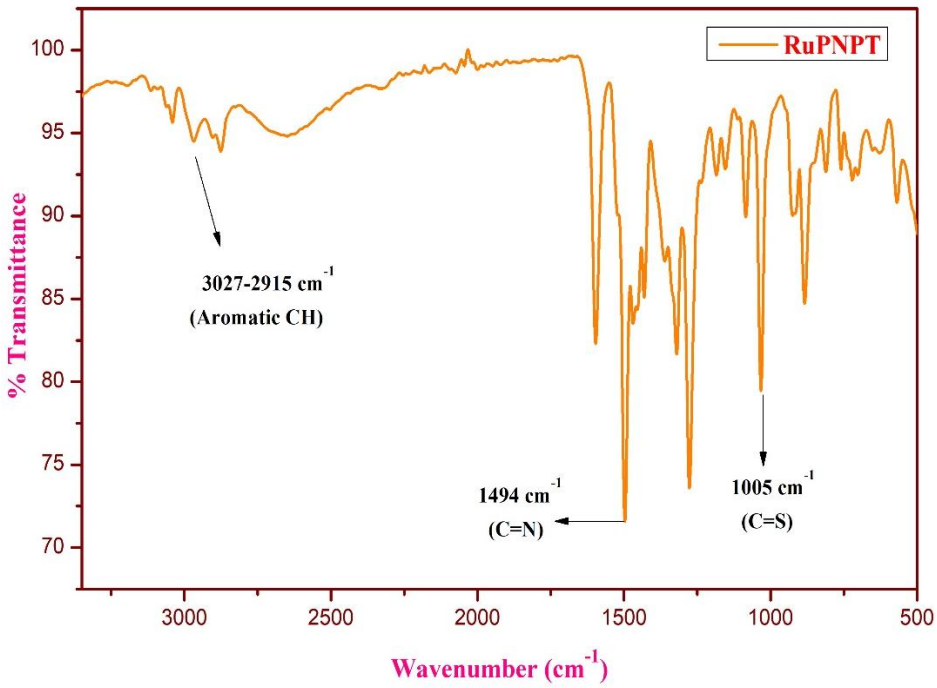

Figure S5. FT-IR Spectrum of **RuPNPT**

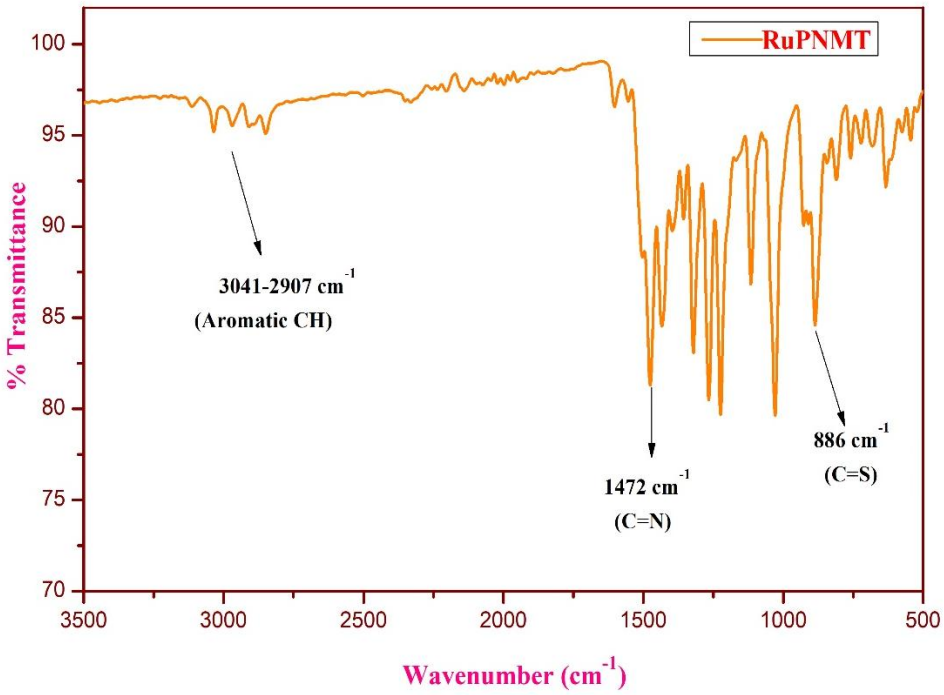

Figure S6. FT-IR Spectrum of **RuPNMT**

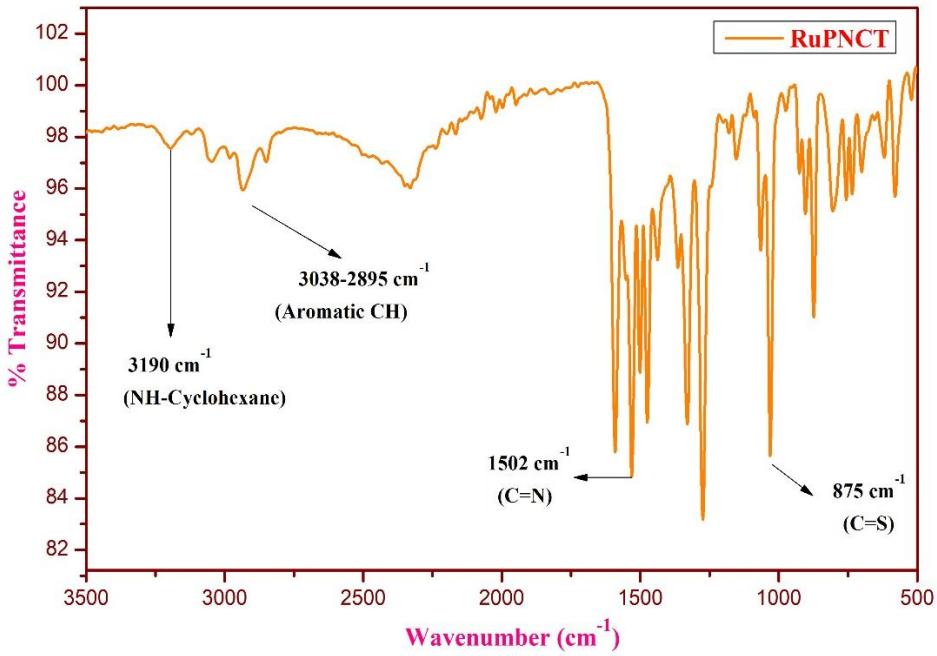

Figure S7. FT-IR Spectrum of **RuPNCT**

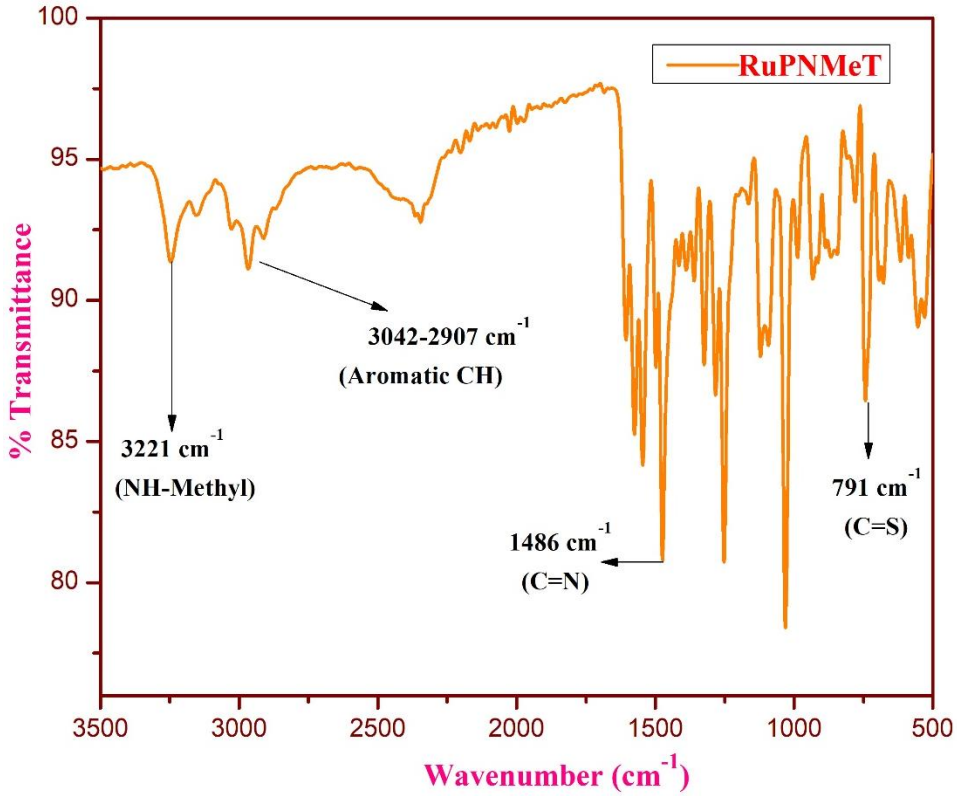

Figure S8. FT-IR Spectrum of **RuPNMeT**

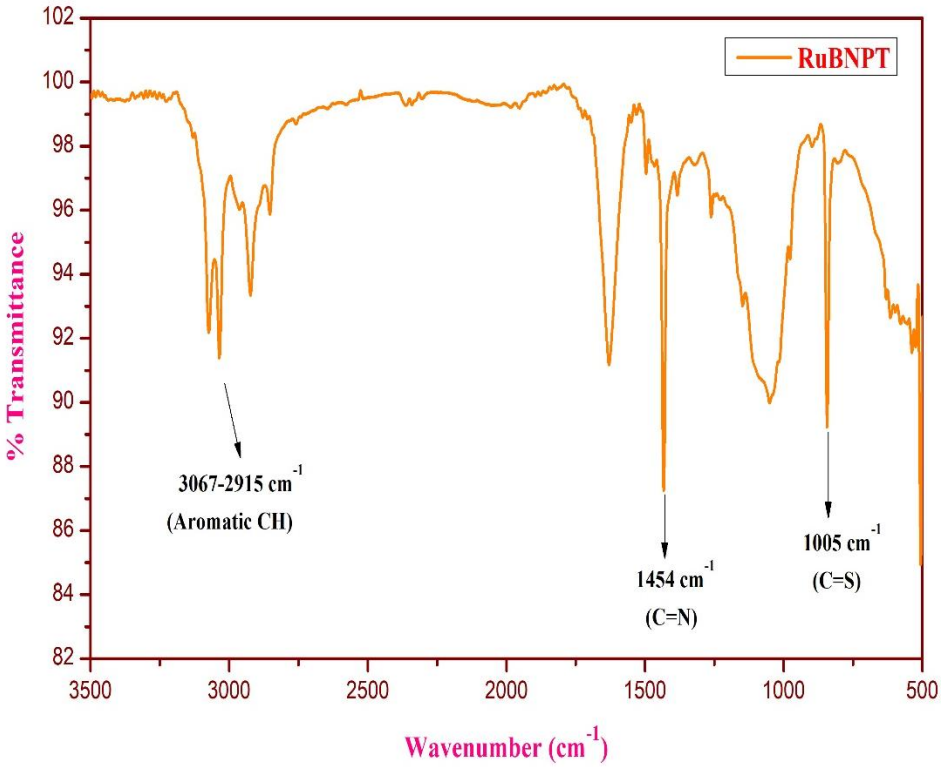

Figure S9. FT-IR Spectrum of **RuBNPT**

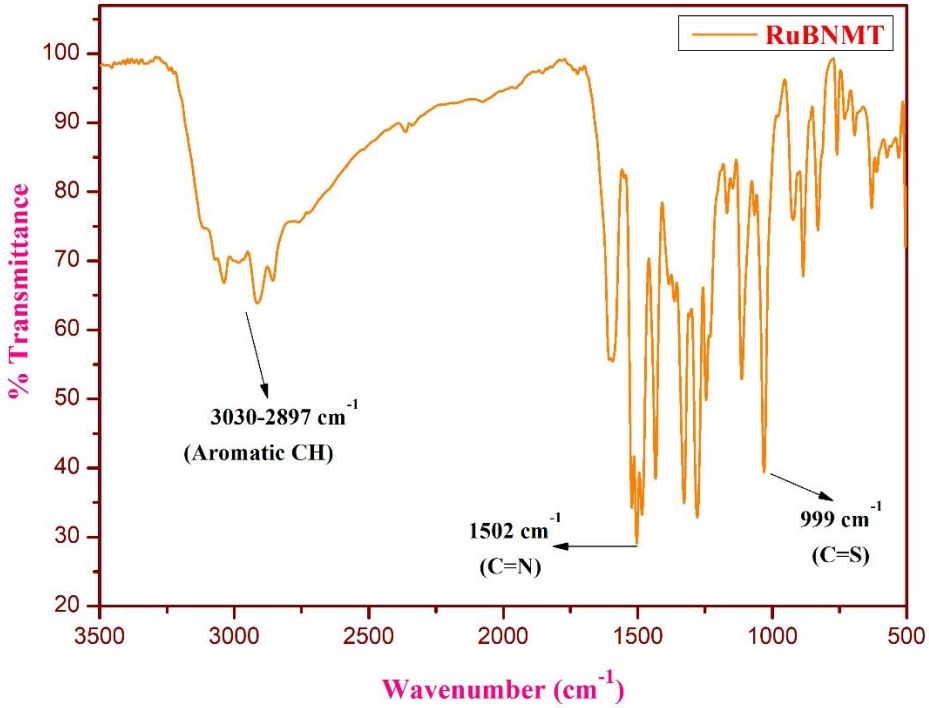

Figure S10. FT-IR Spectrum of **RuBNMT**

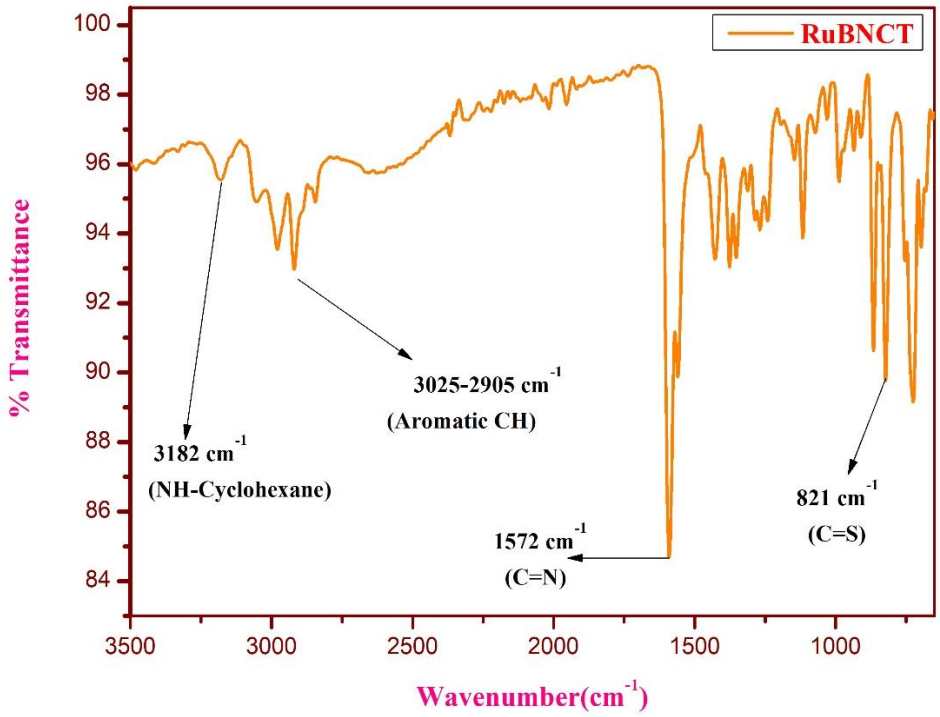

Figure S11. FT-IR Spectrum of **RuBNCT**

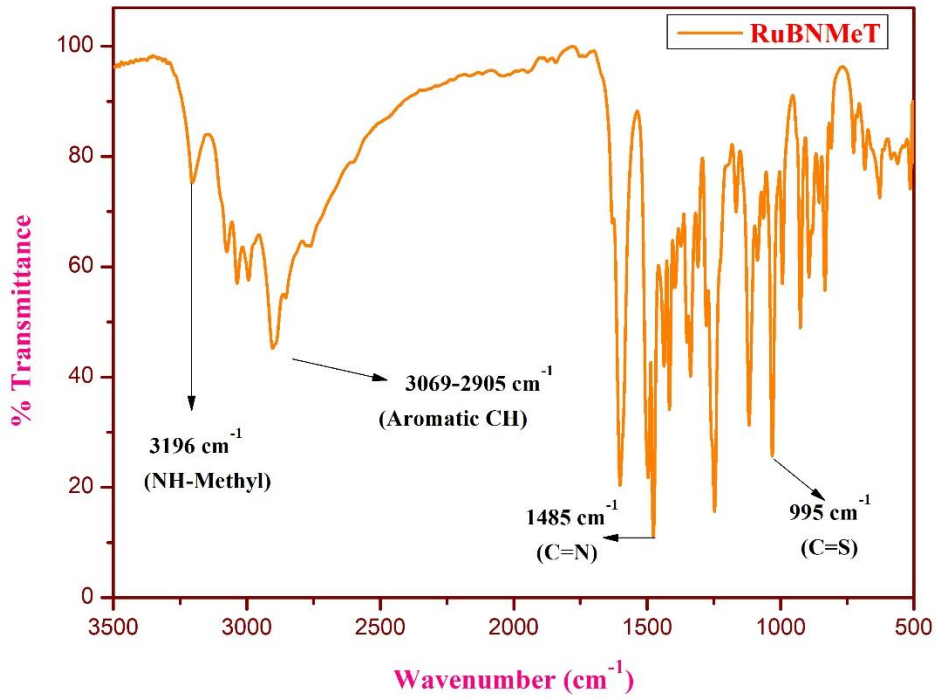

Figure S12. FT-IR Spectrum of **RuBNMeT**

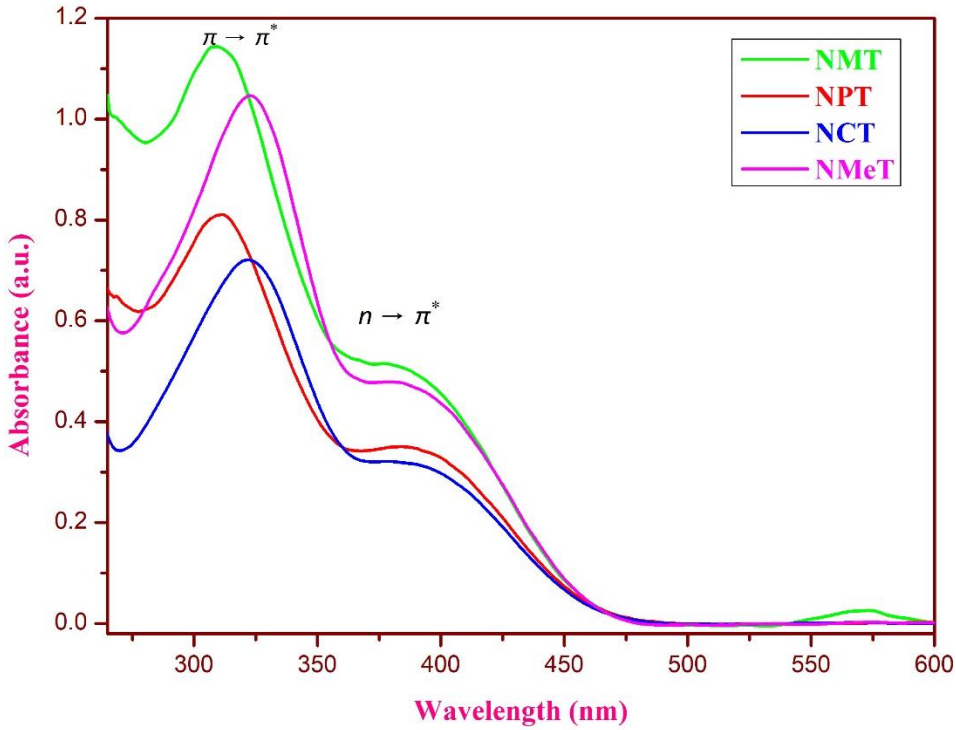

Figure S13. UV-Visible Spectrum of all ligands

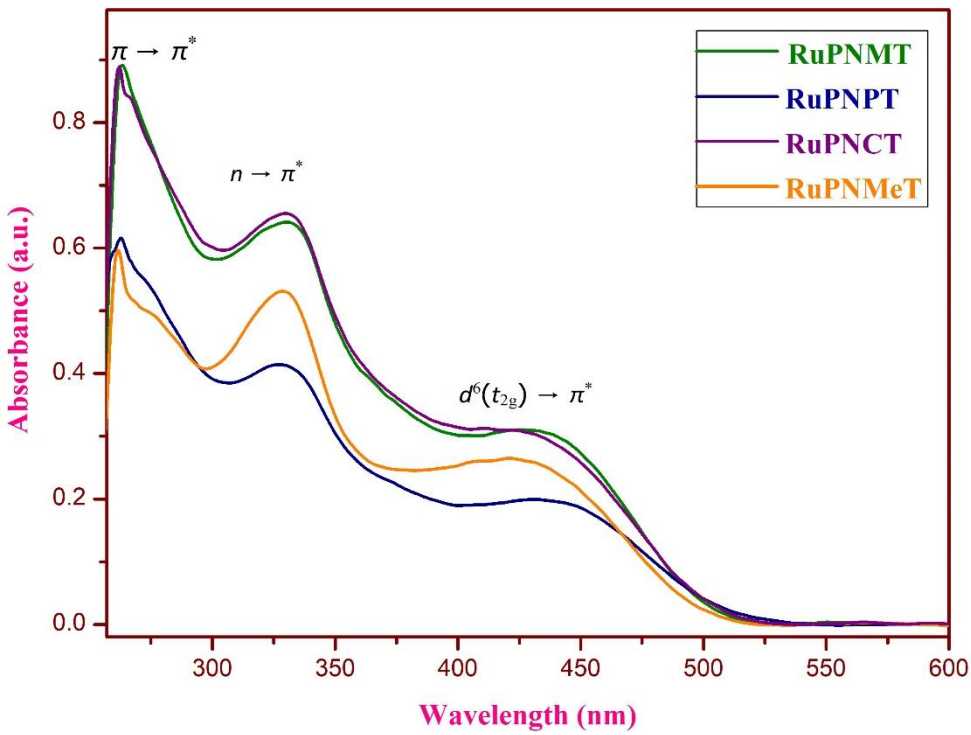

Figure S14. UV-Visible Spectrum of Ru-P-cymene complexes

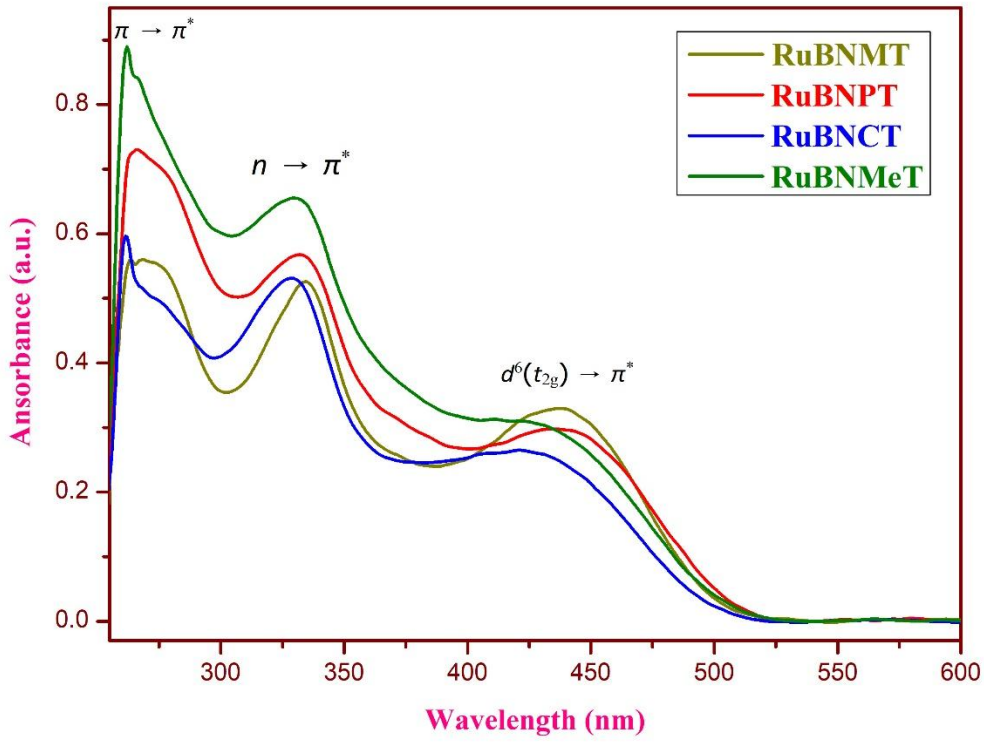

Figure S15. UV-Visible Spectrum of Ru-Benzene complexes

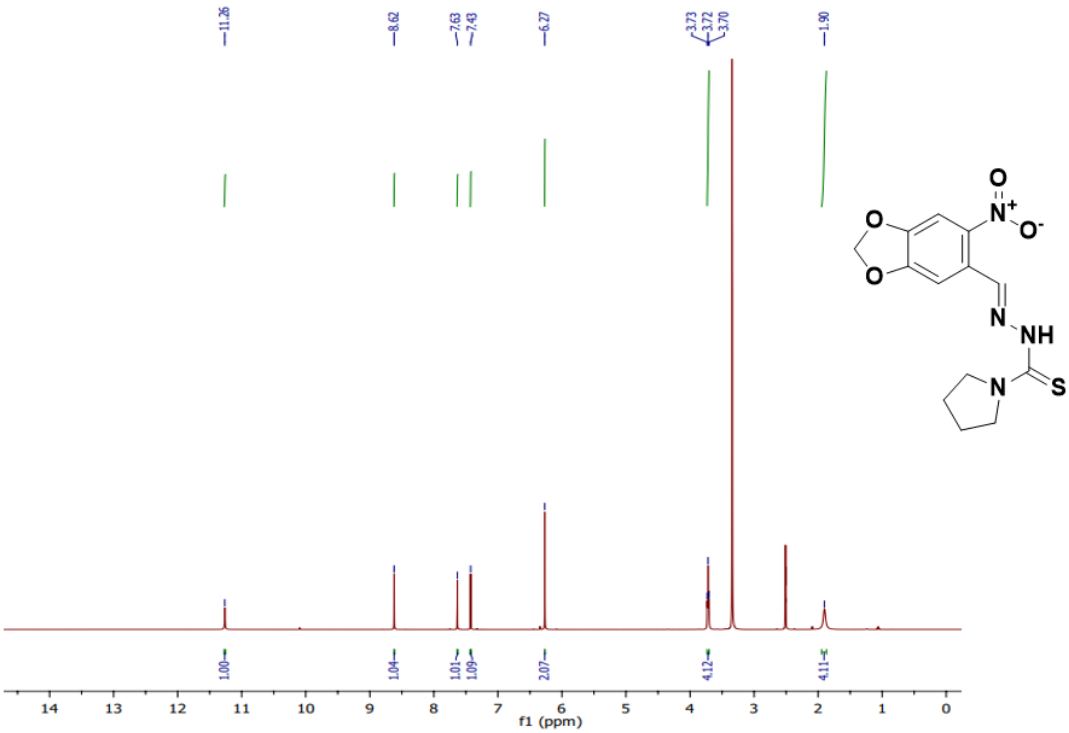

Figure S16. ^{1}H NMR Spectrum of **6NPT** in **DMSO-*d*$_6$**

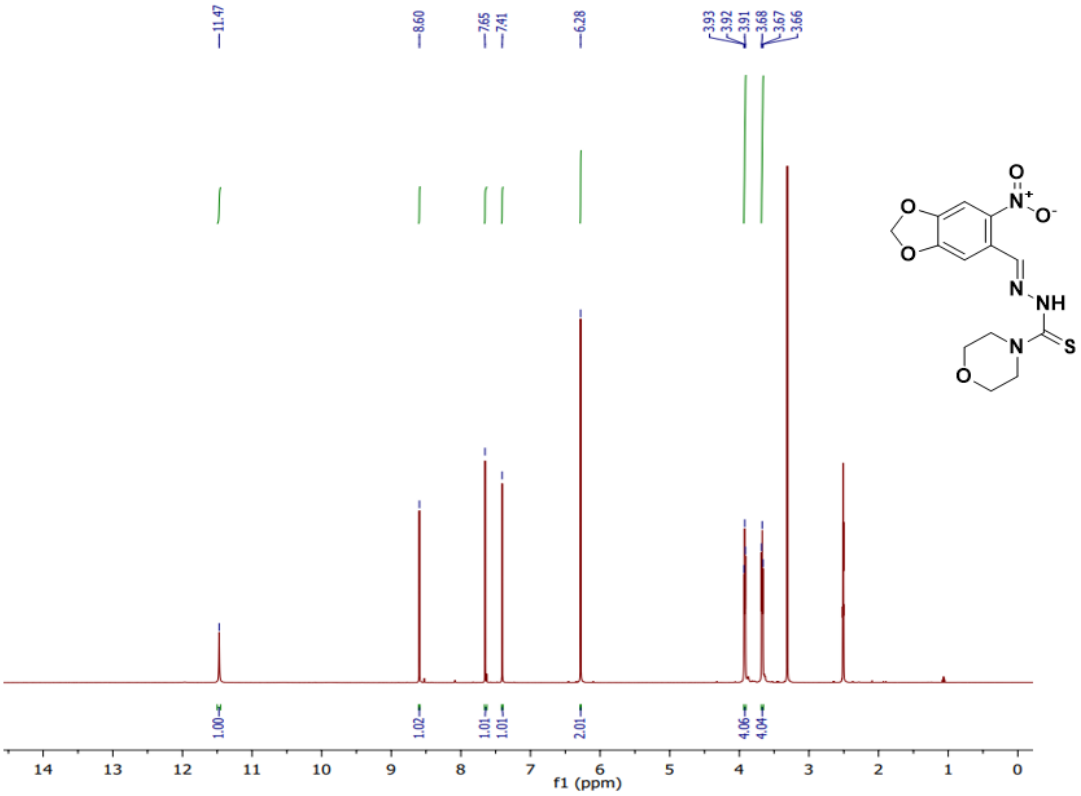

Figure S17. ^{1}H NMR Spectrum of **6NMT** in **DMSO-*d*$_6$**

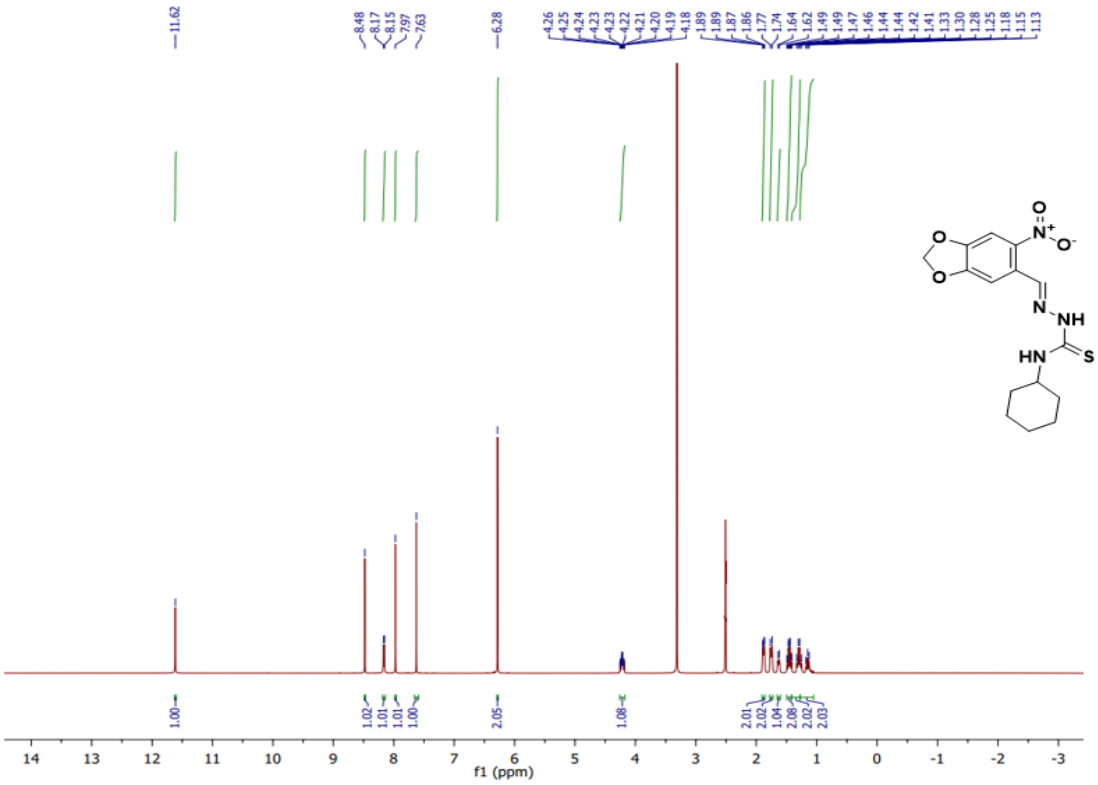

Figure S18. ^{1}H NMR Spectrum of **6NCT** in **DMSO-*d*$_6$**

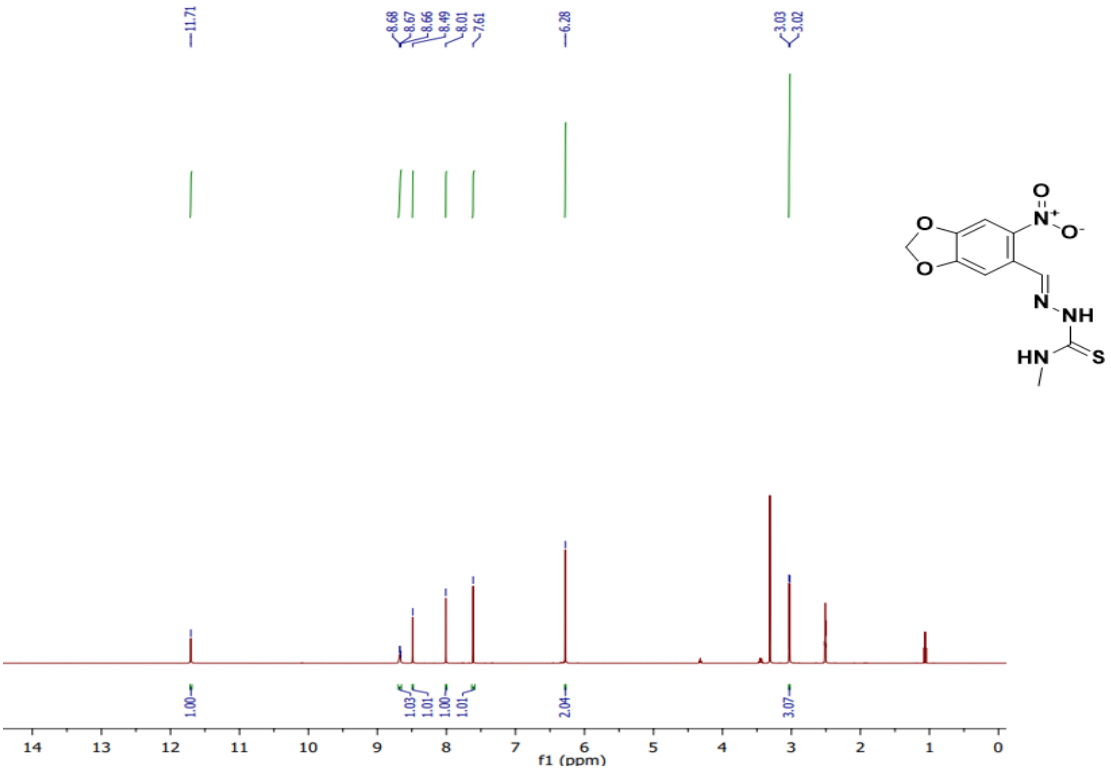

Figure S19. ^{1}H NMR Spectrum of **6NMeT** in **DMSO-*d₆***

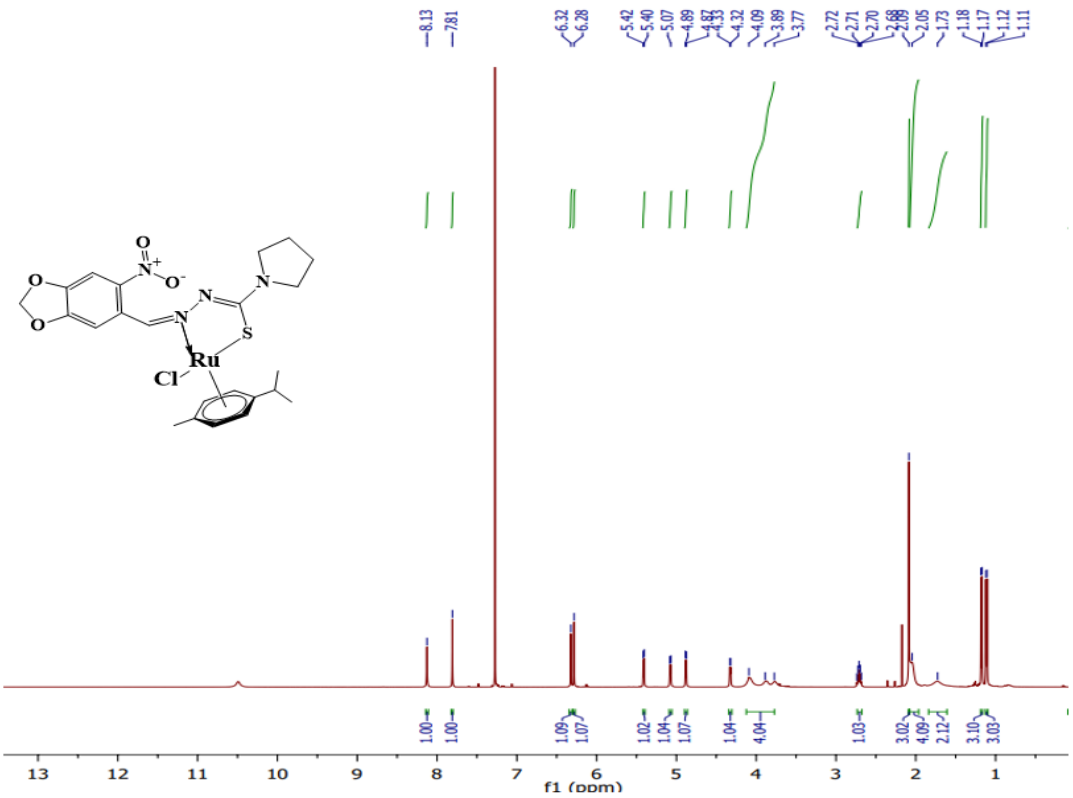

Figure S20. ^{1}H NMR Spectrum of **RuPNPT** in **CDCl₃**

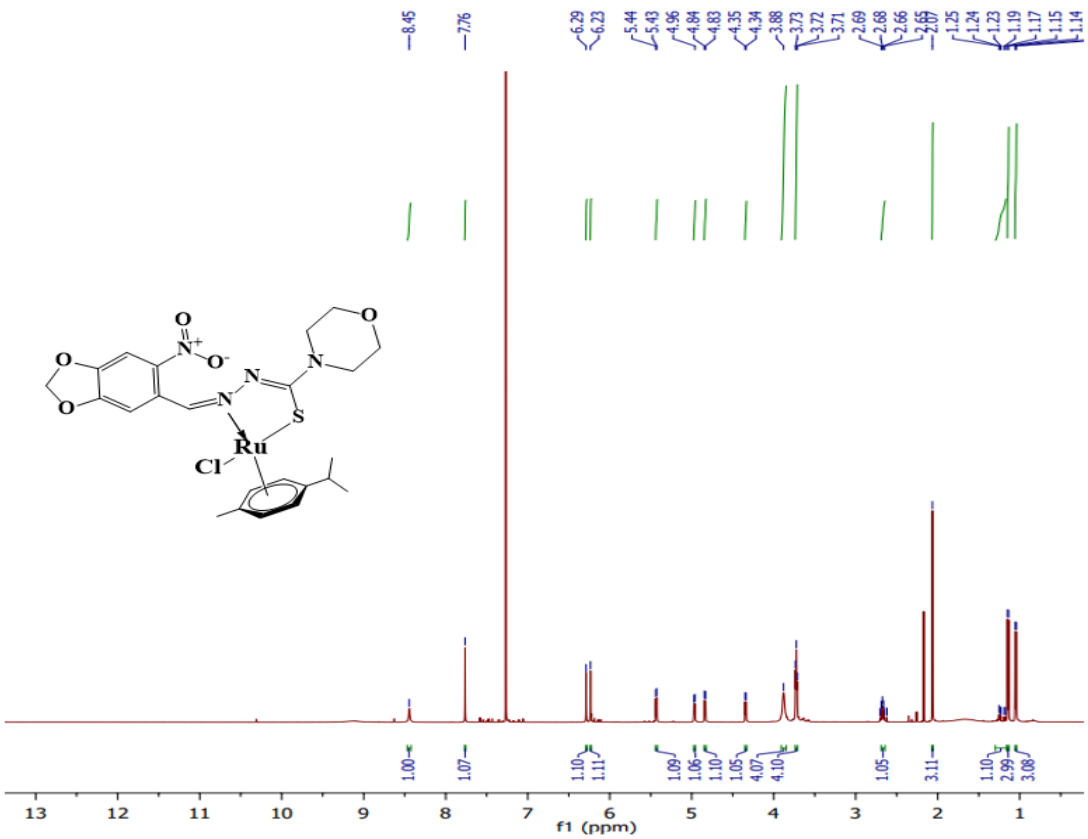

Figure S21. ^{1}H NMR Spectrum of **RuPNMT** in **CDCl3**

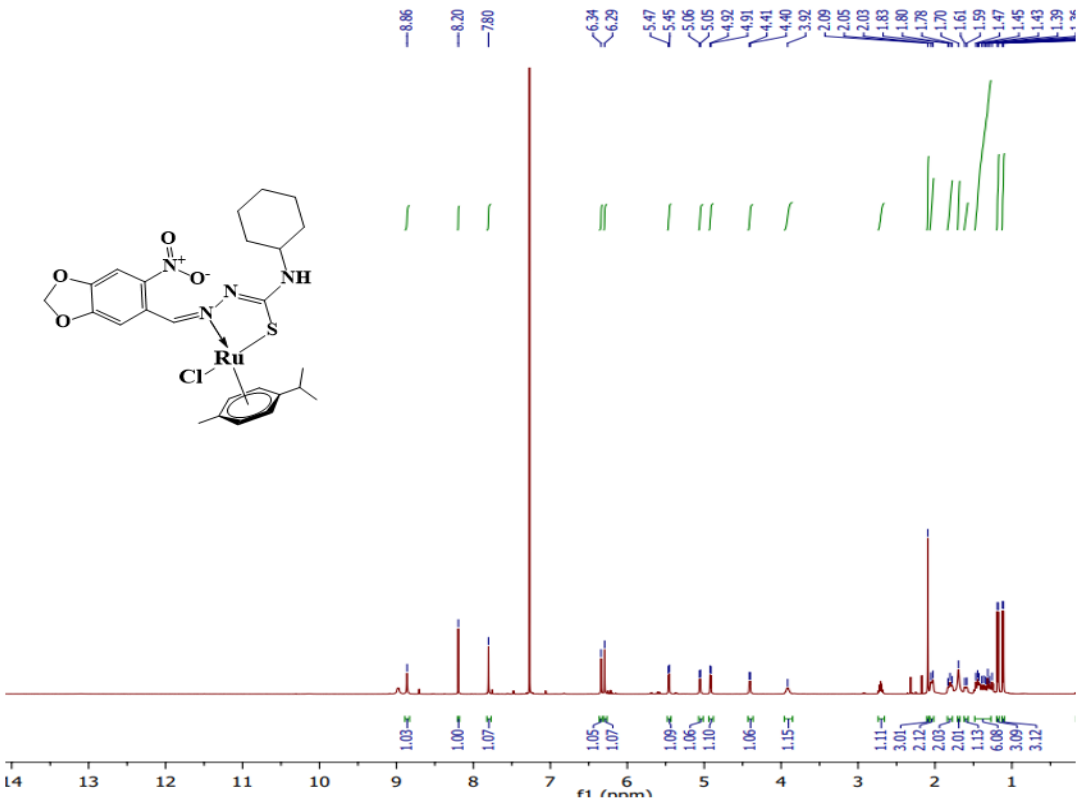

Figure S22. ^{1}H NMR Spectrum of **RuPNCT** in **CDCl3**

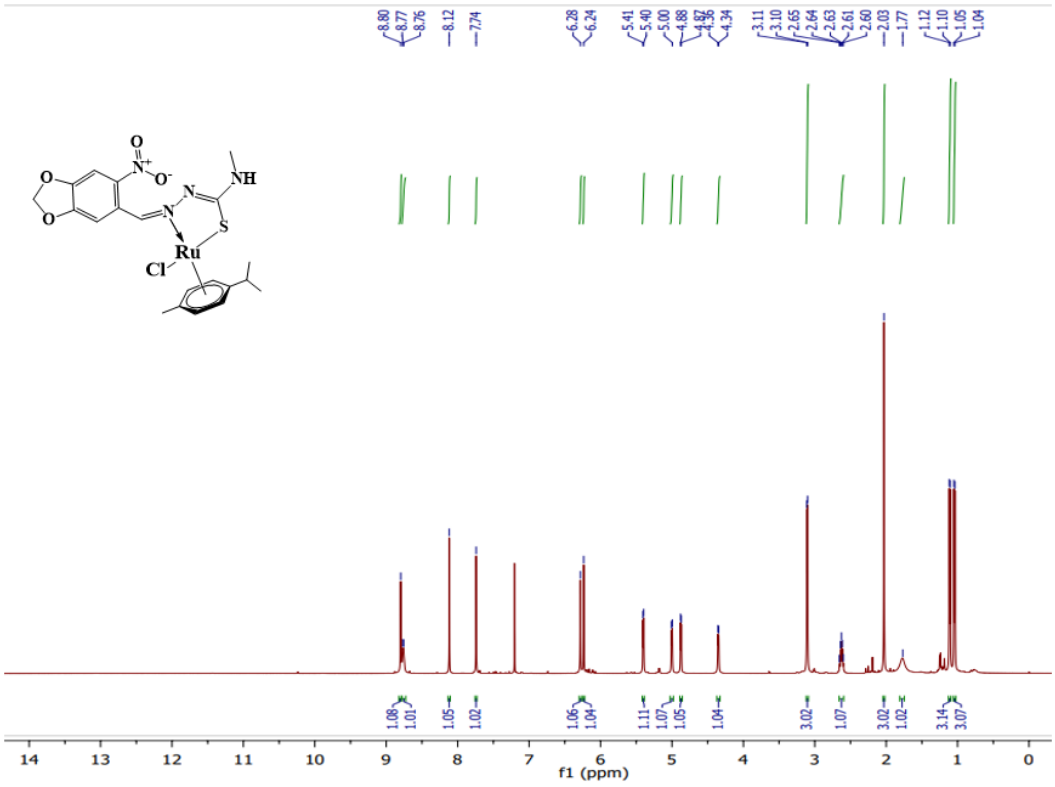

Figure S23. ^{1}H NMR Spectrum of **RuPNMeT** in **CDCl$_3$**

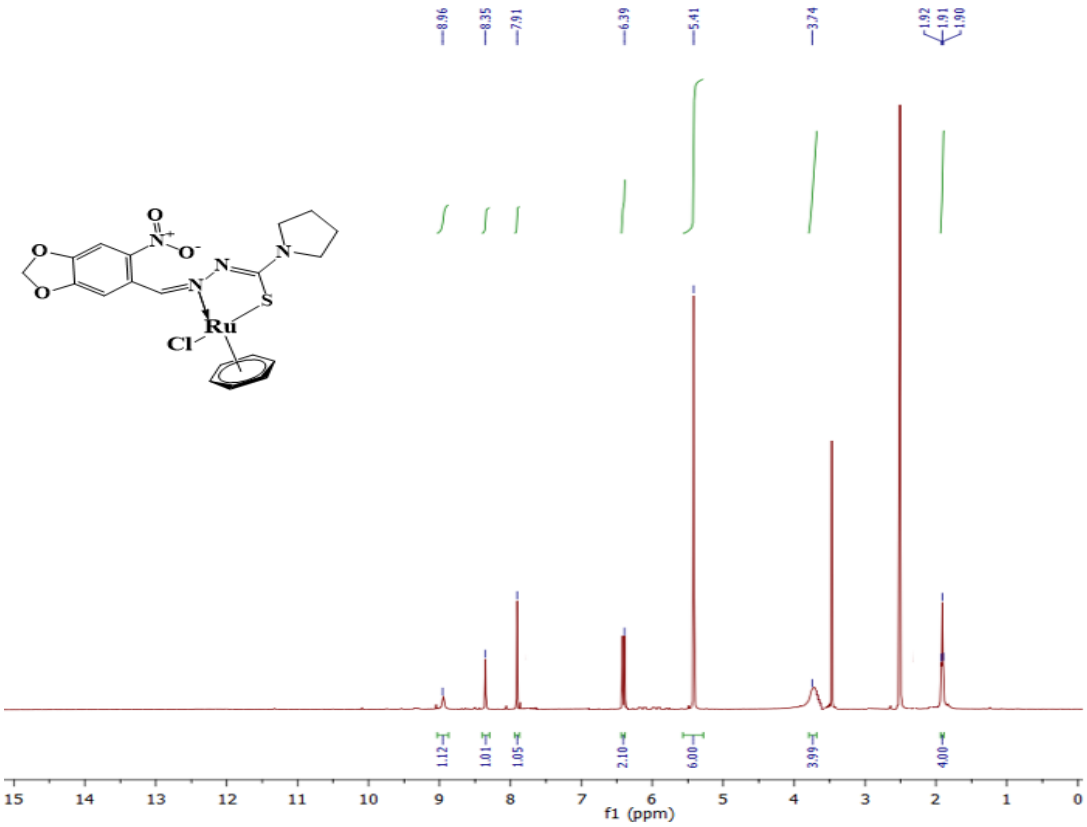

Figure S24. ^{1}H NMR Spectrum of **RuBNPT** in **DMSO-*d*$_6$**

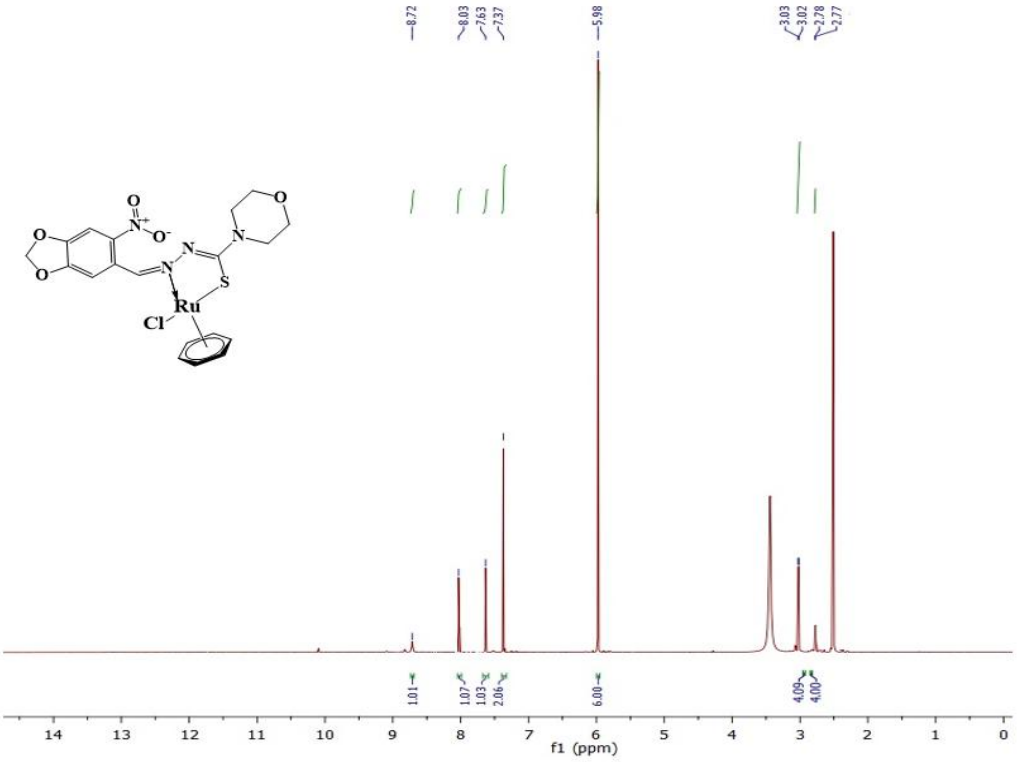

Figure S25. ^{1}H NMR Spectrum of **RuBNMT** in **DMSO-*d*$_6$**

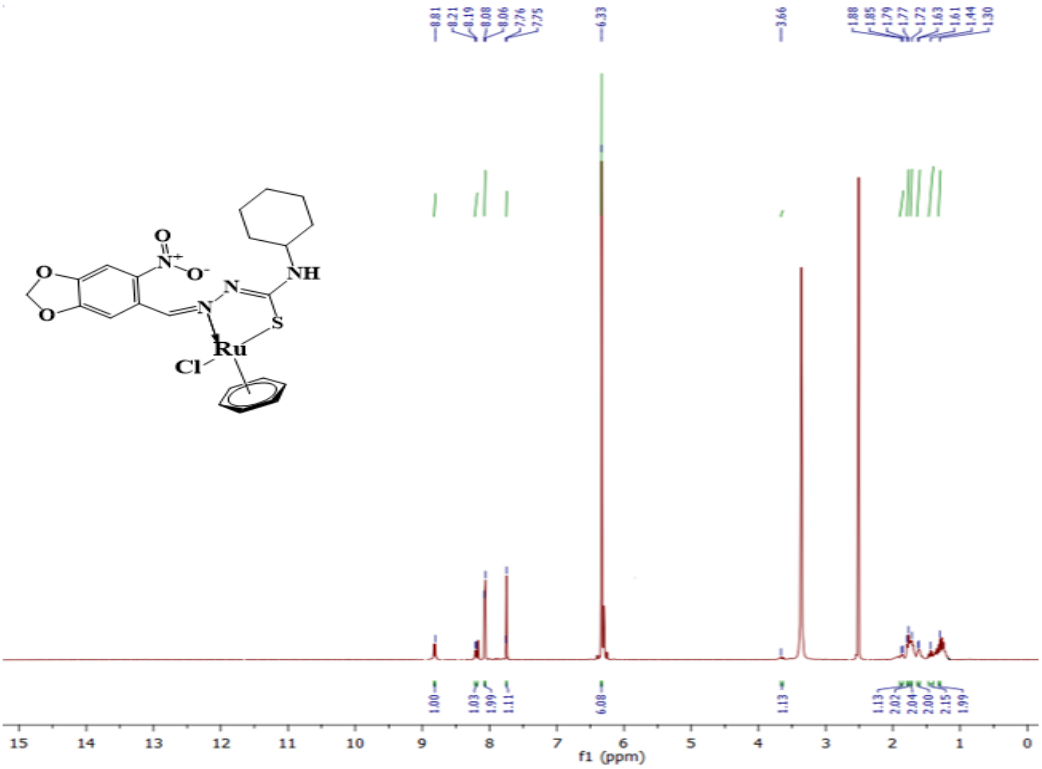

Figure S26. ^{1}H NMR Spectrum of **RuBNCT** in **DMSO-*d*$_6$**

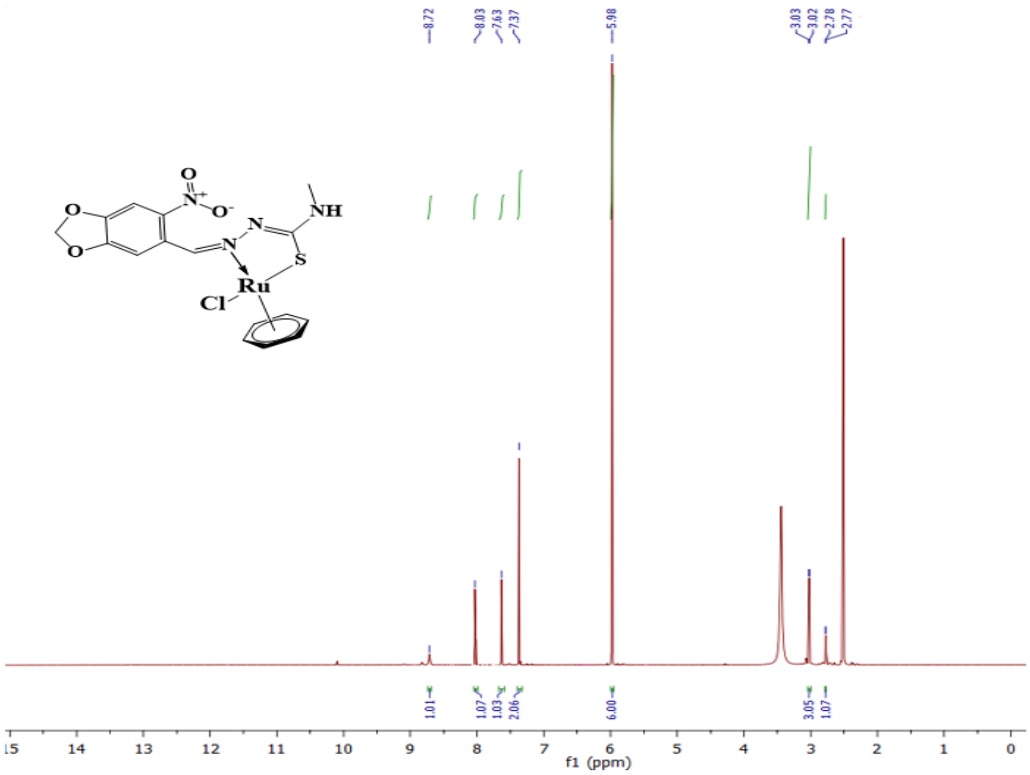

Figure S27. ^{1}H NMR Spectrum of **RuBNMeT** in **DMSO-*d*$_6$**

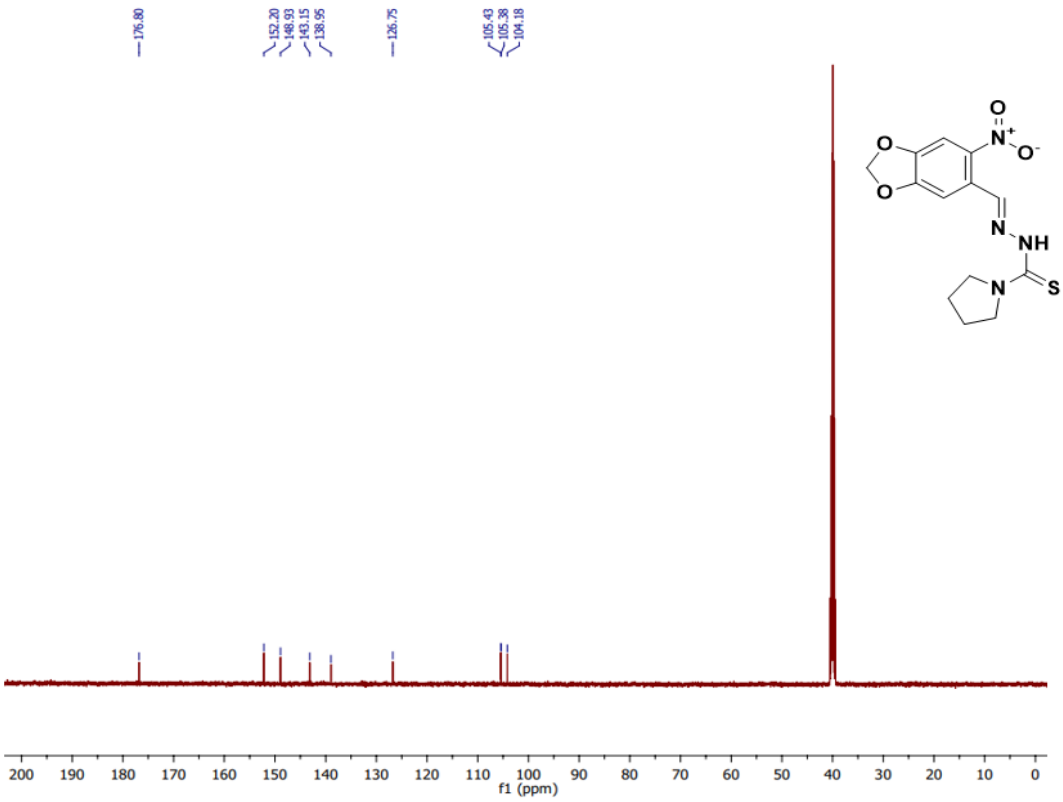

Figure S28. ^{13}C NMR Spectrum of **6NPT** in **DMSO-*d*$_6$**

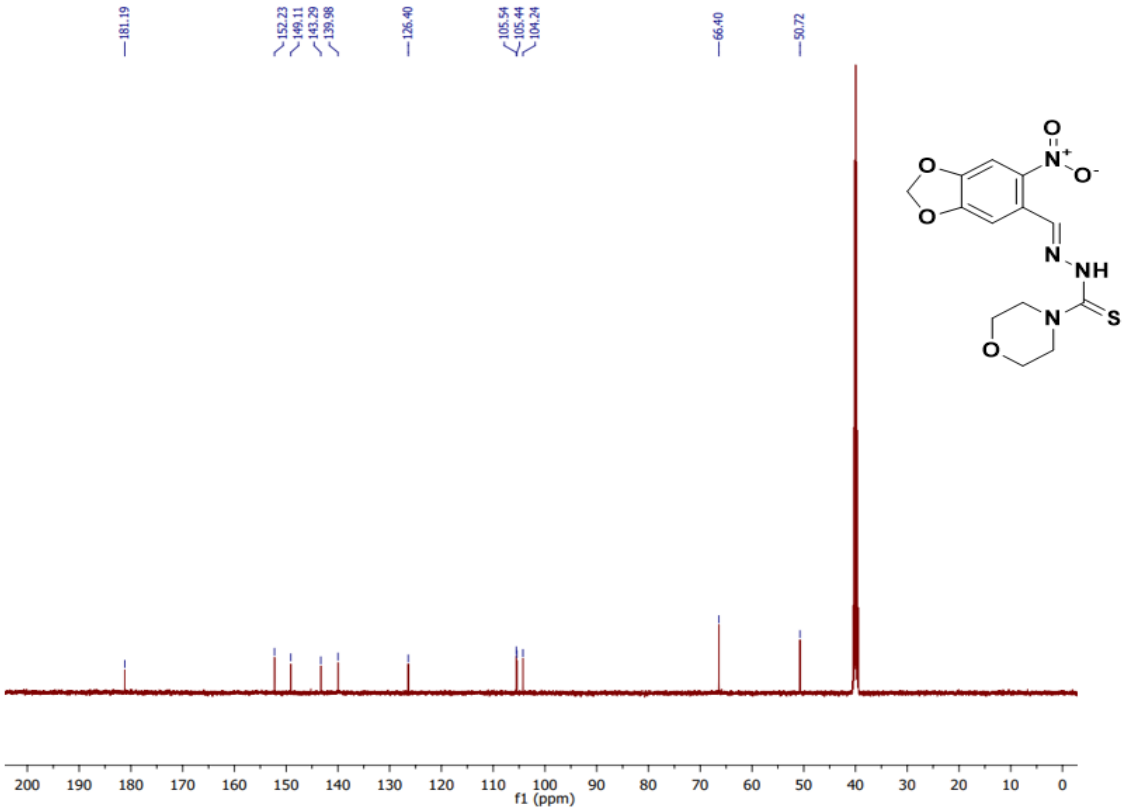

Figure S29. ^{13}C NMR Spectrum of **6NMT** in **DMSO-*d*$_6$**

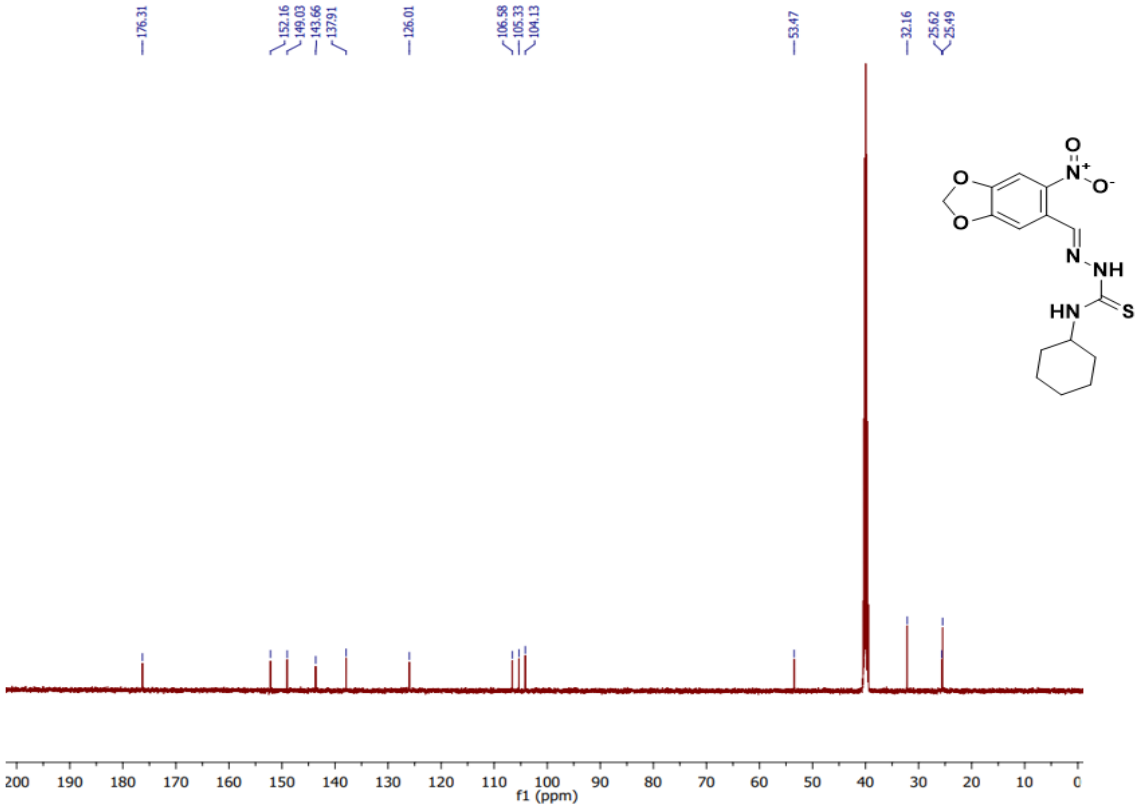

Figure S30. ^{13}C NMR Spectrum of **6NCT** in **DMSO-*d*$_6$**

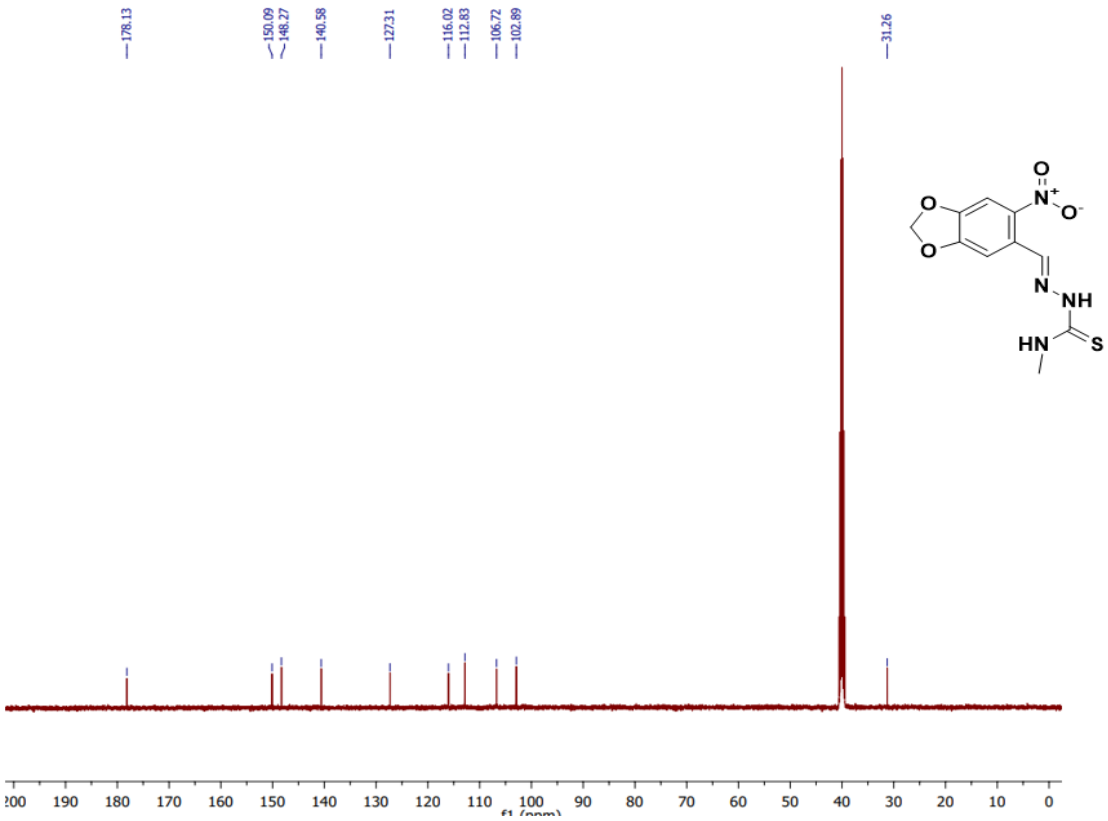

Figure S31. ^{13}C NMR Spectrum of **6NMeT** in **DMSO-*d*$_6$**

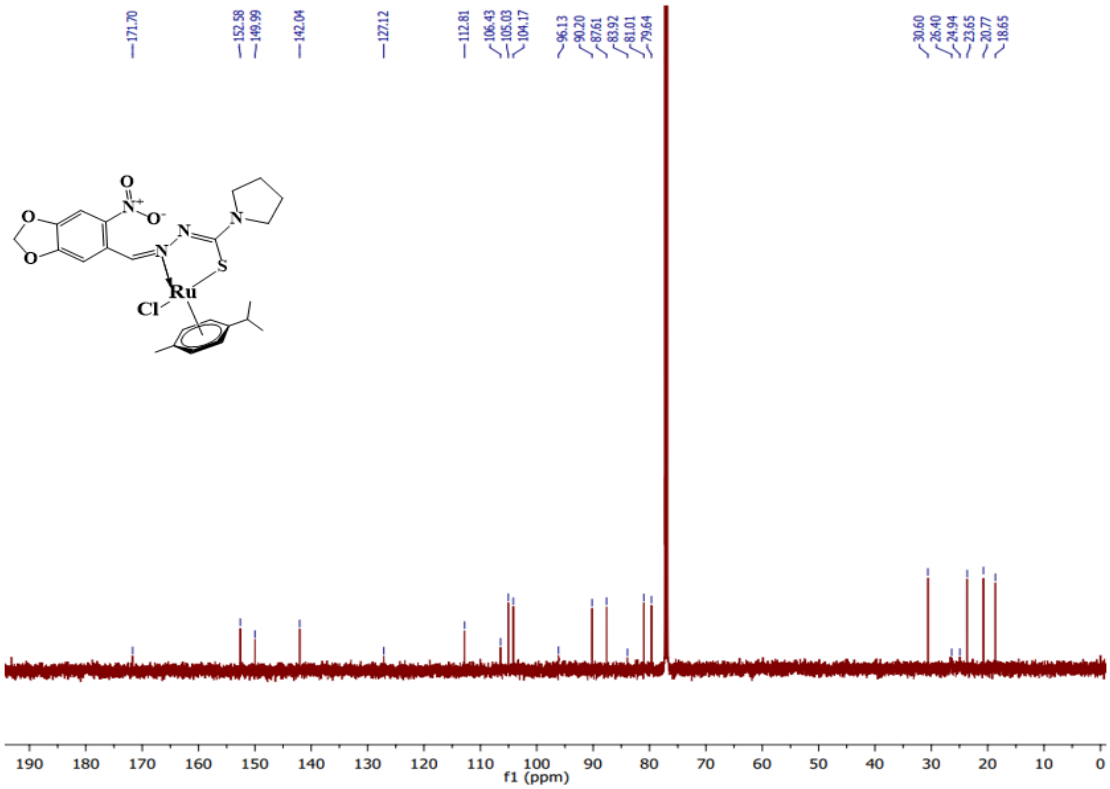

Figure S32. ^{13}C NMR Spectrum of **RuPNPT** in **CDCl$_3$**

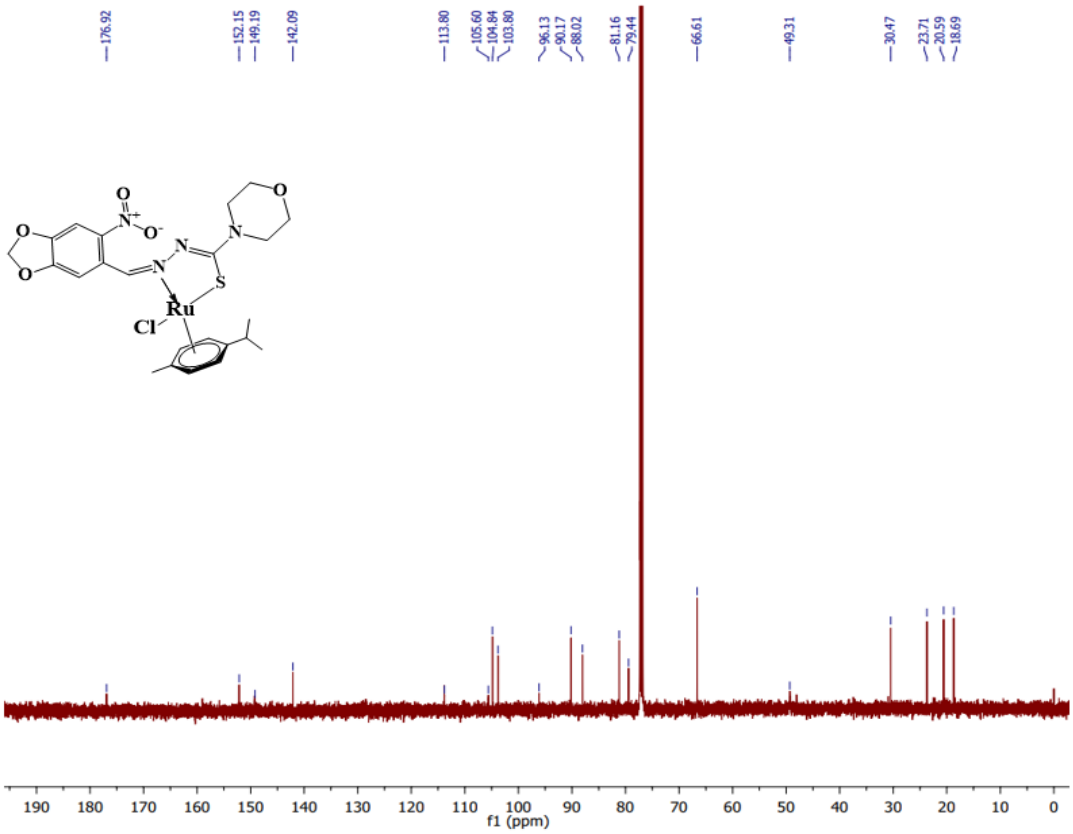

Figure S33. ^{13}C NMR Spectrum of **RuPNMT** in **CDCl$_3$**

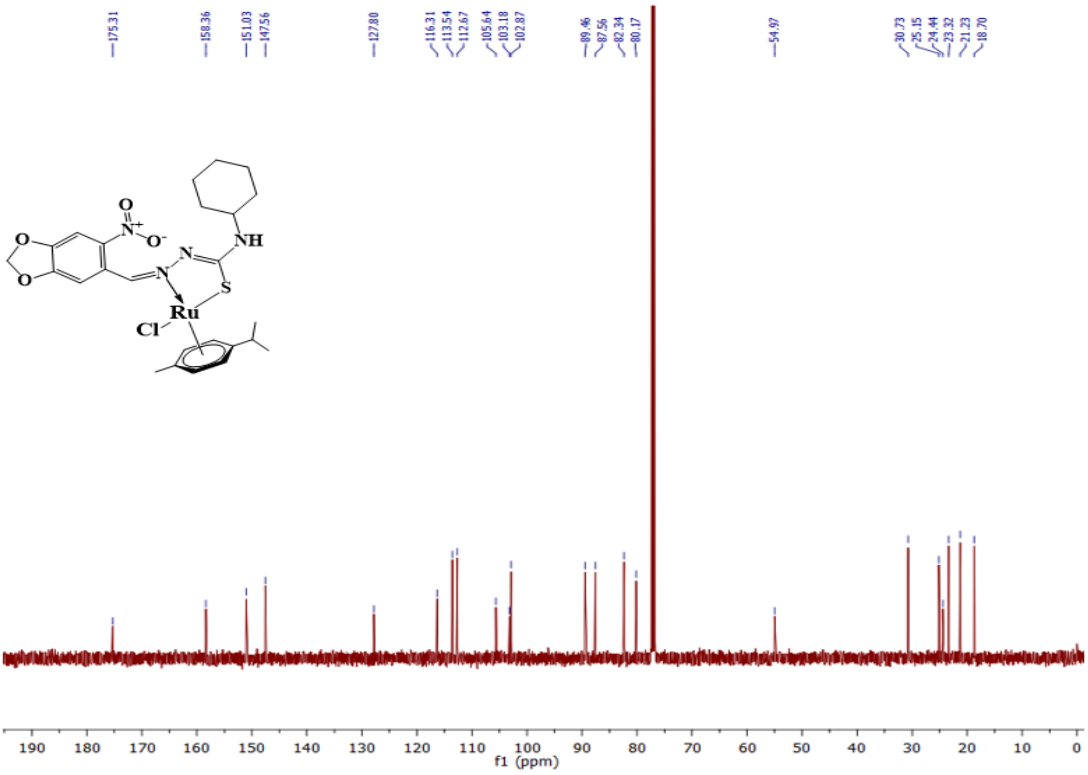

Figure S34. ^{13}C NMR Spectrum of **RuPNCT** in **CDCl$_3$**

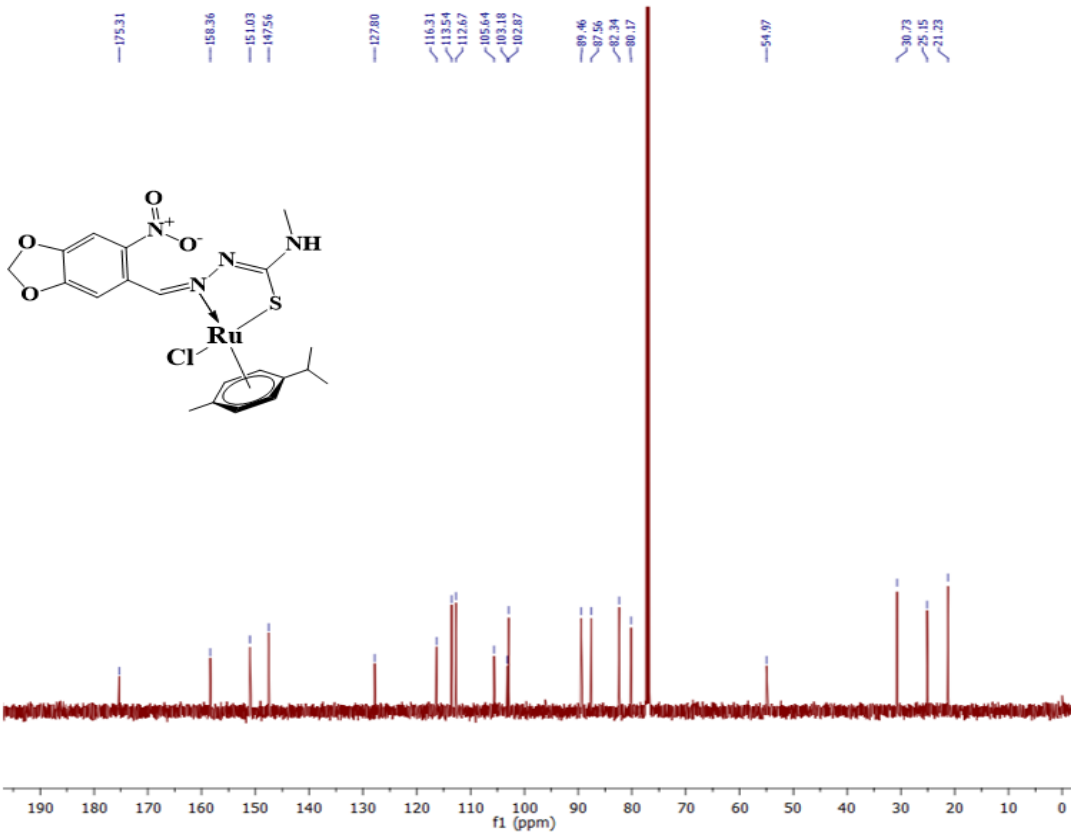

Figure S35. ^{13}C NMR Spectrum of **RuPNMeT** in **CDCl$_3$**

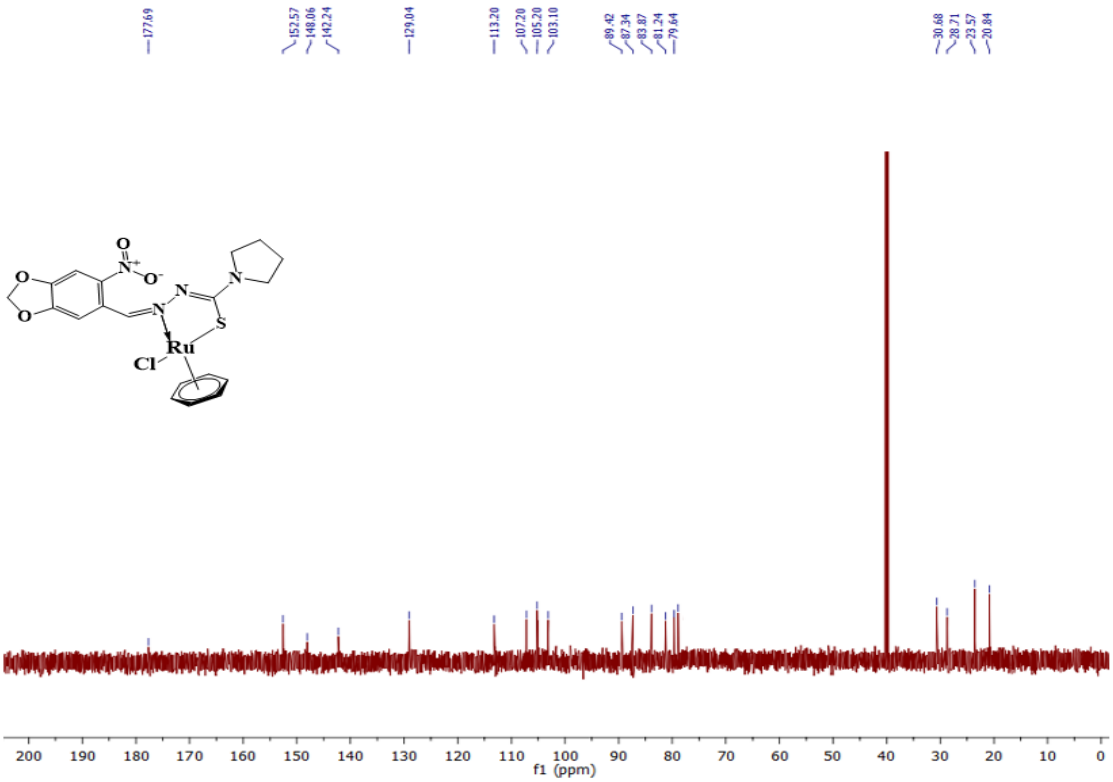

Figure S36. ^{13}C NMR Spectrum of **RuBNPT** in **DMSO-*d*$_6$**

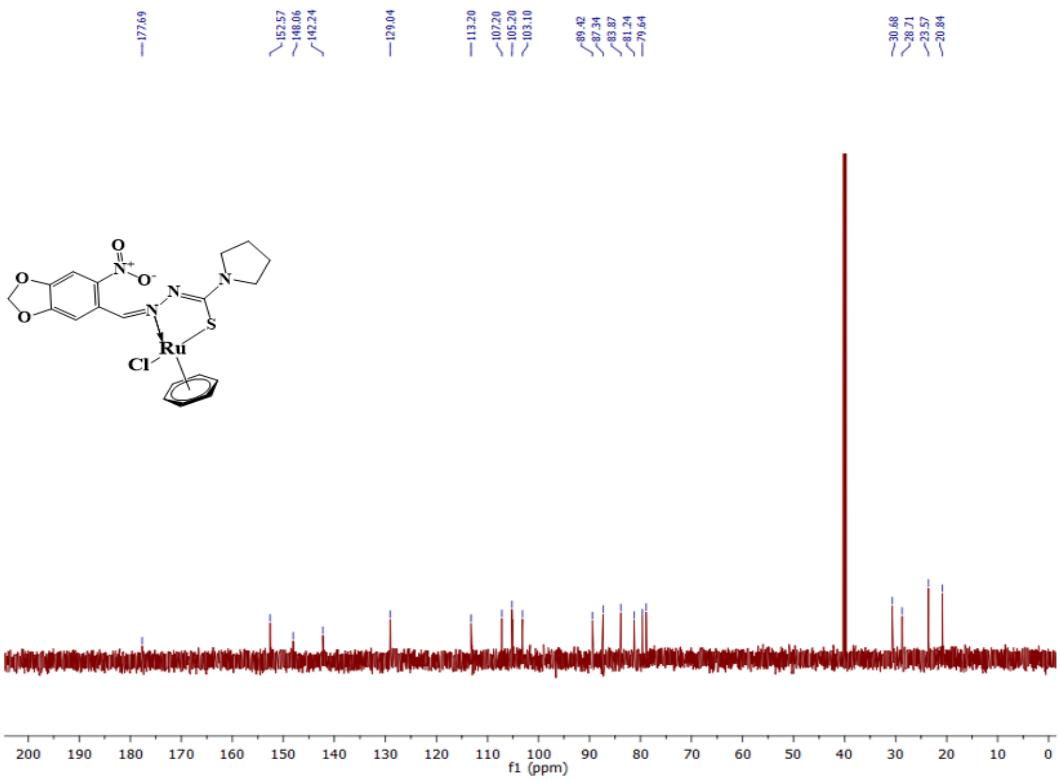

Figure S37. ^{13}C NMR Spectrum of **RuBNMT** in **DMSO-*d*$_6$**

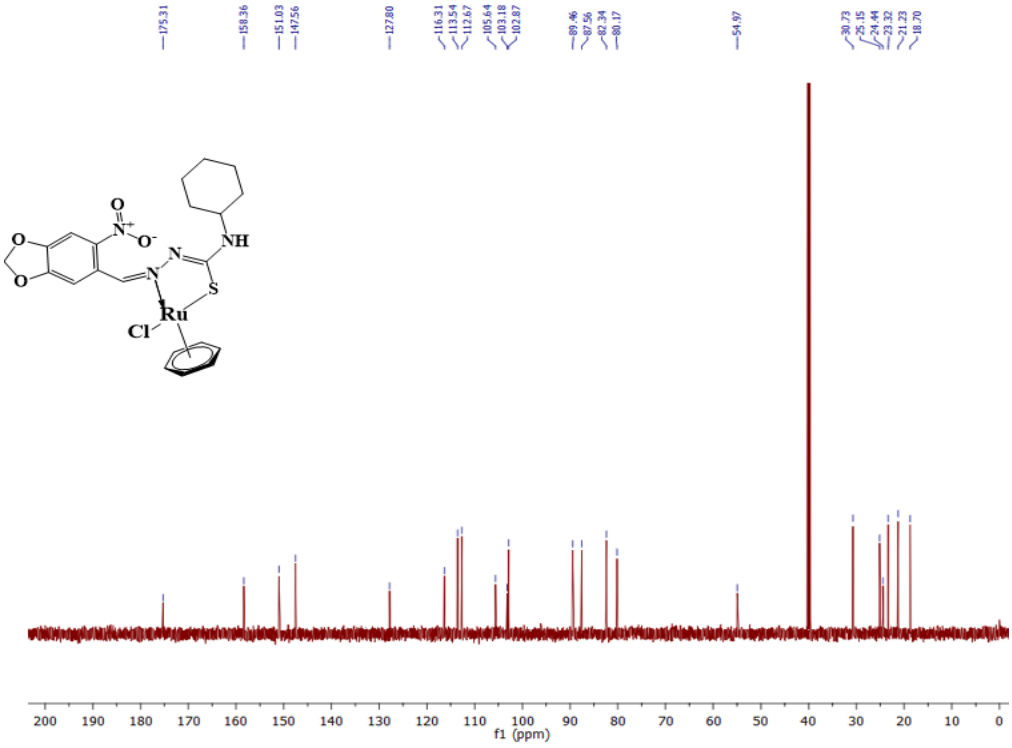

Figure S38. ^{13}C NMR Spectrum of **RuBNCT** in **DMSO-*d*$_6$**

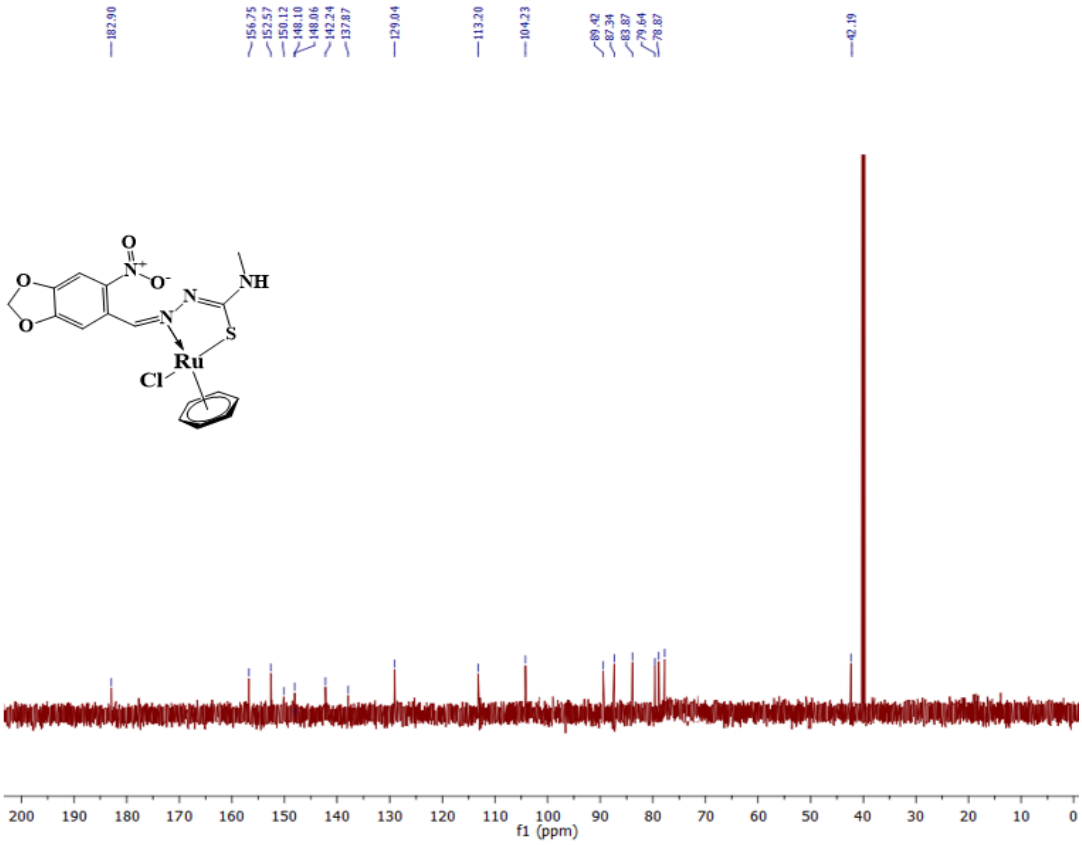

Figure S39. ^{13}C NMR Spectrum of **RuBNMeT** in **DMSO-*d*6**

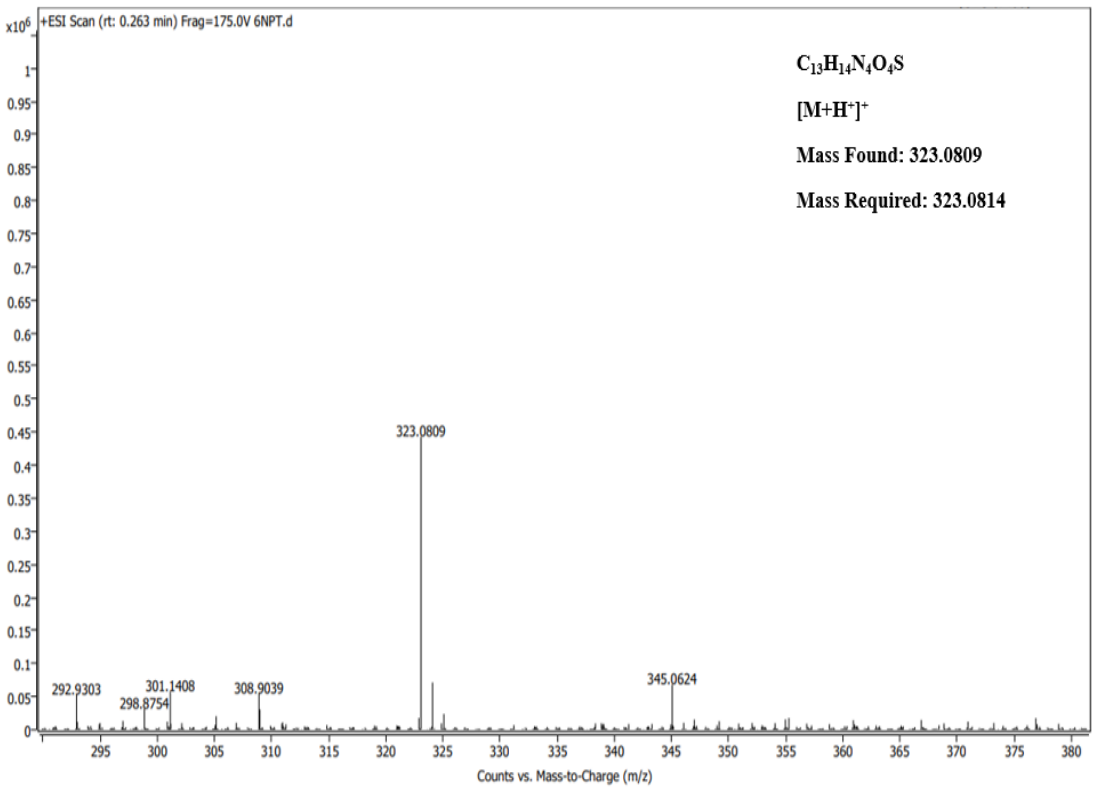

Figure S40. HRMS of **6NPT**

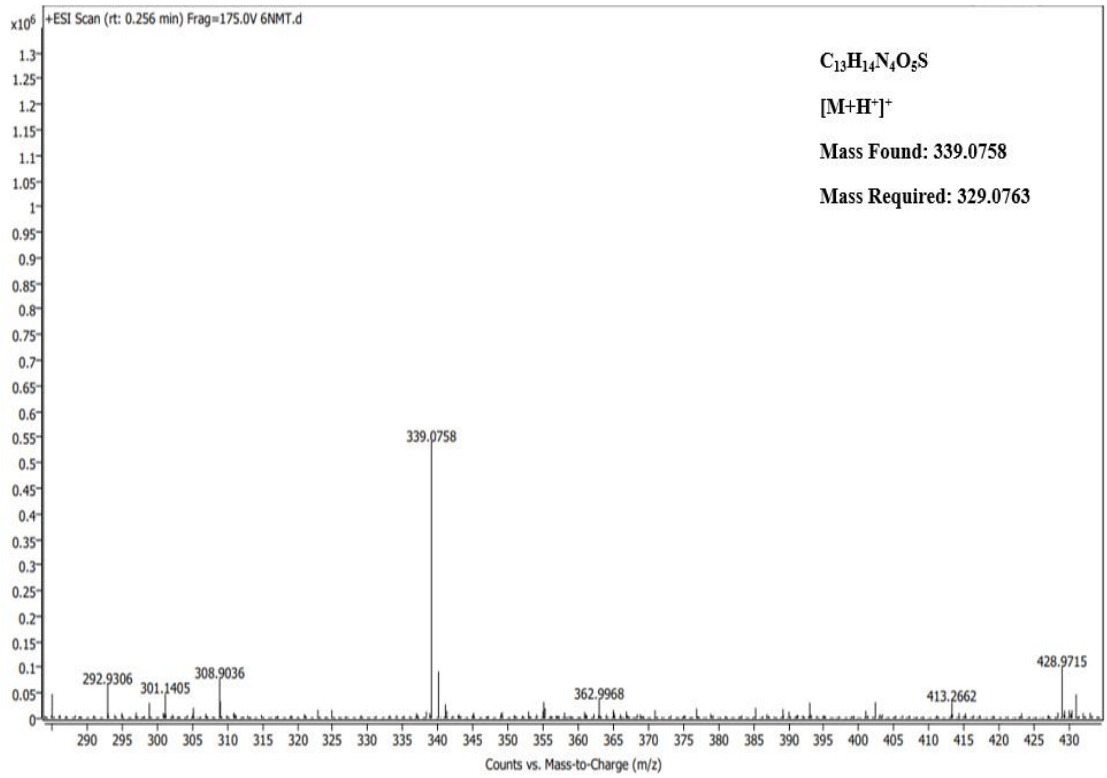

Figure S41. HRMS of **6NMT**

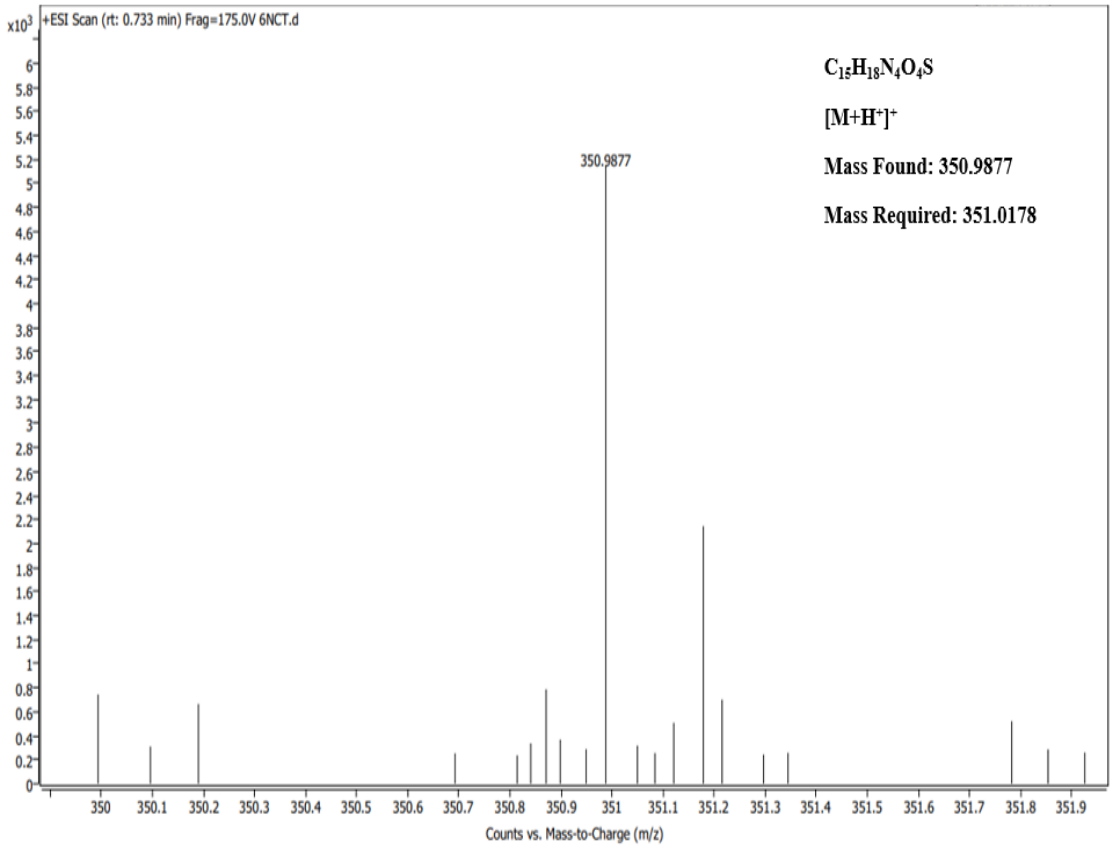

Figure S42. HRMS of **6NCT**

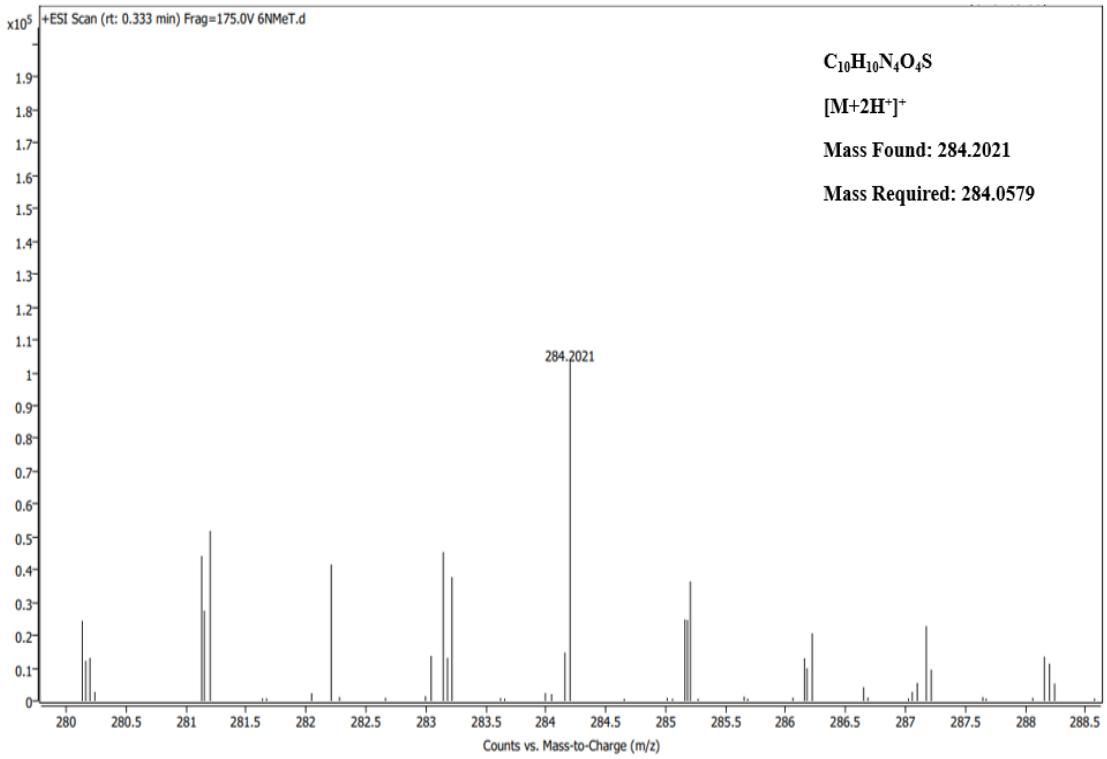

Figure S43. HRMS of **6NMeT**

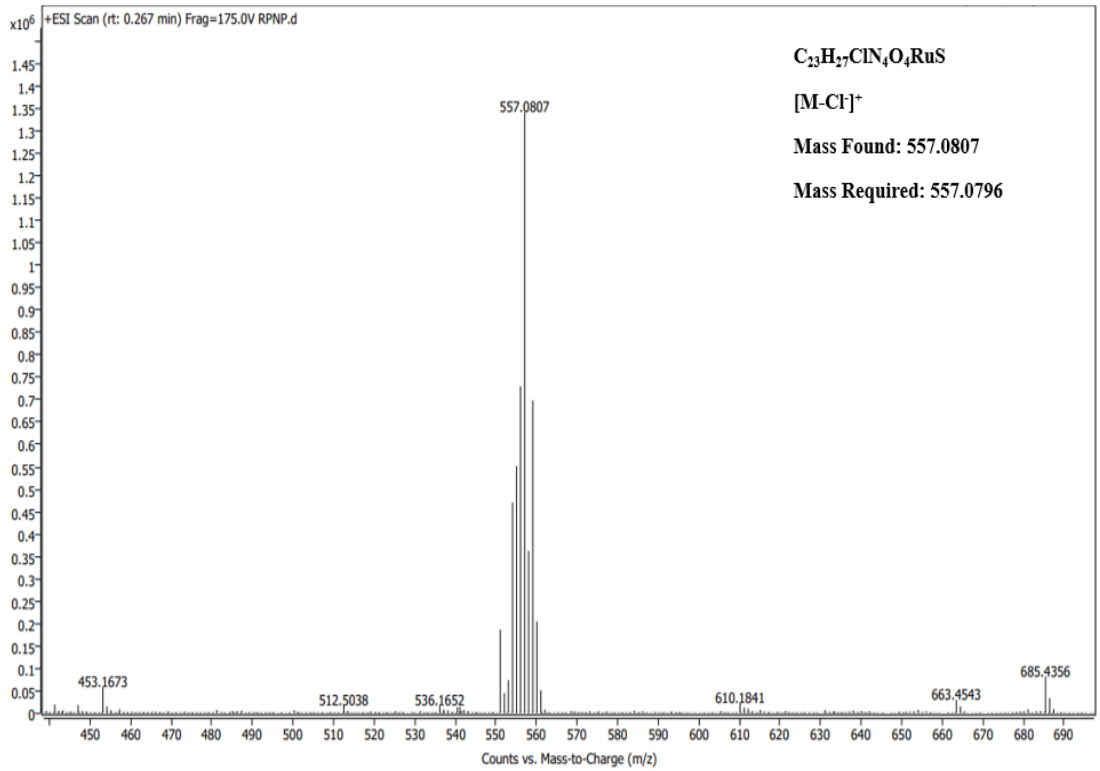

Figure S44. HRMS of **RuPNPT**

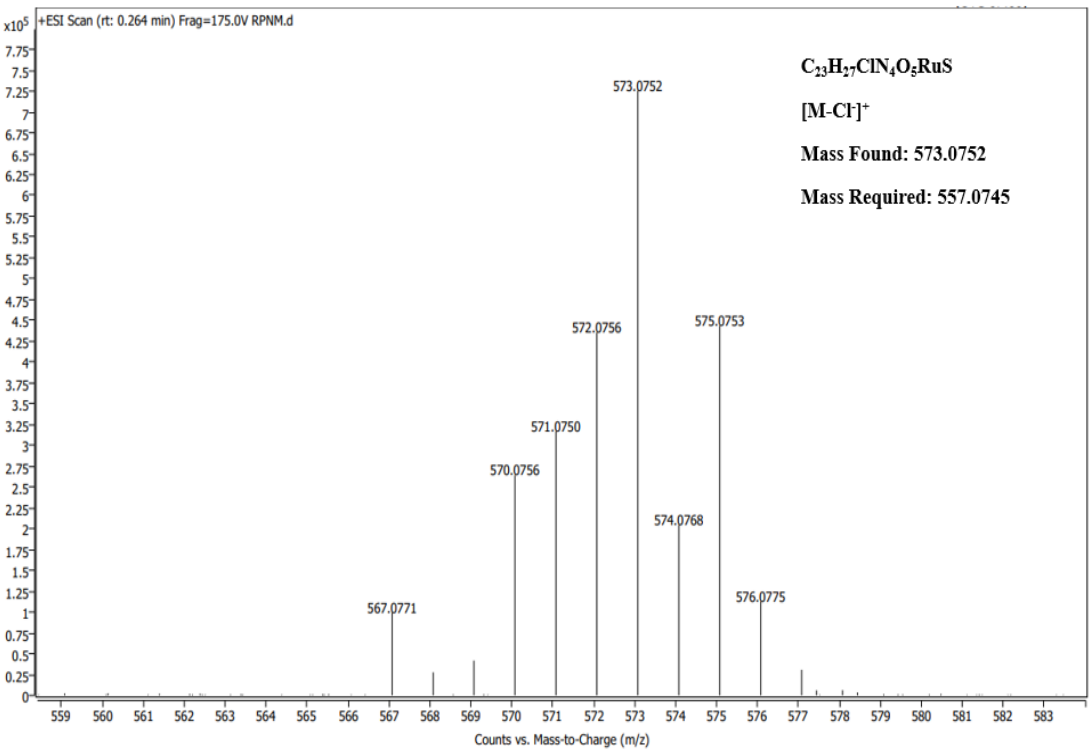

Figure S45. HRMS of **RuPNMT**

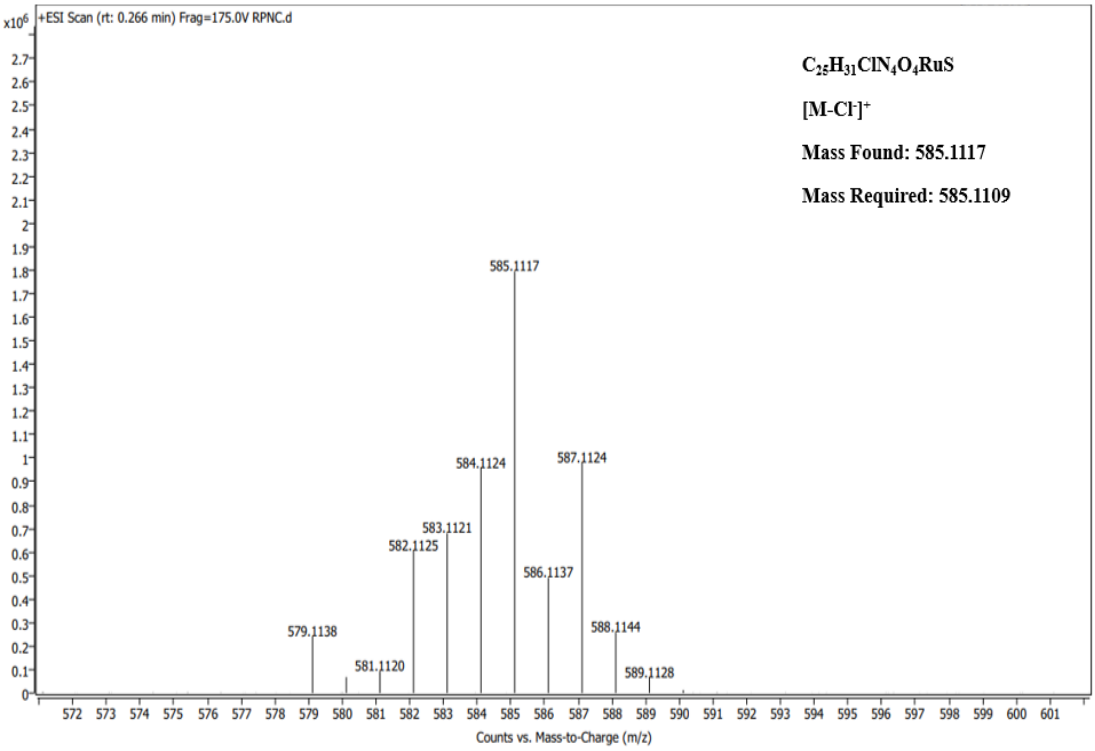

Figure S46. HRMS of **RuPNCT**

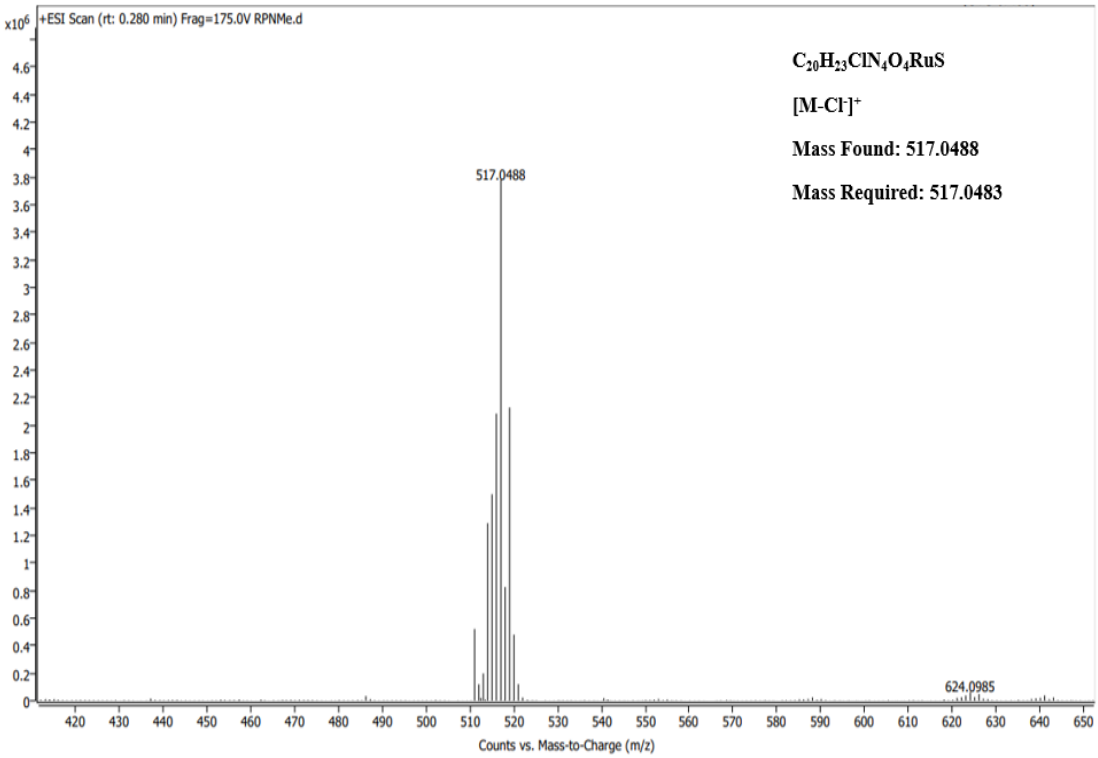

Figure S47. HRMS of **RuPNMeT**

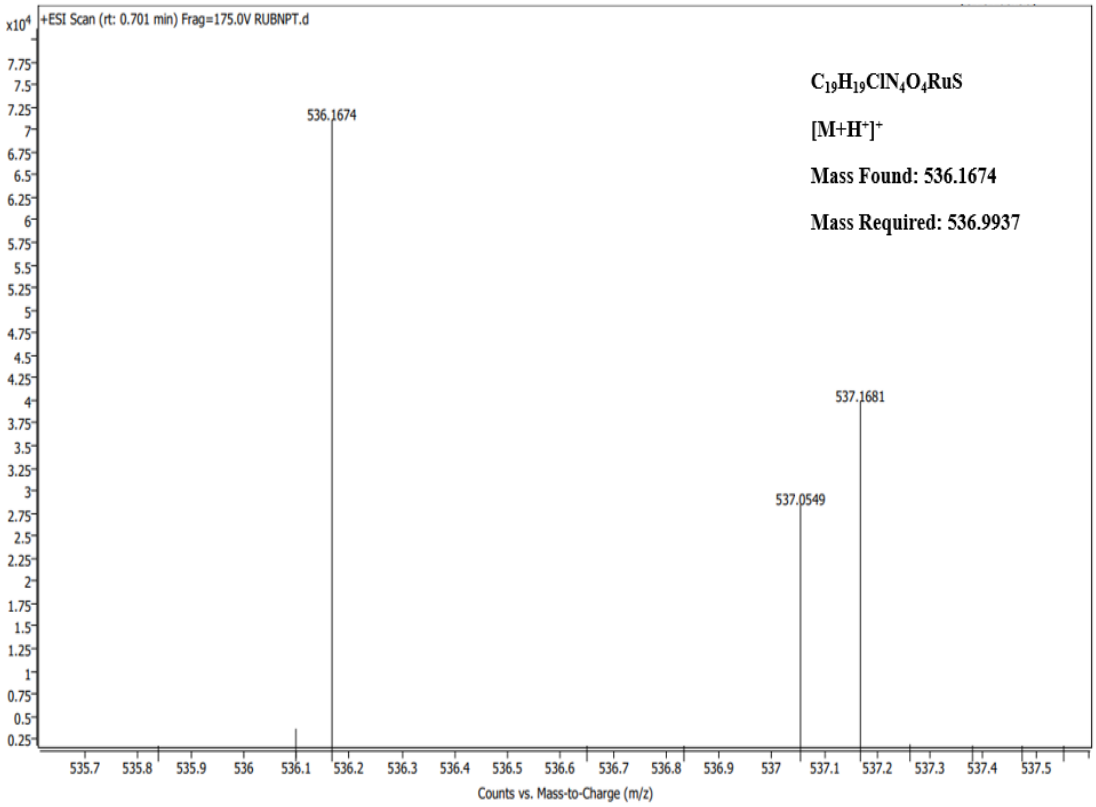

Figure S48. HRMS of **RuBNPT**

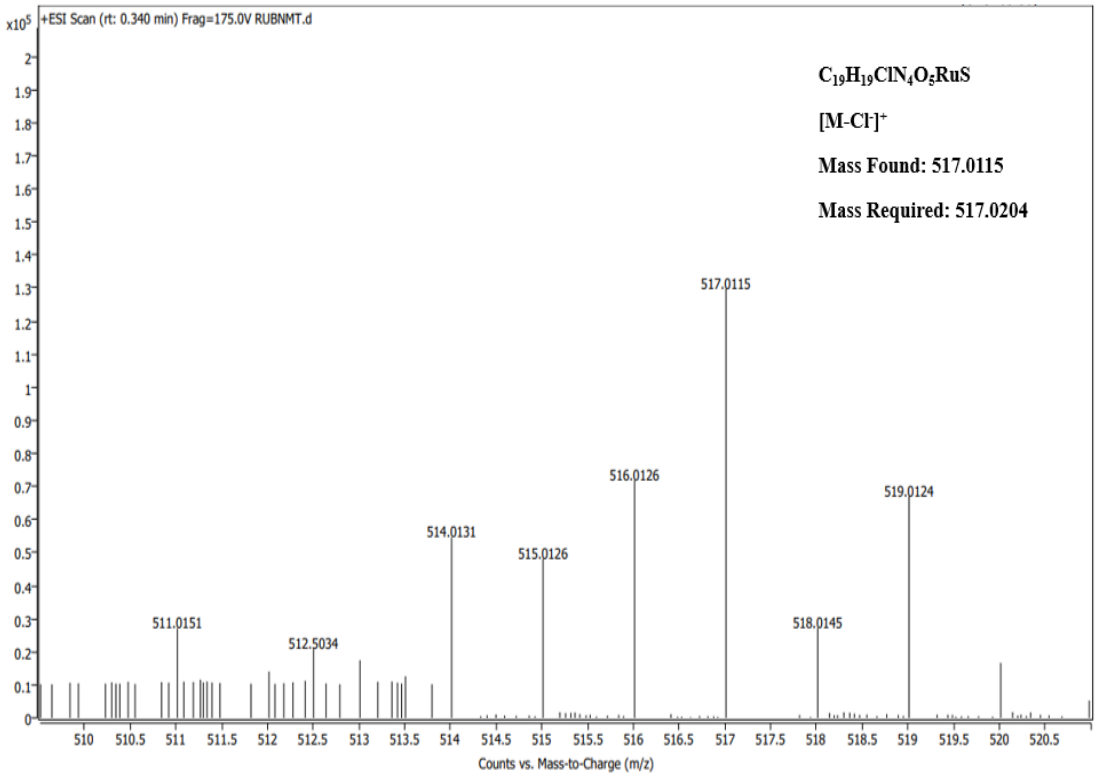

Figure S49. HRMS of **RuBNMT**

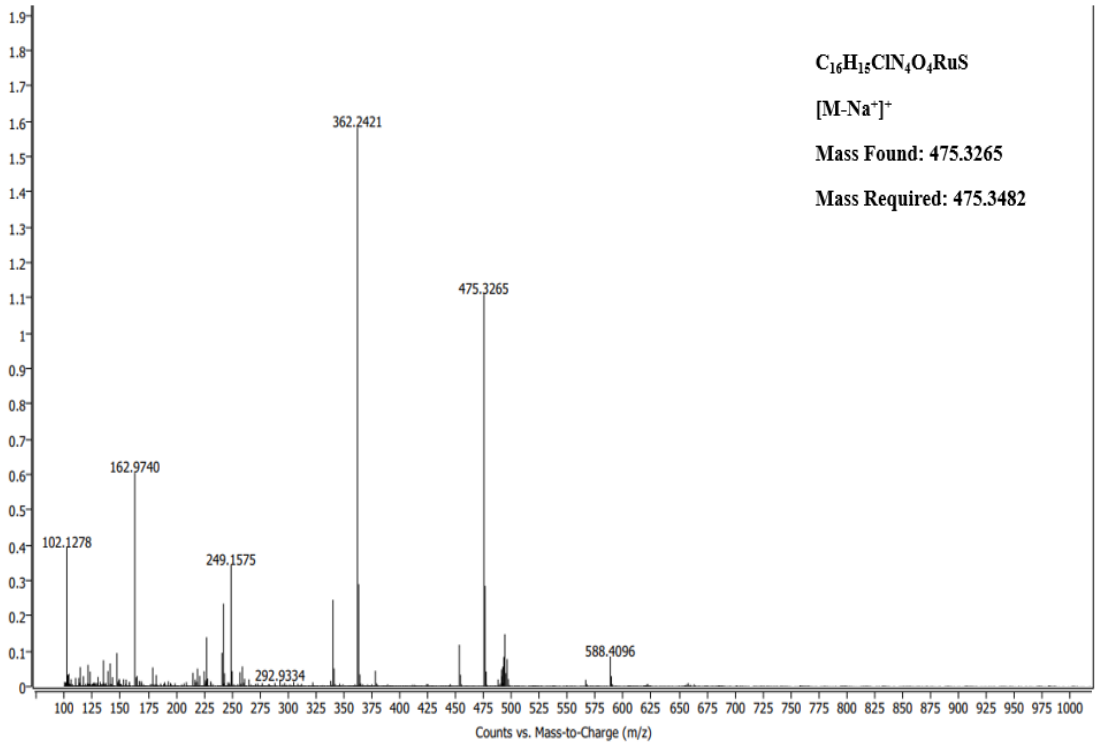

Figure S50. HRMS of **RuBNMeT**

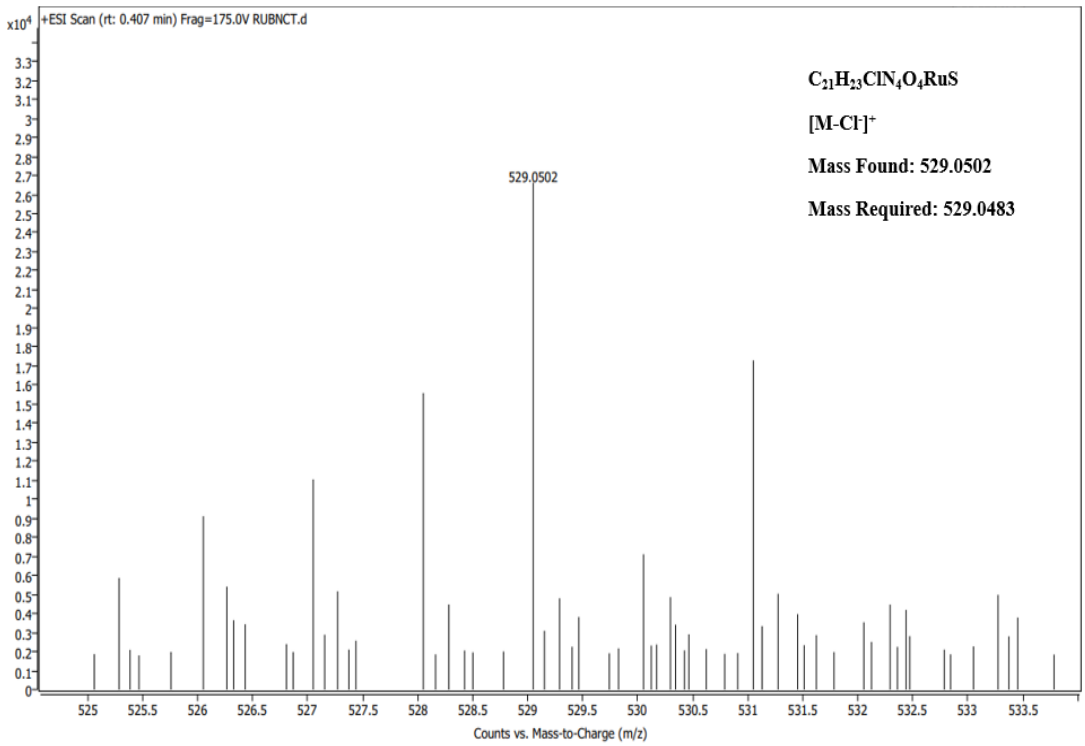

Figure S51. HRMS of **RuBNCT**

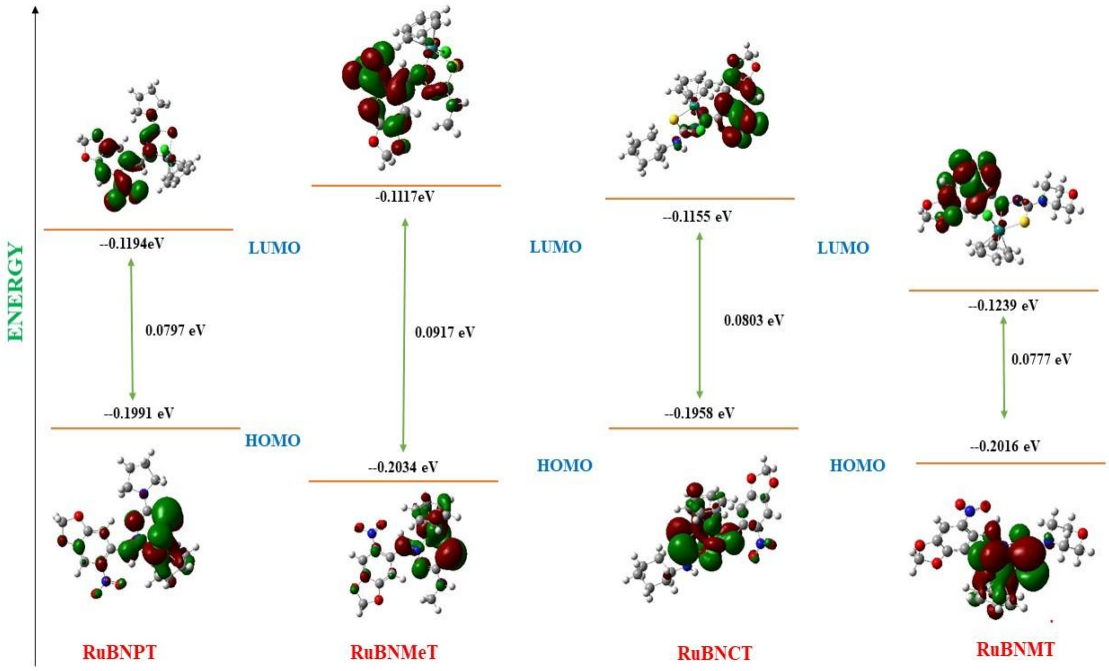

HOMO-LUMO energy gap for Ru(II)-benzene complexes.

Figure S52. The energy profile of all Ru-benzene complexes' frontier molecular orbitals.

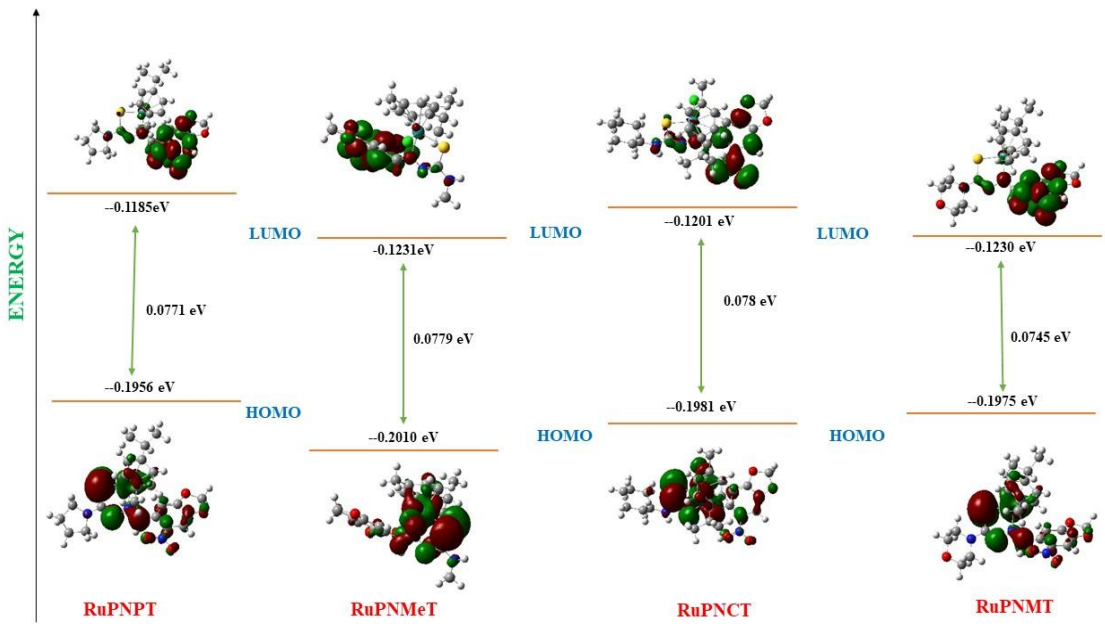

HOMO-LUMO energy gap for Ru(II)-*p*-cymene complexes

Figure S53. The energy profile of all Ru-p-cymene complexes' frontier molecular orbitals.

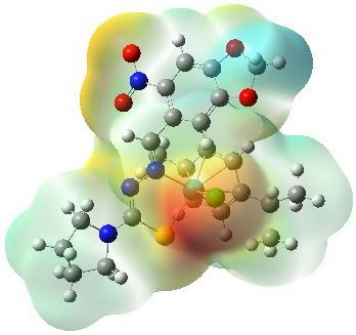

RuPNPT

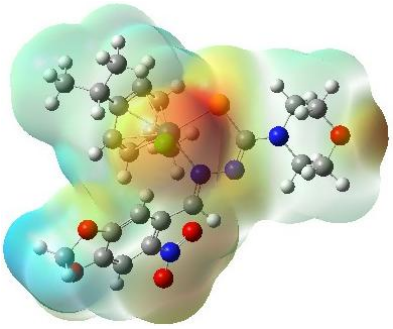

RuPNMT

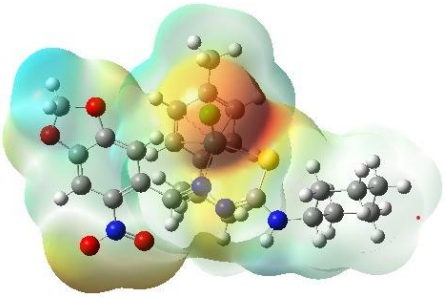

RuPNCT

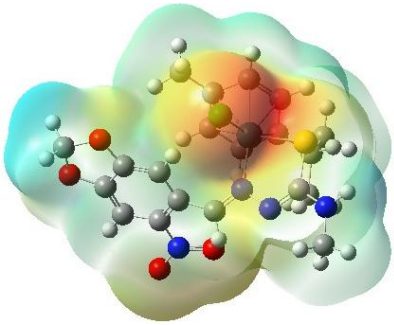

RuPNMeT

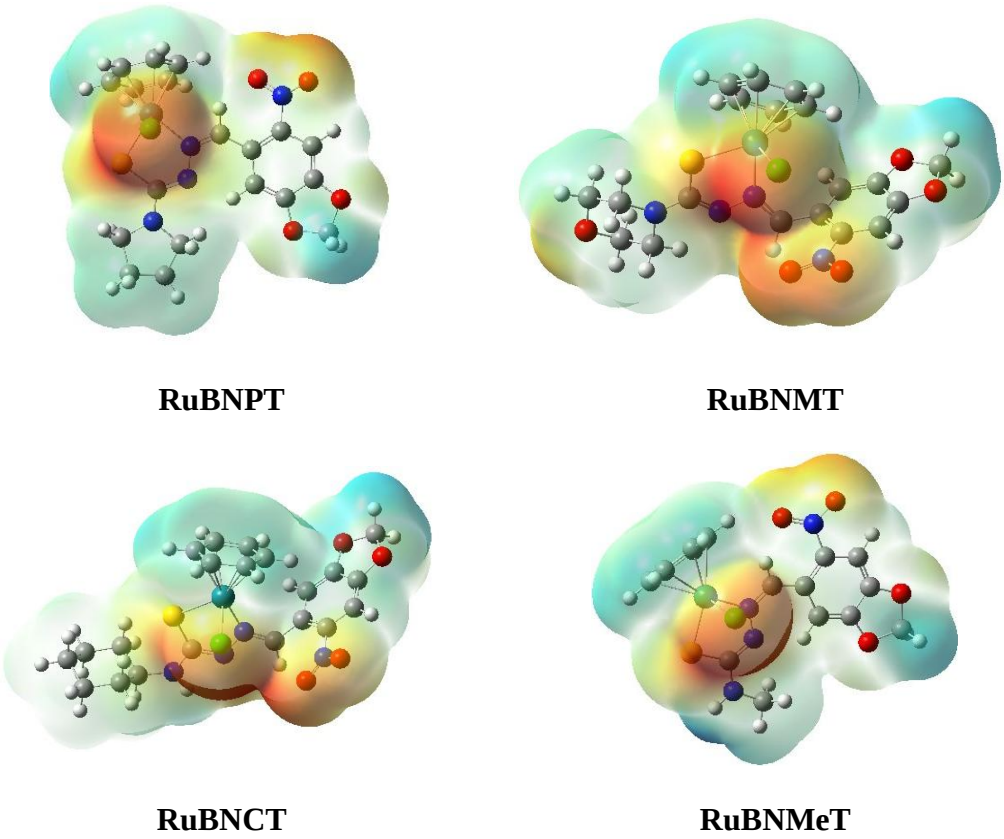

Figure S54. The MEP surface diagram of all the complexes.

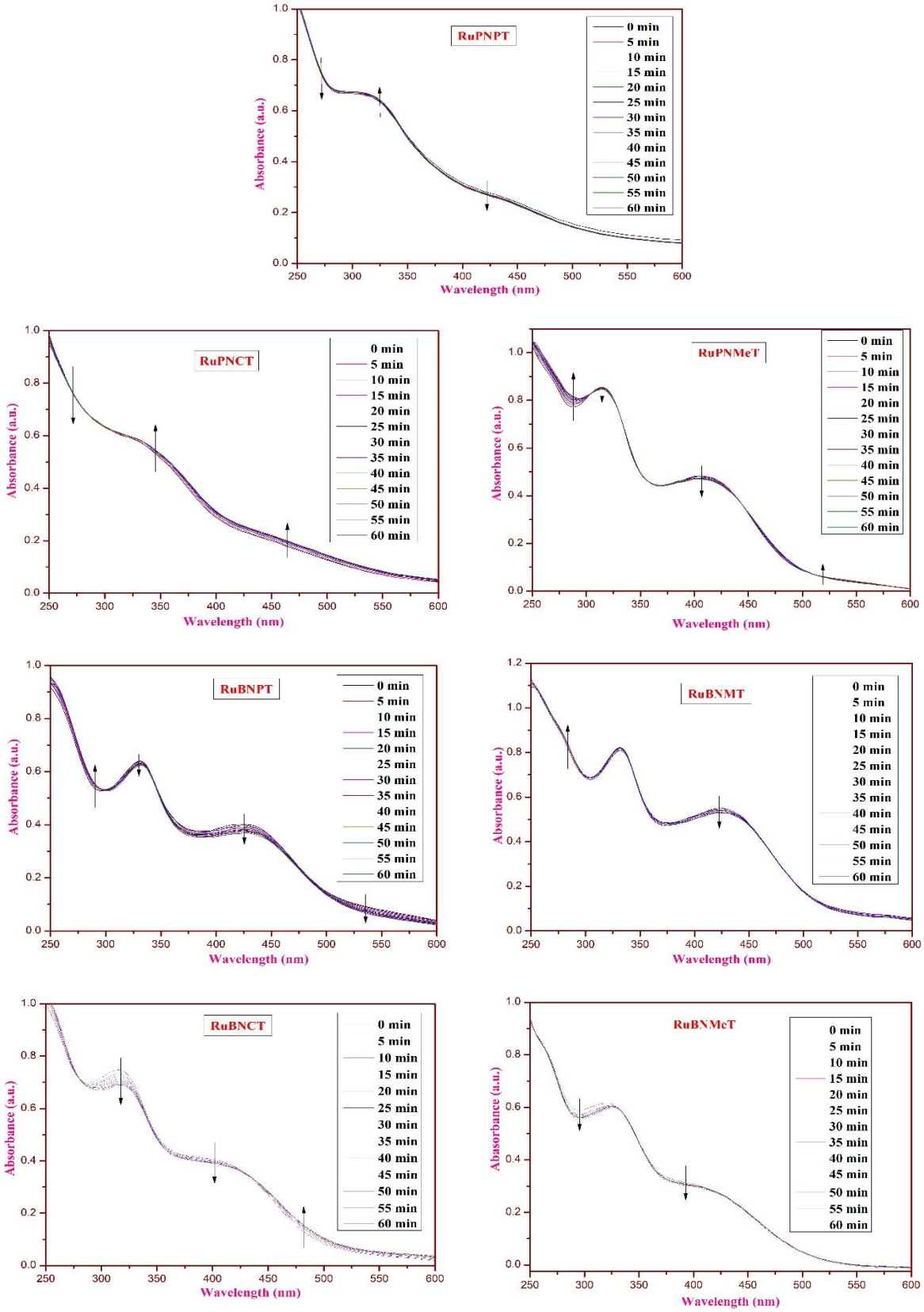

Figure S55. UV-visible spectra of all complexes (0.5 mM) in 4 mM sodium chloride solution

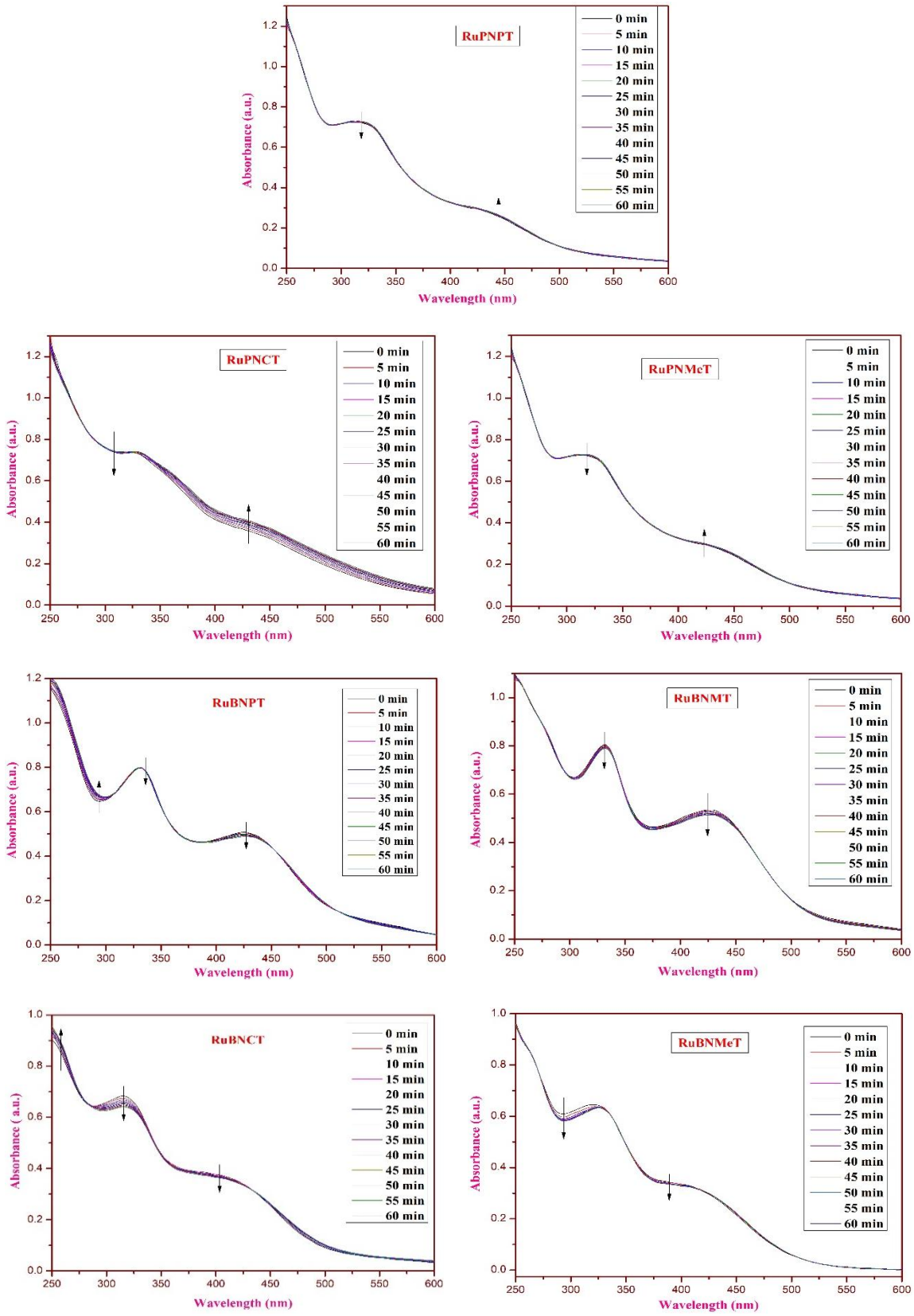

Figure S56. UV-visible spectra of all complexes (0.5 mM) in 110 mM sodium chloride solution

3D Interactions **Docked pose**

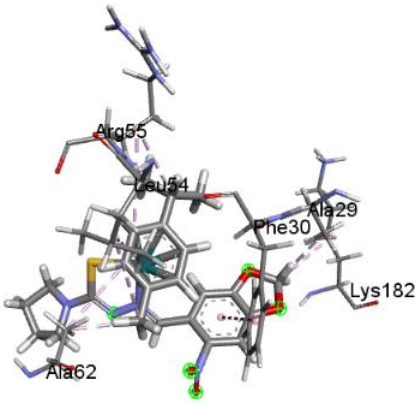

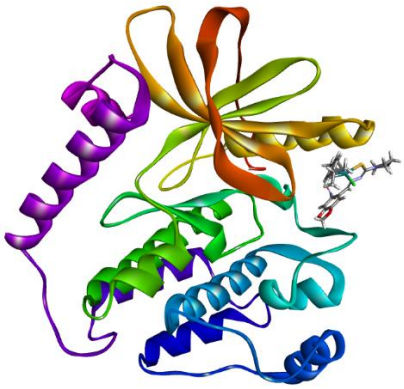

RuPNPT

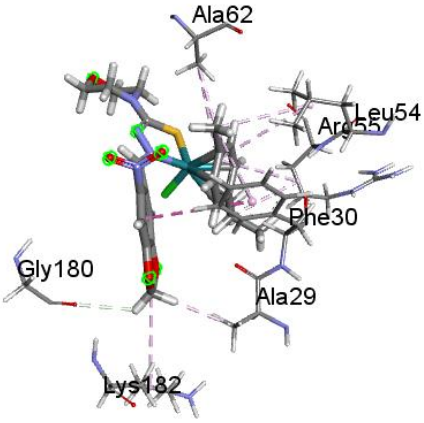

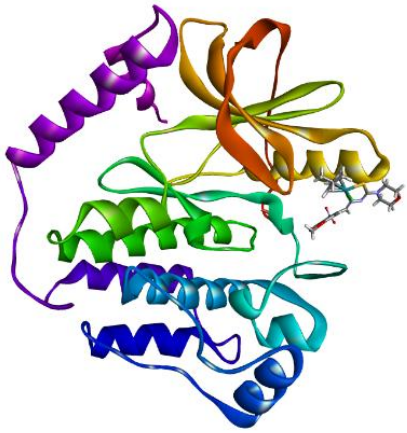

RuPNMT

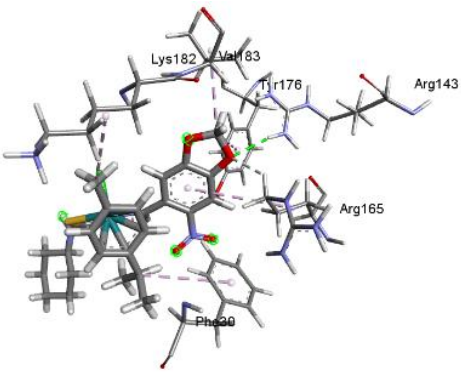

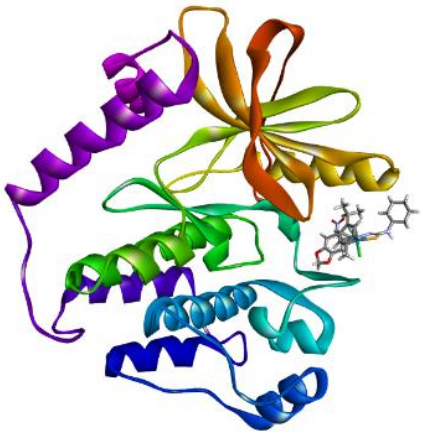

RuPNCT

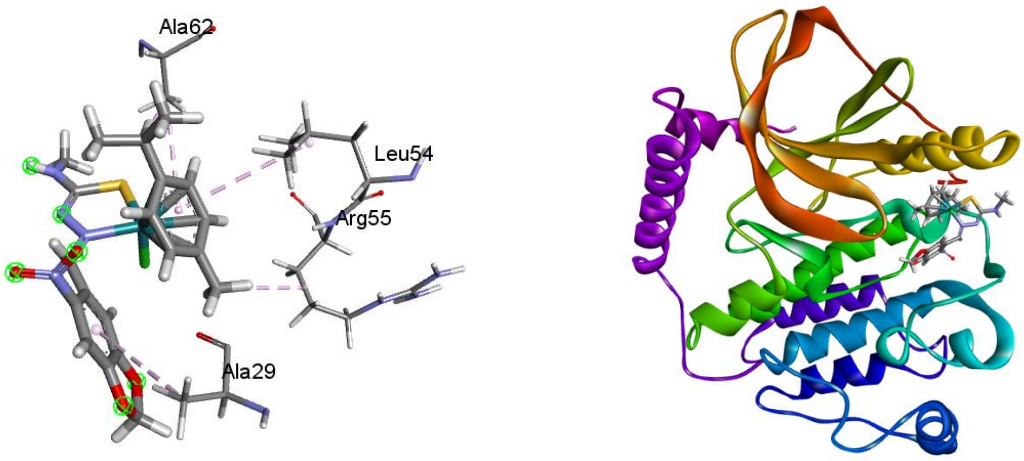

RuPNMeT

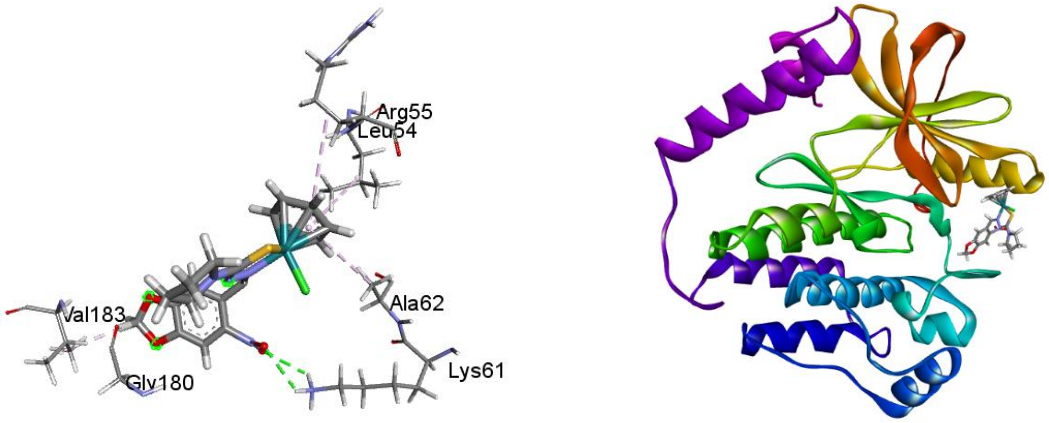

RuBNPT

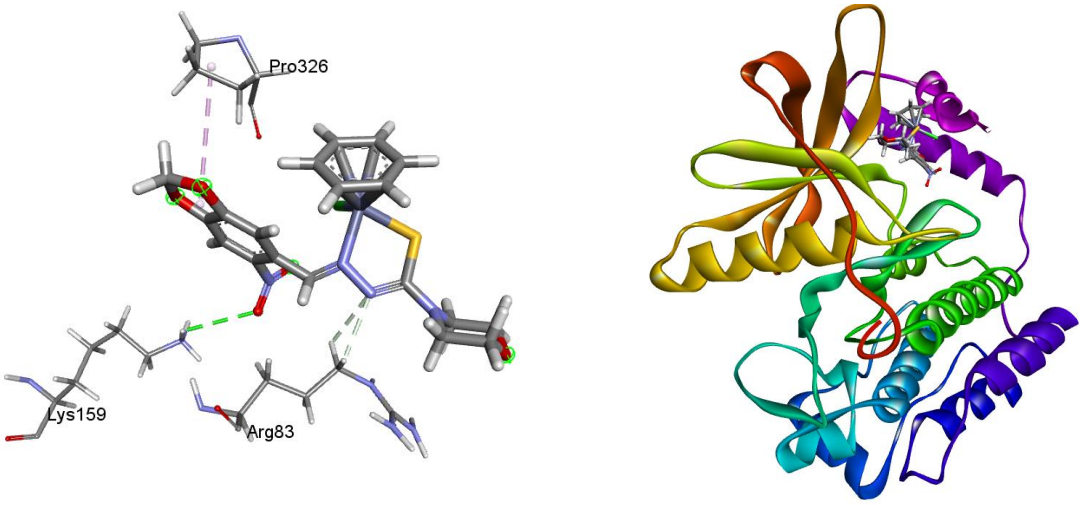

RuBNMT

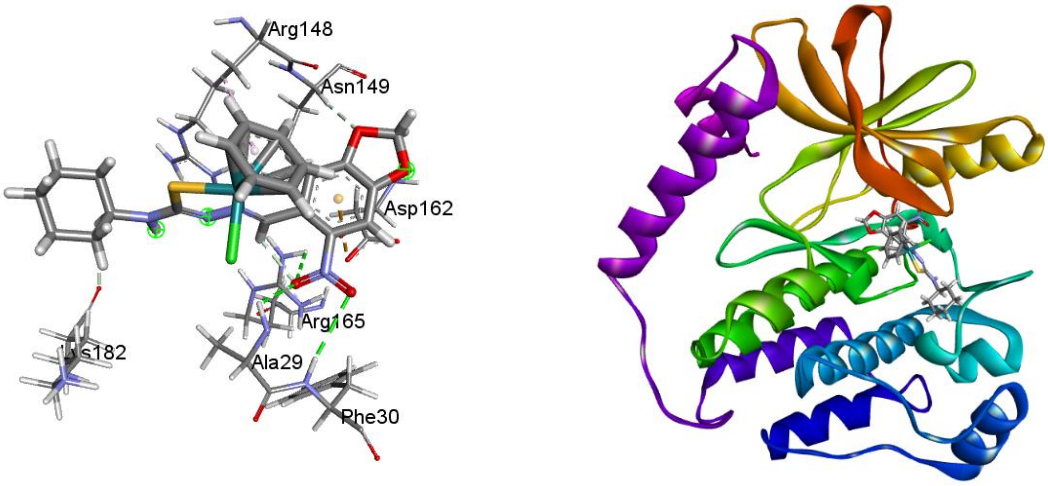

RuBNCT

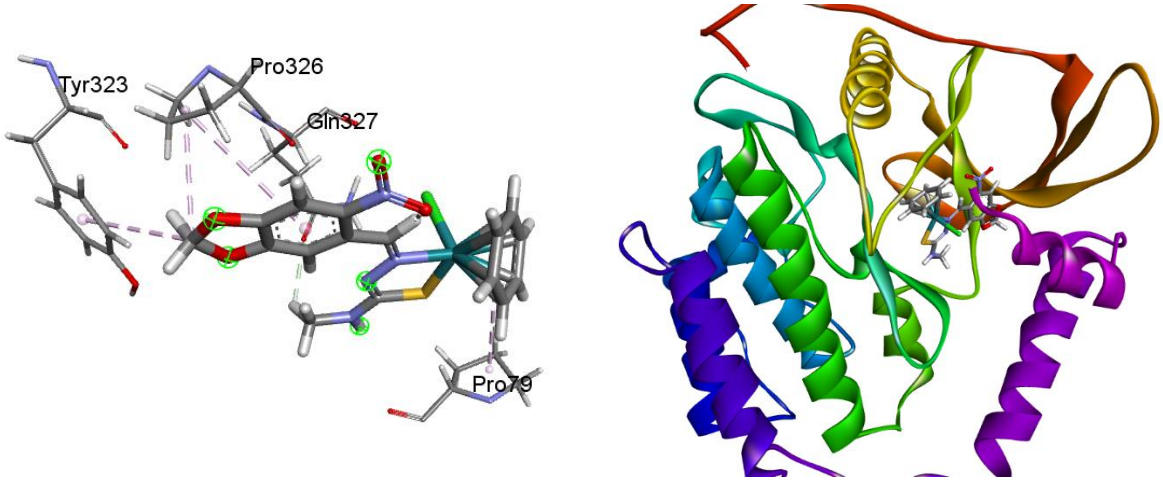

RuBNMeT

Figure S57. 3D interactions and Docked pose of all complexes (**RuPNPT**-**RuBNMeT**) with EGFR protein.

Absorption spectra **[DNA]/(εa- εf) × 10^{-9} versus [DNA] plot**

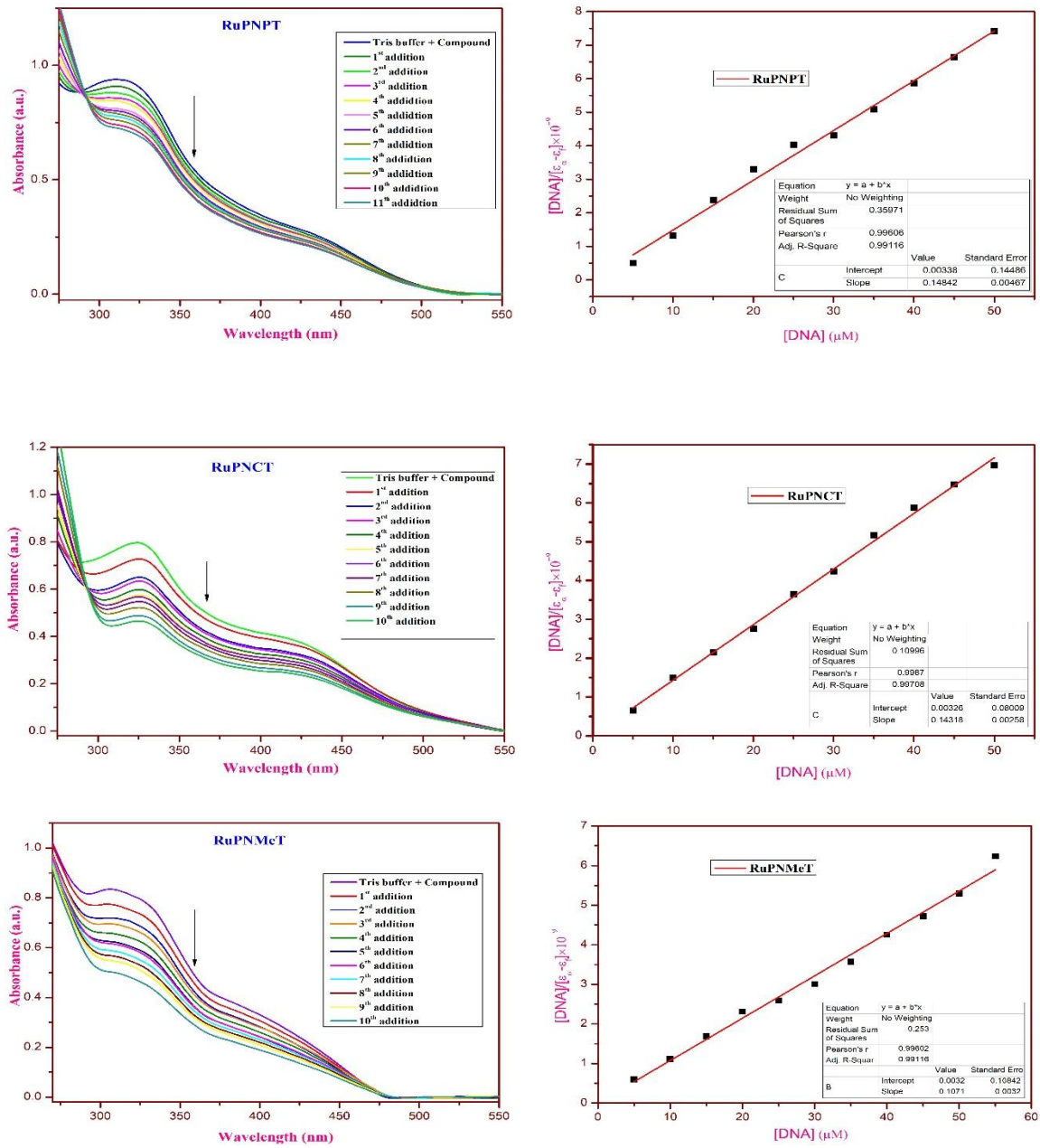

Figure S58. Absorption spectra of all other Ru(η^6-p-cymene) complexes (left) and [DNA]/(εa-εf) × 10^{-9} versus [DNA] plot (right)

Absorption spectra **[DNA]/(εa- εf) × 10-9 versus [DNA] plot**

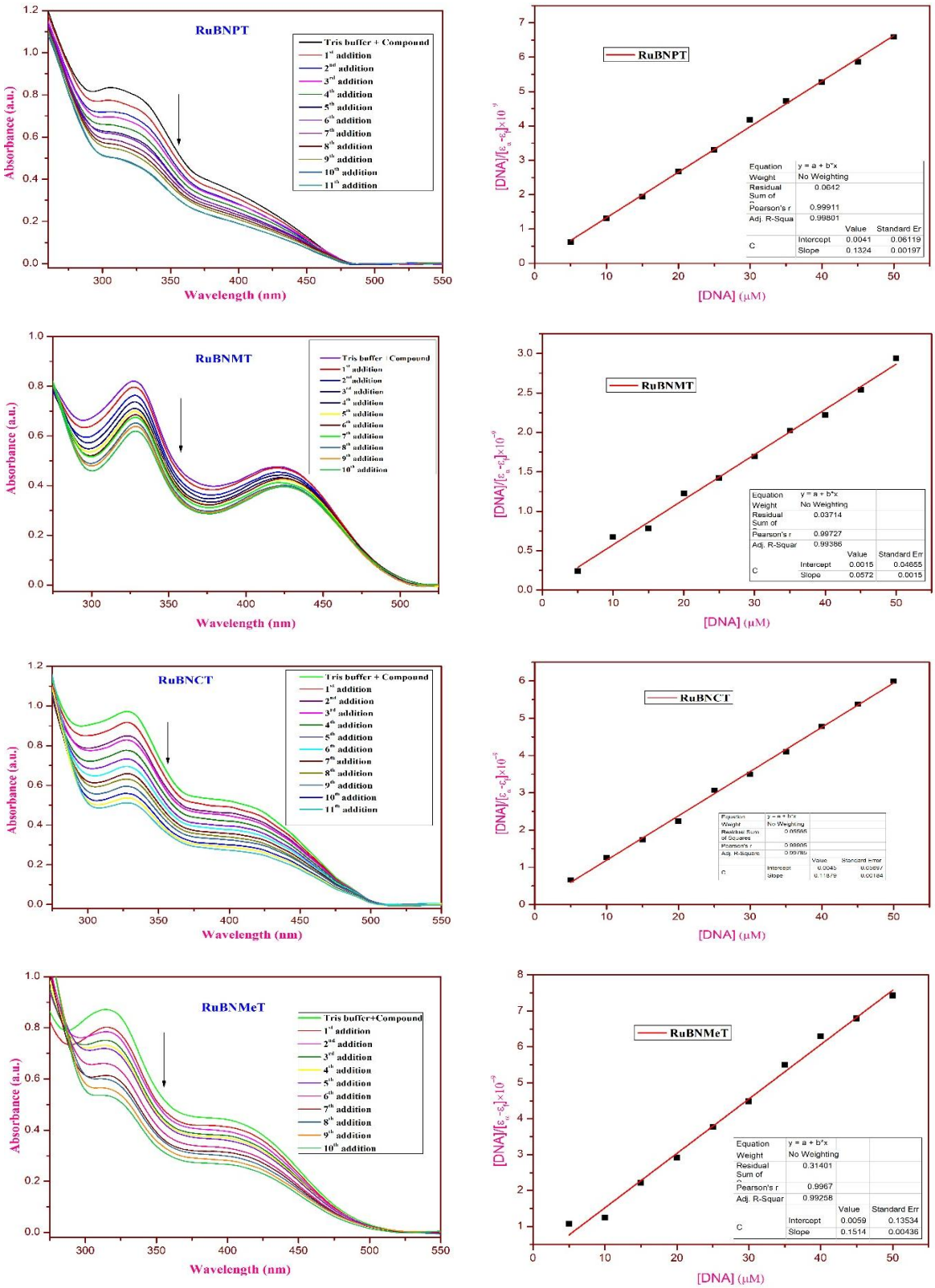

Figure S59. Absorption spectra of all Ru(η6-benzene) complexes (left) and [DNA]/(εa-εf) × 10-9 versus [DNA] plot (right)

Emission spectra **Stern-Volmer plot**

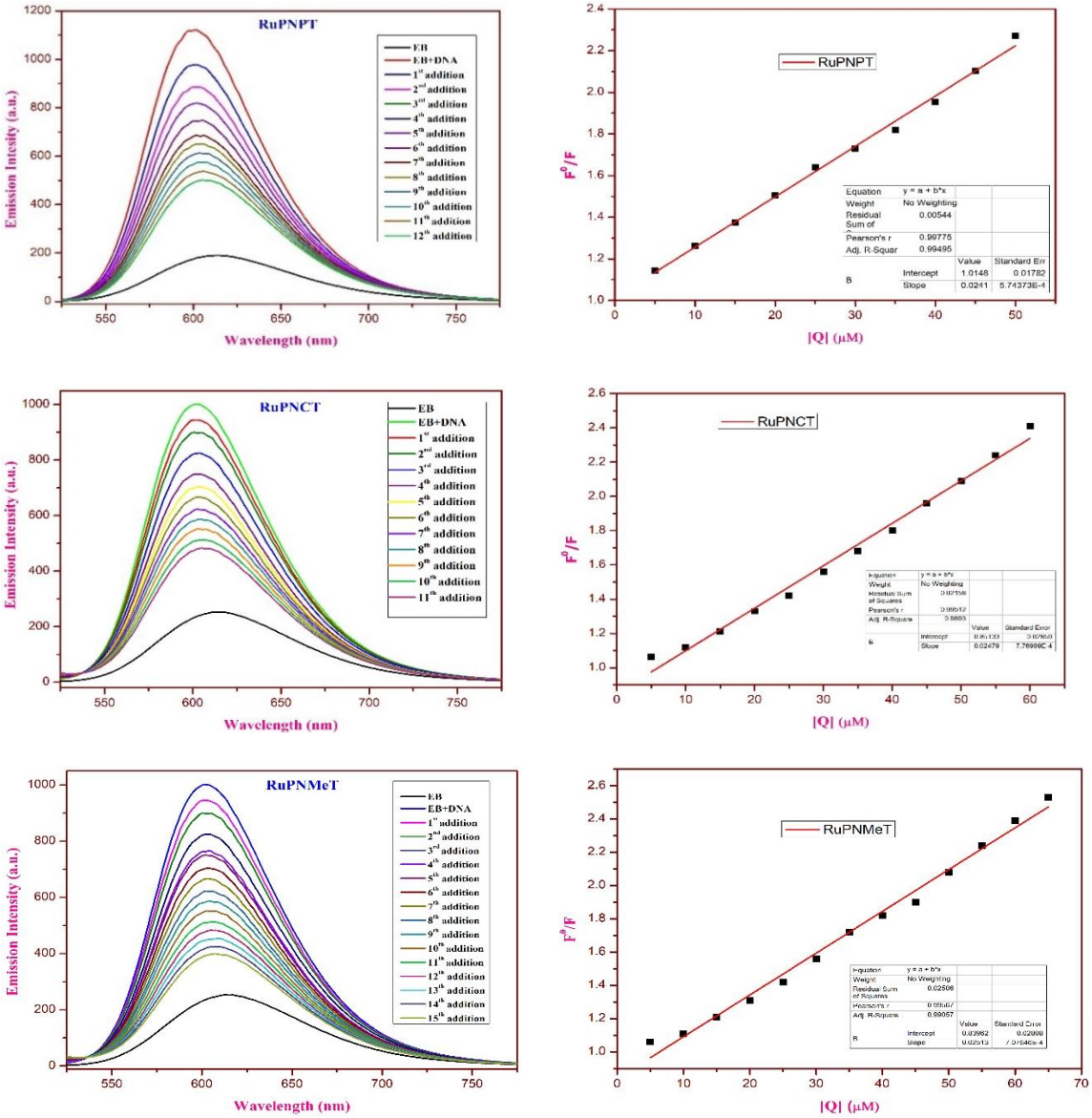

Figure S60. Quenching curves of all Ru(η^6-p-cymene) complexes (left) as well as a Stern–Volmer diagram (right)

Emission spectra **Stern-Volmer plot**

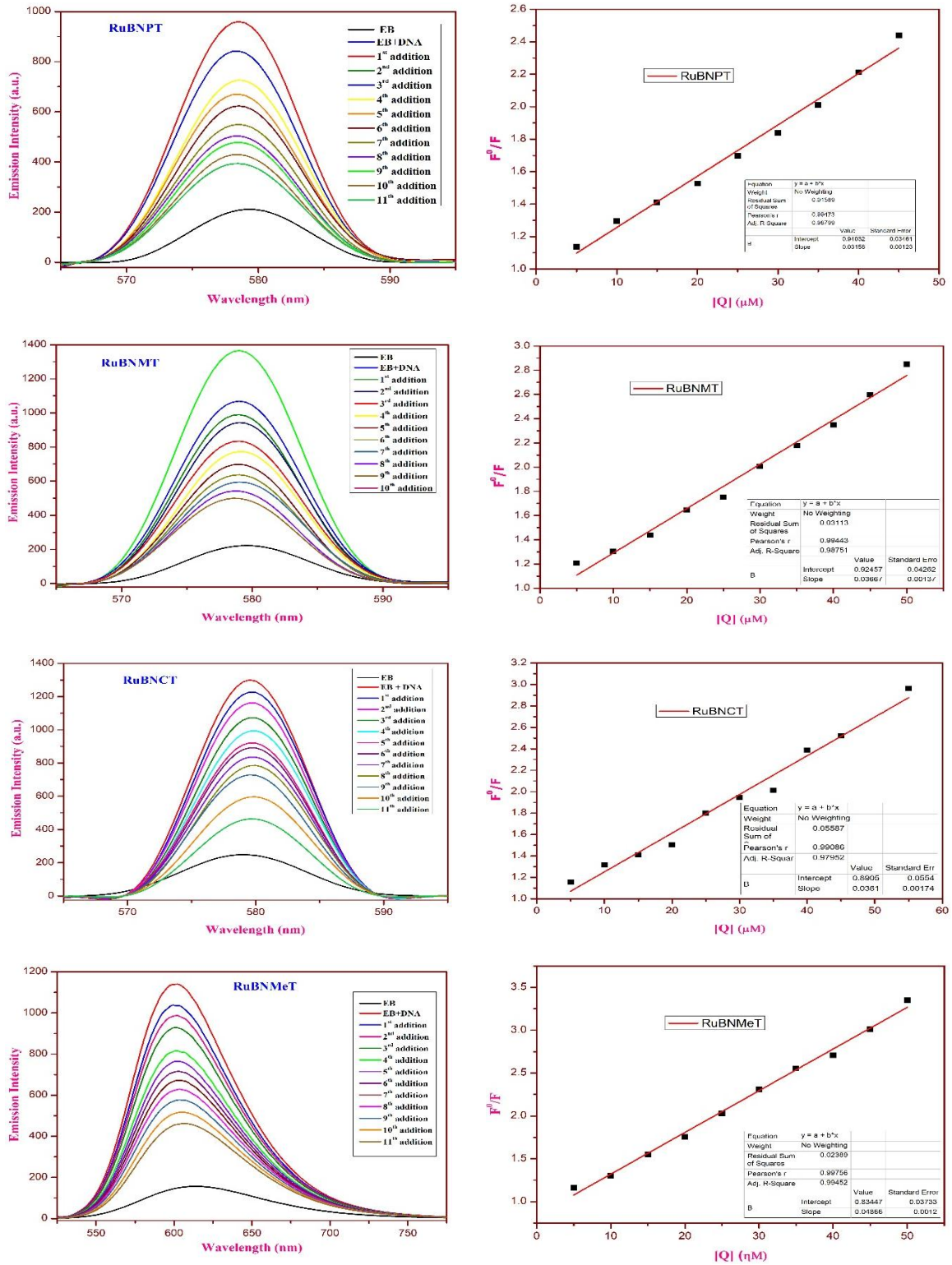

Figure S61. Quenching curves of other Ru(η^6-benzene) complexes (left) as well as a Stern–Volmer diagram (right)

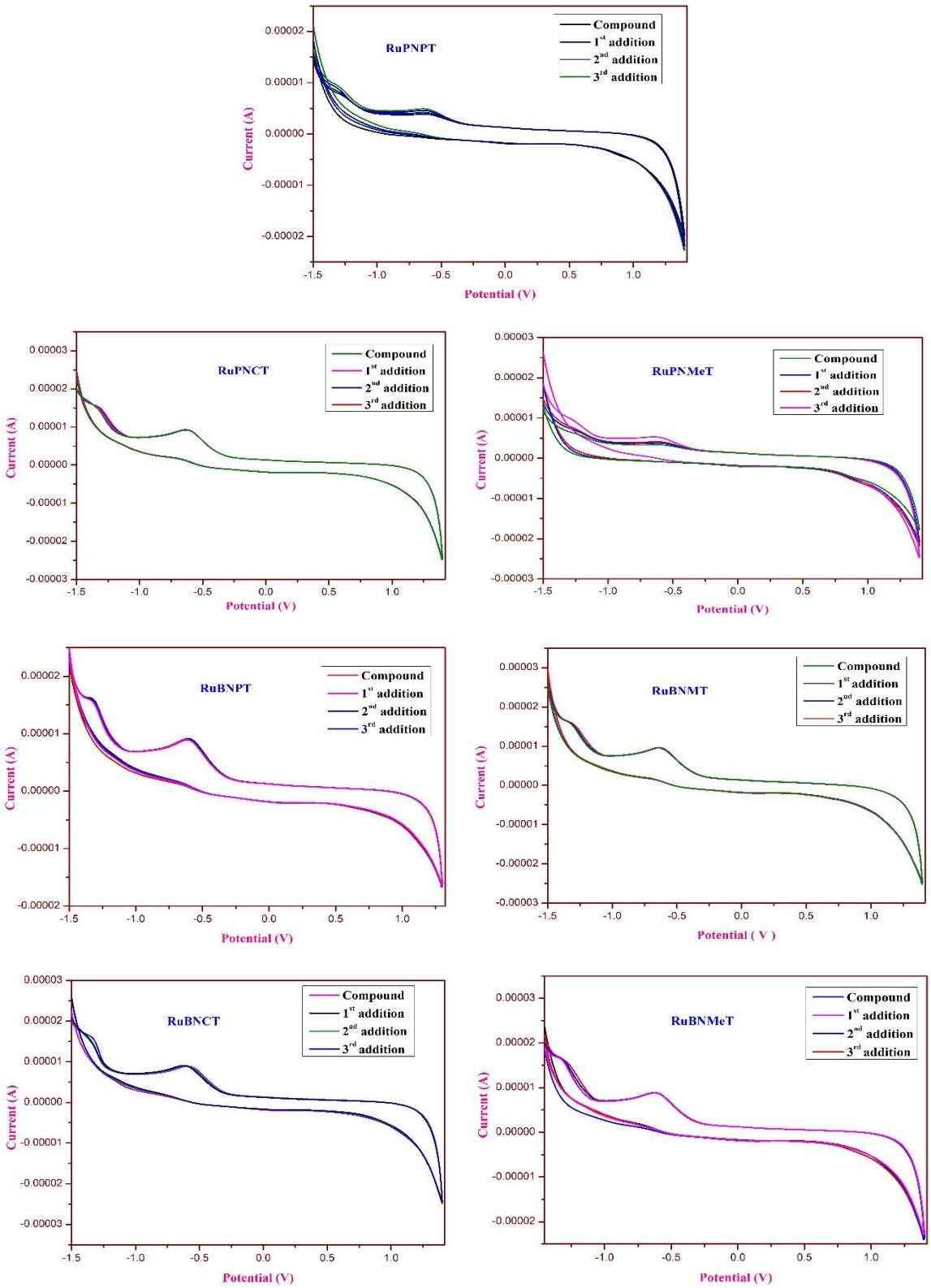

Figure S62. Cyclic voltammograms of all the complexes(25 µM) in the absence and presence of DNA (5 µM) (3 additions).

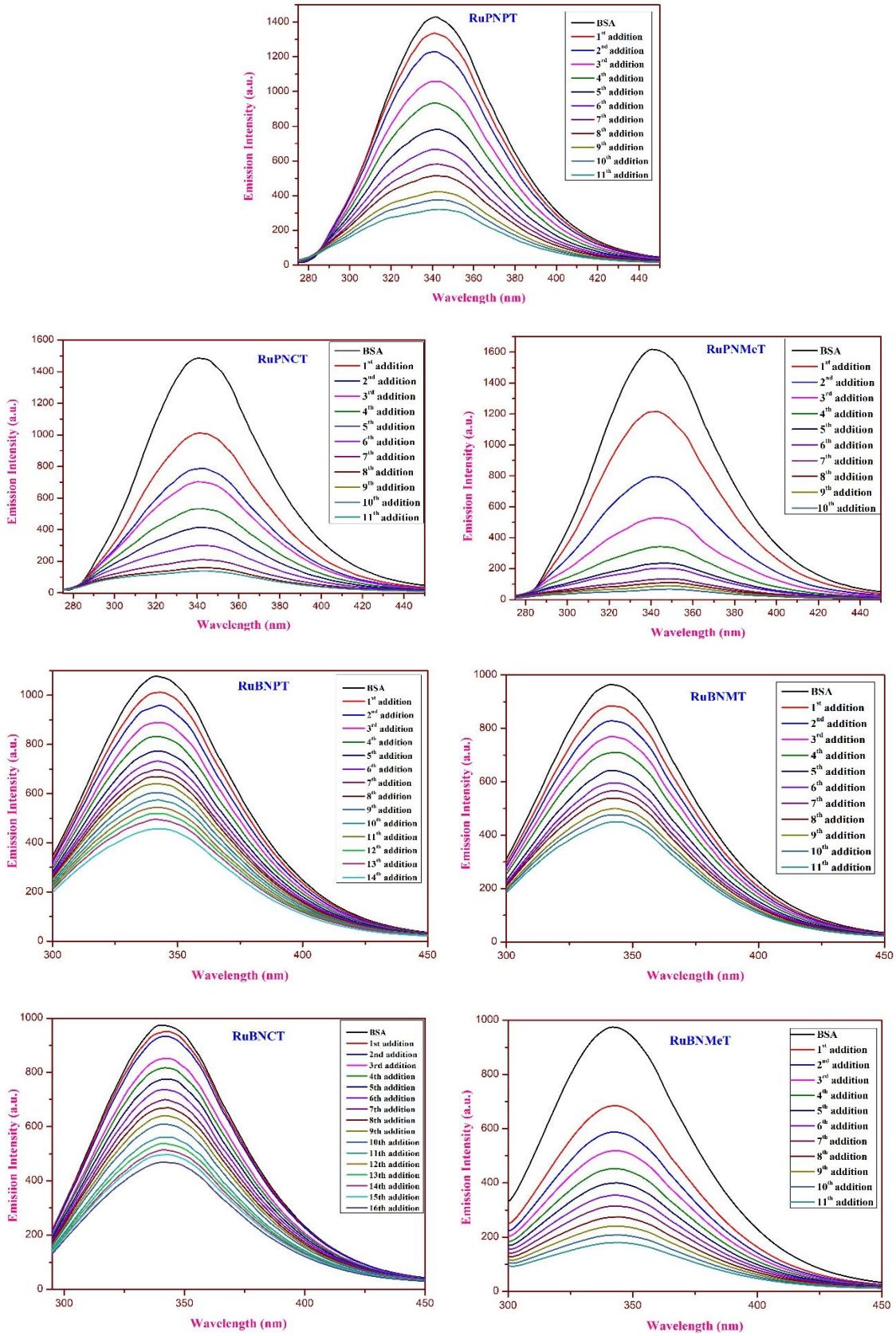

Figure S63. Bovine serum albumin (BSA; 1 μM) emission quenching graphs with increasing additions of the complexes (0– 50 μM)

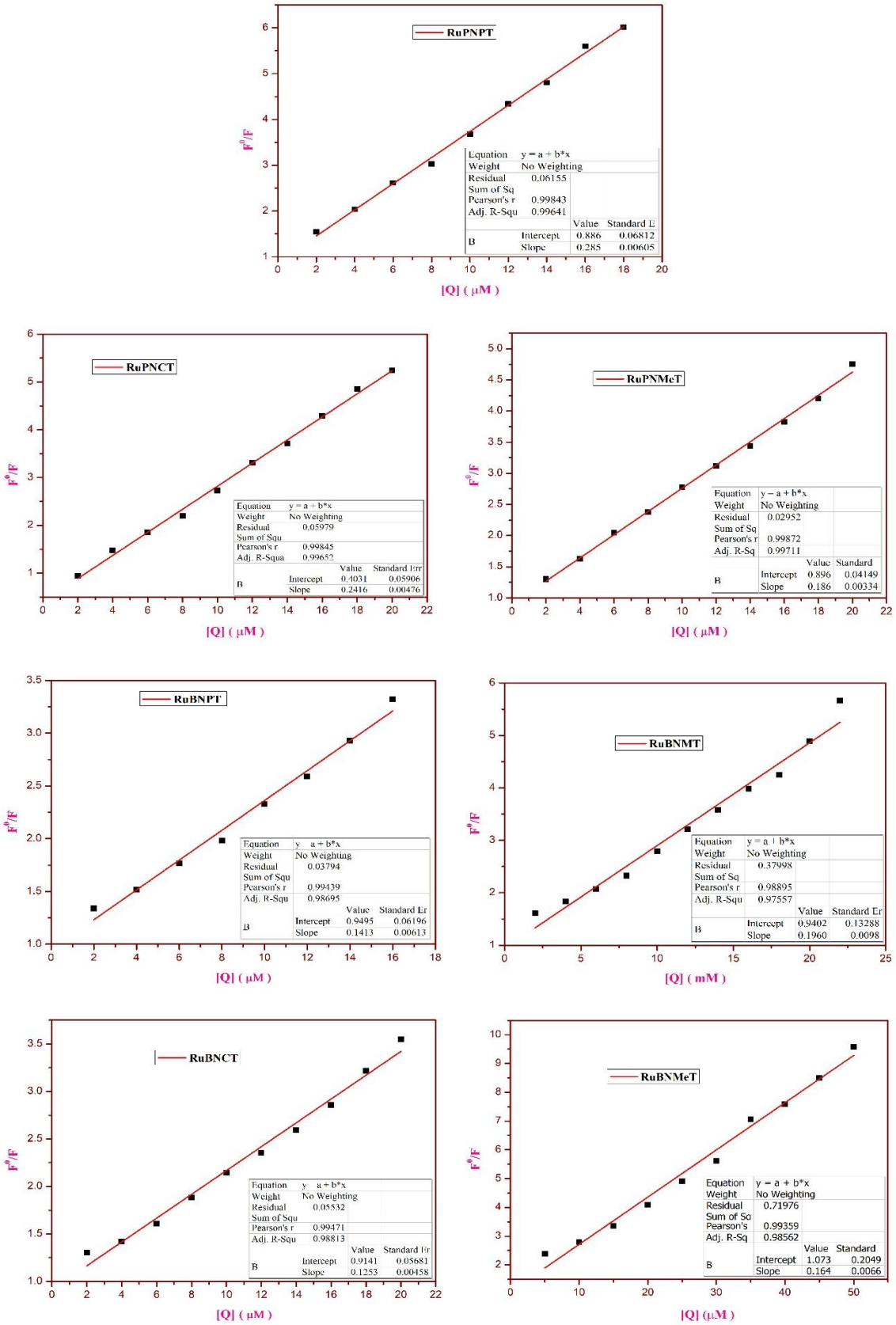

Figure S64. Stern- Volmer plots of all complexes

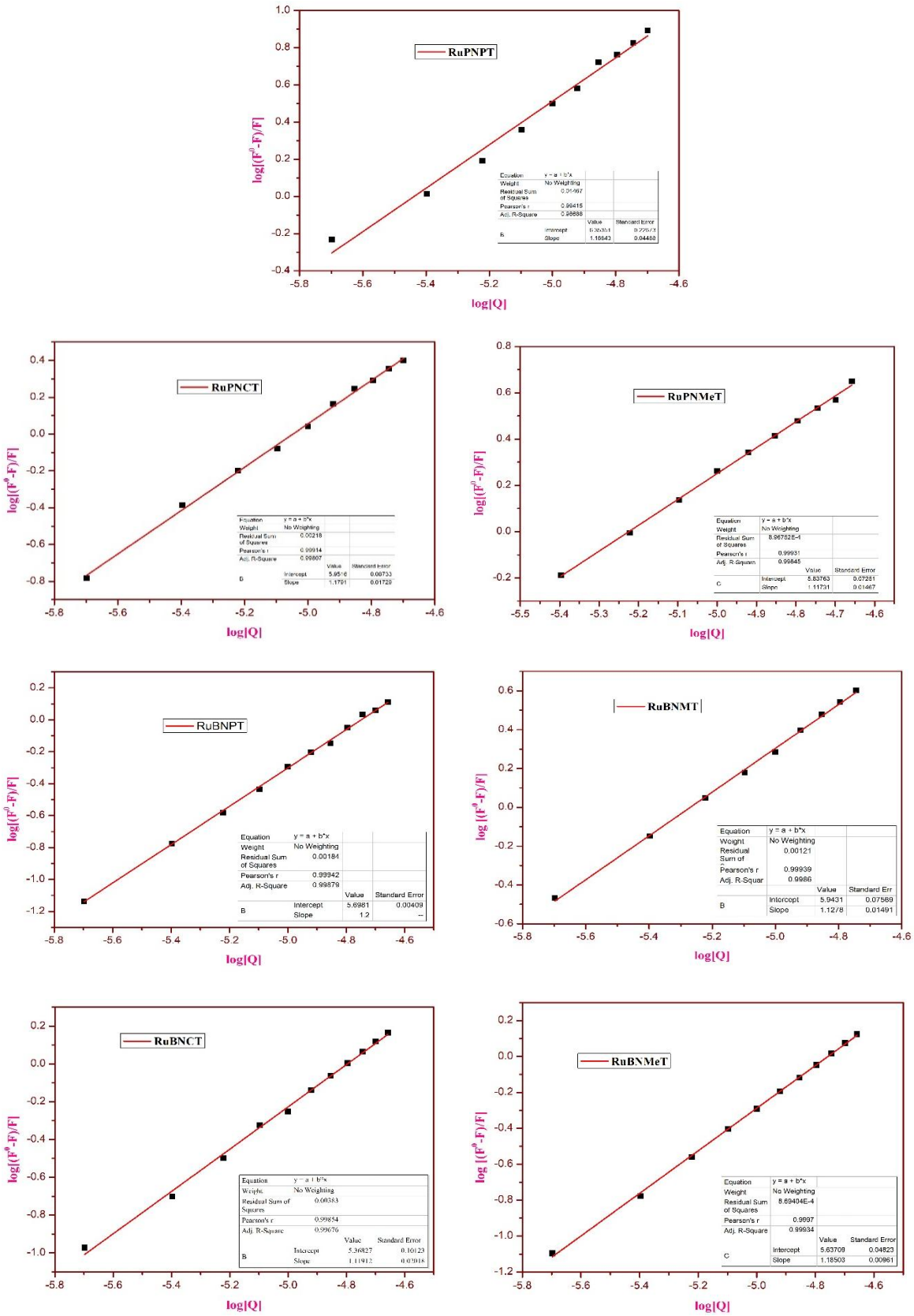

Figure S65. Scatchard plots of all complexes

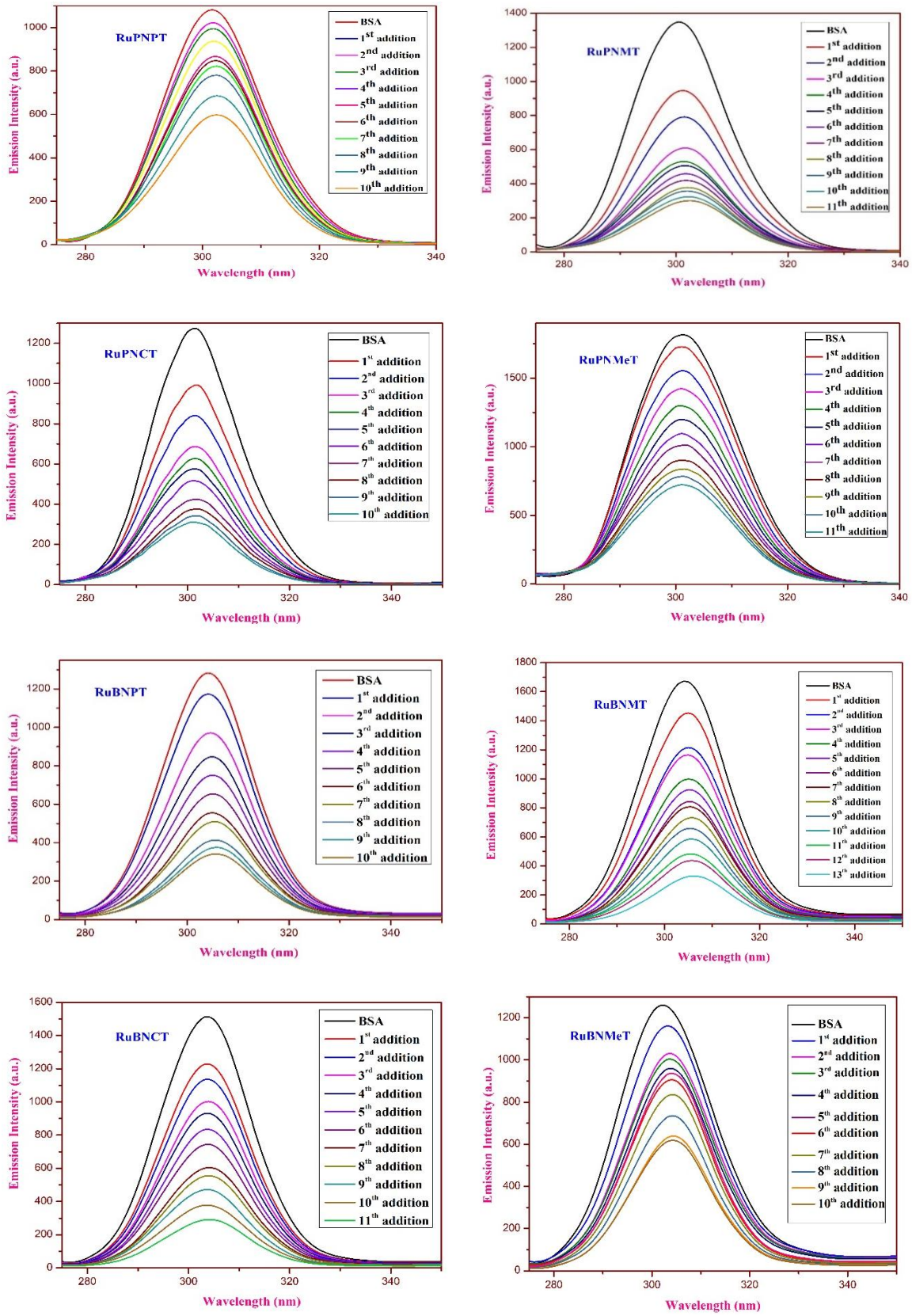

Figure S66. Synchronous spectra of BSA (1 μM) as a function of the concentration of all complexes with Δλ= 15 nm

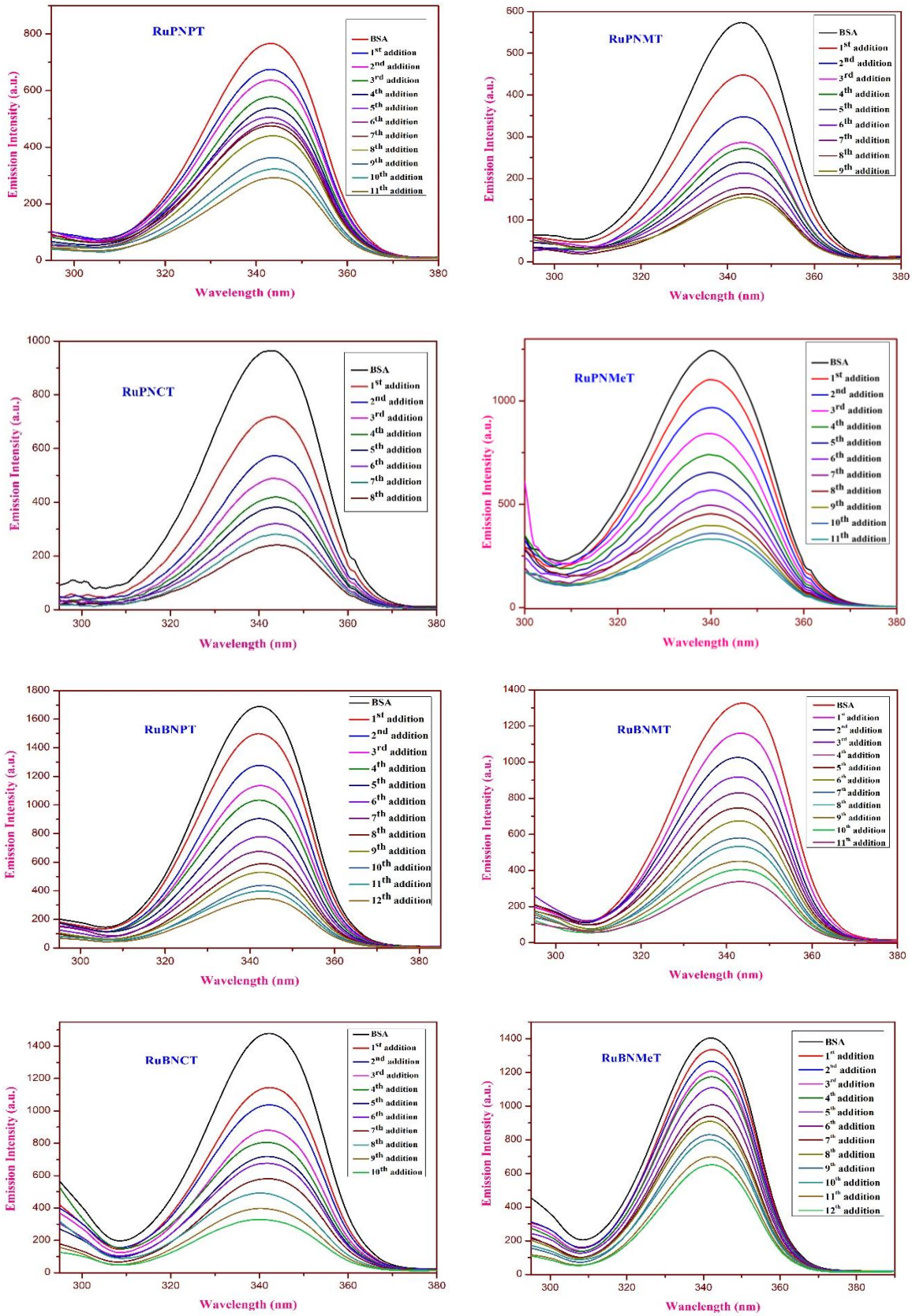

Figure S67. Synchronous spectra of BSA (1 μM) as a function of the concentration of all complexes with Δλ= 60 nm

Table S1 Crystallographic parameters of **6NPT** and **RuPNMT**.

Identification code	**6NPT**	**RuPNMT**
Empirical formula	$C_{13}H_{12}N_4O_4S$	$C_{23}H_{27}ClN_4O_5RuS$
CCDC number	2422094	2422095
Formula weight	320.33	608.06
Temperature	296 (2) K	296 (2) K
Wavelength	0.71073 Å	0.71073 Å
Crystal system	Monoclinic	Monoclinic
Space group	*P21/c*	*P21/c*
Unit cell dimensions		
a (Å)	6.2700(4)	13.8239(8)
b (Å)	16.0102(11)	14.3869(8)
c (Å)	14.1883(9)	14.0803(7)
α (°)	90	90
β (°)	92.133(3)	117.586(2)
γ(°)	90	90
Volume	1423.29(16) $Å^3$	2482.0(2) $Å^3$
Z	4	4
Density (calculated)	1.495 Mg/m^3	1.627 Mg/m^3
Absorption coefficient	0.252 mm^{-1}	0.866 mm^{-1}
F(000)	664	1240
Crystal size	0.90 × 0.60 × 0.50 mm^3	0.40 × 0.30 × 0.20 mm^3
Theta range for data collection	2.873 to 28.572°.	2.832 to 28.544°.
Index ranges	–8<=h<=8,	–18<=h<=17,
		–19<=k<=19,

	–21<=k<=21, –19<=l<=19	–18<=l<=18
Reflections collected	17046	28699
Independent reflections	3561 [R(int) = 0.0366]	6021 [R(int) = 0.0331]
Completeness to theta = 25.242°	99.8 %	99.6 %
Absorption correction	Semi-empirical from equivalents	Semi-empirical from equivalents
Max. and min. transmission	0.884 and 0.805	0.846 and 0.723
Refinement method	Full-matrix least-squares on F^2	Full-matrix least-squares on F^2
Data/restraints/parameters	3561 / 0 / 199	6021 / 0 / 319
Goodness-of-fit on F2	0.908	1.007
Final R indices [I>2sigma(I)]	R1 = 0.0738, wR2 = 0.2210	R1 = 0.0334, wR2 = 0.0777
R indices (all data)	R1 = 0.0990, wR2 = 0.2577	R1 = 0.0441, wR2 = 0.0856
Extinction coefficient	n/a	n/a
Largest diff. peak and hole	1.367 and -0.699 e.$Å^{-3}$	0.742 and -0.581 e. $Å^{-3}$

Table S2 Selected bond lengths (Å) and angles (°)

	RuPNMT
Cl(1)–Ru(1)	2.4049(7)
N(4)–Ru(1)	2.116(2)
S(1)–Ru(1)	2.3263(7)
C(14)–Ru(1)	2.162(3)
C(15)–Ru(1)	2.248(3)
C(16)–Ru(1)	2.261(3)
C(17)–Ru(1)	2.189(3)
C(18)–Ru(1)	2.172(3)
C(19)–Ru(1)	2.217(3)
N(4)–N(5)	1.395(3)
N(3)–O(1)	1.196(4)
N(5)–C(9)–N(6)	117.4(3)
N(5)–C(9)–S(1)	124.8(2)
N(6)–C(9)–S(1)	117.8(2)
C(14)–Ru(1)–S(1)	122.66(8)
C(18)–Ru(1)–S(1)	87.12(8)
C(9)–S(1)–Ru(1)	98.27(9)
N(4)–Ru(1)–C(14)	93.55(10)
N(4)–Ru(1)–C(18)	147.09(10)
N(4)–Ru(1)–C(19)	111.30(9)
N(4)–Ru(1)–C(17)	168.98(10)

N(4)–Ru(1)–C(15)	103.55(10)
N(4)–Ru(1)–C(16)	131.76(10)
N(4)–Ru(1)–S(1)	80.87(6)
N(4)–Ru(1) –Cl(1)	86.70(6)
S(1)–Ru(1)–Cl(1)	87.15(3)

Table S3 CHNS analysis results

Compound	% C	% H	% N	% S
6NPT	48.47	4.37	17.34	9.96
6NMT	46.14	4.18	16.55	9.47
6NCT	51.45	5.20	15.95	9.17
6NMeT	42.58	3.56	19.84	11.38
RuPNPT	46.69	4.68	9.45	5.41
RuPNMT	45.45	4.51	9.18	5.26
RuPNCT	48.42	5.03	9.07	5.14
RuPNMeT	43.55	4.23	10.12	5.80
RuBNPT	42.60	3.54	10.47	5.96
RuBNMT	41.33	3.48	10.16	5.82
RuBNCT	44.74	4.13	9.91	5.67
RuBNMeT	38.79	3.03	11.29	6.44

References

1 J. R. Farrell, G. J. Kerins, K. L. Niederhoffer, L. A. Crandall and C. Ziegler, *Elsevier B.V.*, 2016, preprint, DOI: 10.1016/j.jorganchem.2016.03.030.

2 A. N. Usoltsev, T. S. Sukhikh, A. S. Novikov, V. R. Shayapov, D. P. Pishchur, I. V. Korolkov, I. F. Sakhapov, V. P. Fedin, M. N. Sokolov and S. A. Adonin, *Inorg Chem*, 2021, 60, 2797–2804.

3 B. Ivanova, *J Mol Struct*, DOI:10.1016/j.molstruc.2023.135746.

4 M. Asgari, H. R. Memarian, H. Sabzyan, H. A. Rudbari and O. Blacque, *J Mol Struct*, DOI:10.1016/j.molstruc.2025.141534.

5 A. Samdani and U. Vetrivel, *Comput Biol Chem*, 2018, 74, 39–48.

6 S. Chettri, P. Sasmal, T. Adon, B. Sajeev Kumar, B. P. Kumar and N. M. Raghavendra, *J Mol Graph Model*, DOI:10.1016/j.jmgm.2022.108340.

7 R. K. Chandrasekaran, S. Murugavel, M. Guin and T. Silambarasan, *J Mol Struct*, DOI:10.1016/j.molstruc.2022.132416.

8 M. Qamar, Shafiullah, Sultanat, H. Lal, A. Rizvi and M. Farhan, *Spectrochim Acta A Mol Biomol Spectrosc*, DOI:10.1016/j.saa.2024.124757.

9 L. Colina-Vegas, J. L. Dutra, W. Villarreal, J. H. João, M. R. Cominetti, F. Pavan, M. Navarro and A. A. Batista, *J Inorg Biochem*, 2016, 162, 135–145.

10 S. Gupta, A. Dev J R, C. Prakash Prasad, A. Kumar and S. Kumar Ghosh, *Bioorg Chem*, DOI:10.1016/j.bioorg.2024.107839.